



저작자표시 2.0 대한민국

이용자는 아래의 조건을 따르는 경우에 한하여 자유롭게

- 이 저작물을 복제, 배포, 전송, 전시, 공연 및 방송할 수 있습니다.
- 이차적 저작물을 작성할 수 있습니다.
- 이 저작물을 영리 목적으로 이용할 수 있습니다.

다음과 같은 조건을 따라야 합니다:



저작자표시. 귀하는 원저작자를 표시하여야 합니다.

- 귀하는, 이 저작물의 재이용이나 배포의 경우, 이 저작물에 적용된 이용허락조건을 명확하게 나타내어야 합니다.
- 저작권자로부터 별도의 허가를 받으면 이러한 조건들은 적용되지 않습니다.

저작권법에 따른 이용자의 권리는 위의 내용에 의하여 영향을 받지 않습니다.

이것은 [이용허락규약\(Legal Code\)](#)을 이해하기 쉽게 요약한 것입니다.

[Disclaimer](#) 

공학박사학위논문

**NO_x Scaling and Stability Characteristics of Turbulent
Non-premixed Jet Flames of H₂/CO Syngas**

**H₂/CO 합성가스 난류 비예혼합 제트화염의
NO_x 스케일링 및 화염안정성 특성**

2014년 2월

서울대학교 대학원
기계항공공학부
황정재

**NO_x Scaling and Stability Characteristics of Turbulent
Non-premixed Jet Flames of H₂/CO Syngas**

**H₂/CO 합성가스 난류 비예혼합 제트화염의
NO_x 스케일링 및 화염안정성 특성**

지도교수 윤 영 빈

이 논문을 공학박사학위 논문으로 제출함

2013년 11월

서울대학교 대학원
기계항공공학부
황정재

황정재의 공학박사학위 논문을 인준함

2013년 12월

위 원 장 _____

부위원장 _____

위 원 _____

위 원 _____

위 원 _____

ABSTRACT

NOx emission and stability characteristics of turbulent non-premixed jet flames of syngas hydrogen/carbon monoxide blends were investigated experimentally. The non-premixed jets in this study were formed by central fuel jet and surrounding coaxial air jet, the type widely used in practical combustors. Correlations among flame residence time, global strain rate of the jet and NOx emission were studied for single jet flames and stability limits and local flow characteristics were examined quantitatively for coaxial flames. For this studies, various measurement techniques, including NOx concentration measurement, OH* Chemiluminescence, particle image velocimetry and planar laser-induced fluorescence of OH, were used and measurements were focused on extreme near field of the flames.

The measured flame lengths of single jet flame of syngas increase with Re_f and the flame lengths also increase with the Froude number. Thus, it was confirmed that the jet flames investigated in this study are in the region of buoyancy-momentum transition. The NOx emission decreases with increase of Re_f since the decreasing effect on the flame residence time by the increased fuel jet velocity is more significant than the increasing effects by lengthened flame. As the CO content increases in syngas fuel, the NOx emission decreases since the flame length decreases due to higher stoichiometric mixture fraction. The modified NOx scaling, $EINOx/(L/U_f) \sim (U_f/d_f^*)^{-n}$, which adopted simplified residence time, L/U_f , satisfies $n = -1/2$, same as in hydrogen flames, for each fuel composition of syngas in buoyancy-momentum transition region. Further modified NOx scaling, $EINOx/f_{st}/(L/U_f) \sim (U_f/d_f^*)^{1/2}$, which considered NOx production per unit air consumption, finally collapsed all datasets of syngas into a single line.

The detachment stability characteristics of attached H₂ and syngas jet flames with coaxial air were investigated by observing flame behaviors with varying fuel jet and air jet velocities. The critical fuel jet velocity of the single jet flame of syngas decreases with increase of CO content in syngas fuel. Trends of stability limit have correspondence with the maximum burning velocity in high CO content region and with the stoichiometric mass ratio in high H₂ content region. Hydrogen jet flame show that the stability limits are

almost independent of the coaxial nozzle size in the fuel/air stream velocity domain while blowout of the lifted flames is related to the jet turbulent characteristics. Stability limit curve in fuel/air velocity domain shift upward with increase of rim thickness. Non-monotonic (ascending/descending: regime I/regime II) trends were observed for all syngas compositions in the fuel/coaxial air velocity domain. Local extinction on the rim was observed in regime I and local extinction at the starting point of shear layer near nozzle was observed by Chemiluminescence imaging. Stability limit in regime I could be scaled by fuel/air mass flux. For the syngas compositions, the stability curve extrema are found to be identical for identical nozzle lip thickness cases when the fuel nozzle velocity is normalized by the single jet critical velocity.

For understanding the detachment phenomenon in descending region (Regime II), strain rate and OH layer characteristics were studied experimentally with simultaneous PIV and OH PLIF measurements. The mean principal strain rate S_1 on OH layer decrease with the axial distance and the maximum values of them are located near the nozzle exit. In some cases, the maximum S_1 on OH layer near nozzle exit appears higher in the stable flames than in the flames near detachment. For various fuel jet Reynolds number, the flames near detachment condition have almost identical minimum mean OH layer thicknesses δ_{OH} near the nozzle exit. The S_1 on OH layer and the OH thickness δ_{OH} present inverse relationships, however, δ_{OH} is broadly scattered within a small S_1 range. The pdfs of δ_{OH} show that the distribution is skewed toward lower values within a higher S_1 range while broad distribution around higher values appears within a lower S_1 range. Moreover, the most probable value of δ_{OH} shifts toward lower value near the minimum mean δ_{OH} as the flame condition is varied from stable to near detachment.

Keywords: Non-premixed Flame, Diffusion Flame, Turbulent Flame, Jet Flame, NOx Scaling, NOx, EINOx, Flame Stability, Flame Length, Strain Rate, OH Layer, Scalar Dissipation, PIV, OH PLIF, IGCC, Syngas Combustion.

Student Number: 2009-30906

LIST

ABSTRACT	i
LIST	iii
LIST OF FIGURES.....	v
LIST OF TABLES	x
NOMENCLATURE.....	xi
CHAPTER 1	
INTRODUCTION	1
CHAPTER 2	
EXPERIMENT AND MEASUREMENT SYSTEMS.....	6
2.1 Combustor and Nozzles.....	6
2.2 Flame Imaging.....	9
2.2.1 Chemiluminescence Spectroscopy.....	9
2.2.2 Abel Transform	11
2.3 NO _x Measurement System	12
2.4 Simultaneous PIV and PLIF Diagnostics	14
2.4.1 OH PLIF Measurements	14
2.4.2 PIV Measurements.....	18
2.4.3 Simultaneous Measurement System	21
CHAPTER 3	
NO _x SCALING OF H ₂ /CO SYNGAS TURBULENT NON-PREMIXED JET FLAMES	23
3.1 Background and Objectives.....	23
3.2 Experimental Methods.....	26
3.3 Flame Length Characteristics	31

3.4 NO _x Emissions	38
3.5 EINO _x Scaling of Pure Hydrogen Flame	39
3.6 EINO _x Scaling of H ₂ /CO Syngas Flames.....	43
 CHAPTER 4	
STABILITY CHARACTERISTICS OF H ₂ /CO SYNGAS TURBULENT	
NON-PREMIXED JET FLAMES	
NON-PREMIXED JET FLAMES	48
4.1 Background and Objectives	48
4.2 Experimental Methods.....	52
4.3 Single Jet Flames of Syngas	56
4.4 Jet flames with Coaxial Air Jet	59
4.4.1 Hydrogen Flames	55
4.4.2 H ₂ /CO Syngas Flames.....	63
 CHAPTER 5	
NEAR FIELD STRAIN RATE AND OH LAYER CHARACTERISTICS OF	
H ₂ /CO SYNGAS TURBULENT NON-PREMIXED JET FLAMES	
H ₂ /CO SYNGAS TURBULENT NON-PREMIXED JET FLAMES	70
5.1 Background and Objectives	70
5.2 Experimental Methods.....	72
5.2.1 Experimental Apparatus and Conditions.....	72
5.2.2 Simultaneous PIV and OH PLIF Measurement	75
5.3 Stoichiometric velocity, U_s	75
5.4 Instantaneous Velocity and Strain Rate Fields with OH Layers	78
5.5 Mean Strain Rates on OH Layer.....	84
5.6 OH Layer Thickness	85
5.7 Relationship between Strain Rate and OH Layer Thickness	87
 CHAPTER 6	
CONCLUSION	91

REFERENCES.....	94
ABSTRACT IN KOREAN.....	102

LIST OF FIGURES

Fig. 1.1	Diagram of IGCC power plant processes (ref. [4]).	2
Fig. 1.2	Examples of (a) simple jet flame and (b) coaxial jet flame (ref. [23]).	3
Fig. 2.1	3-D view of the combustor (left) and sectional view of the nozzles (right).	6
Fig. 2.2	Igniter operating: heated wire (left) and working solenoid (right).	7
Fig. 2.3	Velocity distributions of coflowing air measured by hot-wire anemometry for each flow condition.	8
Fig. 2.4	Zirconia-ceramic sensor of non-sampling type NO _x analyzer.	13
Fig. 2.5	Operation principles of NO _x sensor.	13
Fig. 2.6	Schematic of energy transfer process. Relaxation processes emission of photons.	14
Fig. 2.7	OH excitation spectrum; In this study, Q ₁ (6) was used for OH PLIF.	16
Fig. 2.8	OH fluorescence spectrum for Q ₁ (6).	17
Fig. 2.9	Transmittance of UG11 (left) and WG305 (right).	17
Fig. 2.10	Principle of typical PIV system.	19
Fig. 2.11	Experimental setup for PIV and OH PLIF simultaneous measurements..	22
Fig. 3.1	Schematic of experimental apparatus and fuel nozzle (dotted circle) for turbulent non-premixed jet flames.	27
Fig. 3.2	(a) Comparisons of flame appearances through visible and OH* Chem. for 100/0, 75/25, and 50/50 H ₂ /CO%, and (b) flame length definition.	28
Fig. 3.3	Effects of the co-flow air on flame length for H ₂ /CO non-premixed turbulent jet flame.	30
Fig. 3.4	Comparisons of flame appearances from OH* chemiluminescence images according to Re_f (a, b, and c) and fuel composition (c, d, and e)	32

	for $d_f = 2.5$ mm.	
Fig. 3.5	Trends of flame length for pure hydrogen jet flame: (a) Normalized flame lengths according to Re_f , (b) Characteristic flame lengths according to characteristic Froude number.	33
Fig. 3.6	Trends of flame length for H ₂ /CO syngas jet flame: (a) Normalized flame lengths according to Re_f and theoretical values with $C = 19.3$, (b) Characteristic flame lengths according to characteristic Froude number.	36
Fig. 3.7	Similarity confirmation: the cubic of flame length L^3 according to the actual flame volume V for pure hydrogen flames.	38
Fig. 3.8	Trends of (a) NO _x and (b) EINO _x depending on Re_f , d_f , and fuel composition.	39
Fig. 3.9	EINO _x scaling for pure hydrogen jet flame based on Driscoll et al.'s [36] approach: EINO _x divided by flame residence time $L^3/(d_f^{*2}U_f)$ with global strain rate U_f/d_f^* .	40
Fig. 3.10	Comparison of previous flame residence time $L^3/(d_f^{*2}U_f)$ and simplified flame residence time L/U_f for the hydrogen flame data in Chen and Driscoll [29] and in the present study.	41
Fig. 3.11	Modified EINO _x scaling for pure hydrogen jet flame: EINO _x divided by simplified flame residence time L/U_f with global strain rate U_f/d_f^* .	42
Fig. 3.12	EINO _x scaling for H ₂ /CO syngas jet flame (a) Scaling based on Driscoll et al.'s [36] approach: EINO _x divided by flame residence time $L^3/(d_f^{*2}U_f)$ with global strain rate U_f/d_f^* (b) Modified scaling: EINO _x divided by simplified flame residence time L/U_f with global strain rate U_f/d_f^* .	45
Fig. 3.13	(a) Conceptual schematic of relationship between nitrogen consumption and NO _x production, (b) Constant C/f_{st} according to H ₂ fraction in syngas fuel.	46
Fig. 3.14	Modified EINO _x scaling for H ₂ /CO non-premixed turbulent jet flame:	47

$EINO_x/f_{st}$ divided by simplified flame residence time L/U_f with global strain rate U_f/d_f^* .

- Fig. 4.1 Schematics of the experimental apparatus and the nozzle geometry (dotted circle). 53
- Fig. 4.2 Syngas jet flame luminescence photographs: (a) pure H₂, (b) 75/25, and (c) 50/50 H₂/CO%. 55
- Fig. 4.3 Single jet flame stability of syngas fuels: (a) Critical fuel jet velocity versus hydrogen mole fraction in the fuel jet, (b) Maximum laminar flame speed ($S_{u,max}$) and air to fuel mass ratio at stoichiometric condition ($(m_a/m_f)_{st}$) versus hydrogen mole fraction in the fuel jet. 57
- Fig. 4.4 Conceptual schematic of the flame base location depending on the $(m_a/m_f)_{st}$ ratio. 58
- Fig. 4.5 Stability limits of pure hydrogen jet flames with coaxial air for various air shroud sizes ($d_a = 10.1, 12.4, \text{ and } 15.0 \text{ mm}$). 59
- Fig. 4.6 (a) Flame appearances including: 1/ attached single jet flame without coaxial air, 2/ attached flame with coaxial air, 3/ lifted flame, (b) Stability limits in terms of air/fuel Reynolds numbers (Legend: same as Fig. 4.5). 60
- Fig. 4.7 Detachment stability limits of hydrogen jet flames with coaxial air for various fuel nozzle rim thicknesses. 62
- Fig. 4.8 Detachment stability limits of syngas jet flames with coaxial air ($d_f = 3.0 \text{ mm}$, $l = 0.45 \text{ mm}$, and $d_a = 12.4 \text{ mm}$); crossed symbols are the stability limits for the single jet flame cases (see $U_a = 0 \text{ m/s}$). 63
- Fig. 4.9 Averaged OH* chemiluminescence images near the nozzle exit for the: (a) 100/0% H₂/CO, (b) 75/25% H₂/CO, and (c) 50/50% H₂/CO jet flames (Region of interest: $12.1 \times 12.1 \text{ mm}$, $d_f = 3.0 \text{ mm}$, $l = 0.45 \text{ mm}$, and $d_a = 12.4 \text{ mm}$). White arrows show the region of local extinction. 64
- Fig. 4.10 Inverse Abel transformed images of the averaged OH* chemiluminescence images in Fig 4.9: (a) 100/0% H₂/CO, (b) 75/25% 65

H₂/CO, and (c) 50/50% H₂/CO jet flames (Region of interest: 12.1 × 12.1 mm, $d_f = 3.0$ mm, $l = 0.45$ mm, and $d_a = 12.4$ mm). White arrows show the region of local extinction.

- Fig. 4.11 Detachment stability limits of syngas jet flames with coaxial air in terms of air/fuel mass fluxes: (a) datasets of Fig. 4.8, (b) complimentary datasets for additional burner geometries. 67
- Fig. 4.12 Detachment stability limits of syngas jet flames - coaxial air velocity U_a normalized by the maximum coaxial air velocity $U_{a,max}$ as a function of fuel jet velocity U_f normalized by the critical fuel velocity of the single jet case $U_{f,c}$: (a) Datasets of Fig. 4.8, (b) Additional cases for $d_f = 4.05$ mm (1/2 scaled for enhanced legibility) and $l = 0.9$ mm. 69
- Fig. 5.1 OH PLIF images of the flame near detachment condition in (a) regime I and (b) regime II. 71
- Fig. 5.2 Schematics of the experimental setup for simultaneous PIV and OH PLIF measurements. 73
- Fig. 5.3 Schematics of the nozzles: (a) the nozzle configurations and dimension, and (b) field of view for PIV and OH PLIF simultaneous measurement. 73
- Fig. 5.4 Conceptual schematic of the ideal mixing process in a uniform pressure condition. The mixture velocity is the stoichiometric axial velocity, $U_s = Z_s U_f + (1-Z_s) U_a$. (ref. [72]) 77
- Fig. 5.5 Instantaneous velocity fields and strain rate fields superimposed by the OH layer near detachment conditions for H₂/CO 100/0: (a) for Regime I and (b) for Regime II. The dashed line represents the stoichiometric velocity U_s . 79
- Fig. 5.6 Instantaneous velocity fields and strain rate fields superimposed by the OH layer near detachment conditions for H₂/CO 75/25: (a) for Regime I and (b) for Regime II. The dashed line represents the stoichiometric 80

- velocity U_s .
- Fig. 5.7 Instantaneous velocity fields and strain rate fields superimposed by the OH layer near detachment conditions for H₂/CO 50/50: (a) for Regime I and (b) for Regime II. The dashed line represents the stoichiometric velocity U_s . 81
- Fig. 5.8 Mean extensive principal strain rates, $\langle S_1 \rangle$, conditioned upon OH layer with x-axis: (a) H₂/CO 100/0, (b) 75/25/, and (c) 50/50. 83
- Fig. 5.9 Mean OH layer thickness ($\delta_{\langle OH \rangle}$) extracted from averaged OH PLIF images along axial direction: (a) H₂/CO: 100/0, (b) 75/25, and (c) 50/50. 120 instantaneous images were averaged for each case. Star indicates the minimum $\delta_{\langle OH \rangle}$ of each case. 86
- Fig. 5.10 Scatterplots of OH layer thickness (δ_{OH}) conditioned on extensive principal strain rate (S_1) for (a) 100/0, (b) 75/25 and (c) 50/50 H₂/CO flame. Black points are for near detachment condition ($U_a/U_{a,bo} \approx 0.95$) and gray points are for stable conditions ($U_a/U_{a,bo} \approx 0.6$). Solid line shows mean value, $\overline{\delta_{OH}}$. 89
- Fig. 5.11 Probability density function (pdf) of OH layer thickness (δ_{OH}) conditioned upon high S_1 and low S_1 at near detachment condition and stable condition. 90

LIST OF TABLES

Table 2.1	Formation and destruction of OH radical.	15
Table 3.1	Experimental conditions for turbulent non-premixed syngas jet flames.	30
Table 3.2	Properties of the H ₂ /CO mixtures (@ 300 K, 1 bar).	31
Table 4.1	Summary of milestone investigations related to jet flame stability characterization (*: shroud size not mentioned in the graphs, **: high temperature 300-1000 K, ***: 0.2 and 1.2 mm fuel nozzle → 2 deg. tapered on the outside).	49
Table 4.2	Experimental conditions for syngas jet flames with coaxial air ($d_f = 3.0$ mm and $d_a = 12.4$ mm).	54
Table 5.1	Experimental conditions (*ND: near detachment, ST: stable).	74

NOMENCLATURE

Alphabet

A_0	averaged flame area
A_T	wrinkled flame area
D	diffusivity
Da	Damkohler number
d_a	diameter of coaxial nozzle
d_f	diameter of fuel nozzle
d_f^*	effective diameter of jet, $m/(\pi\rho_a J/4)^{1/2}$
$EINO_x$	emission index of nitrogen oxides
Fr_f	characteristic fuel jet Froude number
f_{st}	stoichiometric air-fuel mass ratio, $(m_a/m_f)_{st}$
g	gravitational acceleration
J	jet momentum flux, $\Sigma\rho U^2$
L	flame length
l	rim thickness of fuel nozzle
m	jet mass flowrate, $\Sigma\rho U$
m_a	air mass flowrate
$m_{a,st}$	stoichiometric air mass flowrate corresponding to m_f
m_f	fuel mass flowrate
m_{N_2}	nitrogen mass flowrate
m_{NO_x}	mass production rate of NO _x
MW	molecular weight
r	radial distance
Re_a	coaxial air Reynolds number, $U_a\{d_a-(d_f+2l)\}/2\nu_a$
Re_f	fuel Reynolds number, $U_f d_f/\nu_f$
S_I	extensive principal strain rate
$S_{NO}(Z_b)$	maximum reaction rate
S_{rx}	shear strain rate, $1/2(\partial U_x/\partial x + \partial U_x/\partial r)$

$S_{u,max}$	maximum laminar flame speed
T_{st}	stoichiometric flame temperature
T_{∞}	ambient temperature
U_a	bulk exit velocity of coaxial nozzle
$U_{a,bo}$	detachment velocity of coaxial air
U_{co}	coflow air velocity
U_f	bulk exit velocity of fuel
$U_{f,c}$	critical fuel jet velocity
U_r	r -direction component of velocity
U_s	stoichiometric mixture axial velocity, $Z_s U_f + (1-Z_s) U_a$
U_x	x -direction component of velocity
V	flame volume
x	axial distance
Z	mixture fraction, $m_f/(m_a+m_f)$
Z_s	stoichiometric mixture fraction

Greek

α	thermal diffusivity
δ_{OH}	OH layer thickness
λ	wavelength
μ_a	viscosity of air
μ_f	viscosity of fuel
ν_a	kinematic viscosity of air
ν_f	kinematic viscosity of fuel
ρ_a	air density
ρ_f	fuel density
ρ_{∞}	ambient gas density
Φ_G	global equivalence ratio, $(m_a/m_f)_{st}/(m_a/m_f)$
χ	scalar dissipation rate

χ_{NO_x} NOx concentration

Subscript

a air

f fuel

st stoichiometric

∞ ambient

CHAPTER 1

INTRODUCTION

For the last 40 years, the world total fuel consumption, mainly relying on fossil fuel sources, has approximately doubled. However, the CO₂ emissions from fossil fuel started from the Industrial Revolution have been increased exponentially and do not seem to decrease in the past few decades. Recently, the Intergovernmental Panel on Climate Change (IPCC) reported that many natural systems are being affected by regional climate changes. This report was based on observations such as notable evolutions of the increase of the global average surface temperature, the increase of the global average sea level and the decrease of Northern Hemisphere snow cover [1]. One of world organization related on energy alerted that if no new plan is taken, the critical level of CO₂ emissions would be reached in 2030 with serious environmental and health problems. An alternative scenario has been considered for which the greenhouse gas concentration is stabilized at a 450 ppm CO₂-equivalent level in 2030 [2]. This scenario is called as 450 Scenario. This approach requires reduction of CO₂ emission through investments on energy efficiency at end-use level and power plants, and renewable energies, biofuels, nuclear power plants and carbon capture and storage (CCS) system in power plants.

For this challenging issue, both transport and power generation field, which take over 60% of CO₂ emission, will have to concentrate effort to achieve the scenario. Actually, the power generation field has been already engaged in the past 15 years, especially for the reduction of nitrogen oxide (NO_x) emissions in power plants [3]. The major advantage of gas turbines for power plant is high fuel flexibility. Integrated Gasification Combined Cycle (IGCC) power plant is one of alternative which can take advantages of fuel flexibility of gas turbines. This facility is an assembly of various technologies including gasification, carbon capture, synthesis gas (syngas) fuel combustion and so on to produce a clean and affordable energy (see Fig. 1.1). However, if the carbon-based feedstock adopts variety materials including coal, biomass, wastes etc.,

composition of the resulting syngas can be greatly varied. Thus, hardware such as combustor nozzle and chamber should be modified to ensure safe and efficient burning operations because syngas contains a large fraction of hydrogen which has high flame speed. For such a practical modification, fundamental studies on syngas combustion are needed.

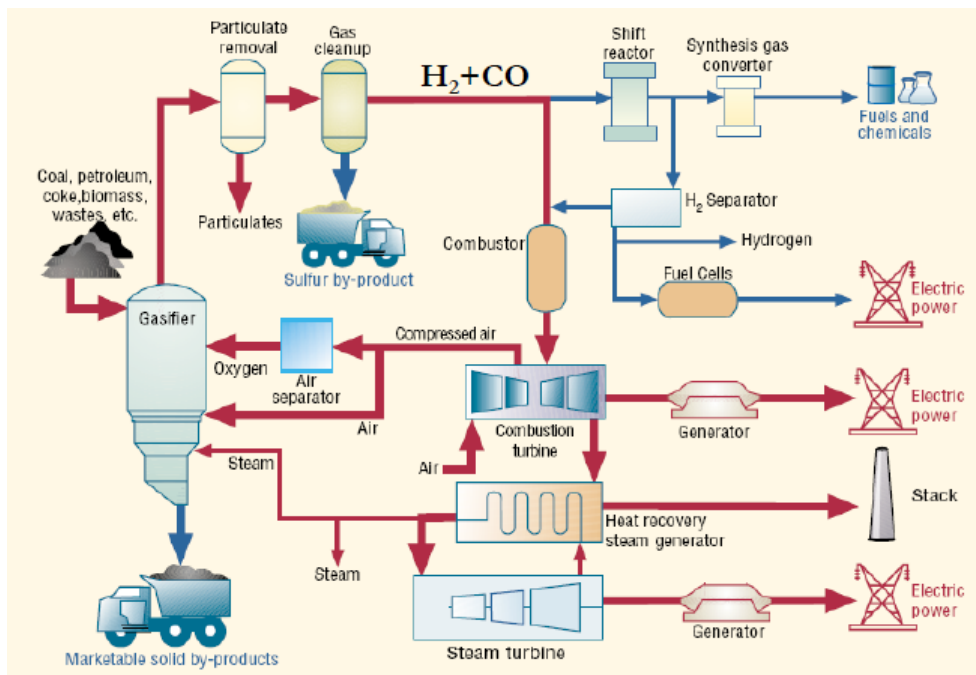


Fig. 1.1 Diagram of IGCC power plant processes (ref. [4]).

Syngas is a mixture of mainly hydrogen (H_2) and carbon monoxide (CO), which can be obtained from the coal gasification process prior to the combustor in a power plant. Recent research has investigated the characteristics of syngas combustion, focusing on its fundamental combustion properties, including, chemical kinetics [5-7], laminar [8-10] and turbulent [11,12] flame speeds, autoignition propensities [13-15], and turbulent jet characteristics [16,17]. Moreover, research on the characteristics of nitric oxides (NO_x) emissions of syngas flames have been investigated not only for fundamental flames

[16,18,19] but also for practical gas turbine combustors [20-22]. Non-premixed flames are usually applied in practical IGCC gas turbine combustors because syngas potentially causes flashback in premixed type combustors due to high burning velocities. Nevertheless, by contrast to large amount of other researches on syngas flames such as swirling premixed flame, counterflow diffusion flame, and so on, relatively little research on turbulent non-premixed jet flames of syngas has been conducted.

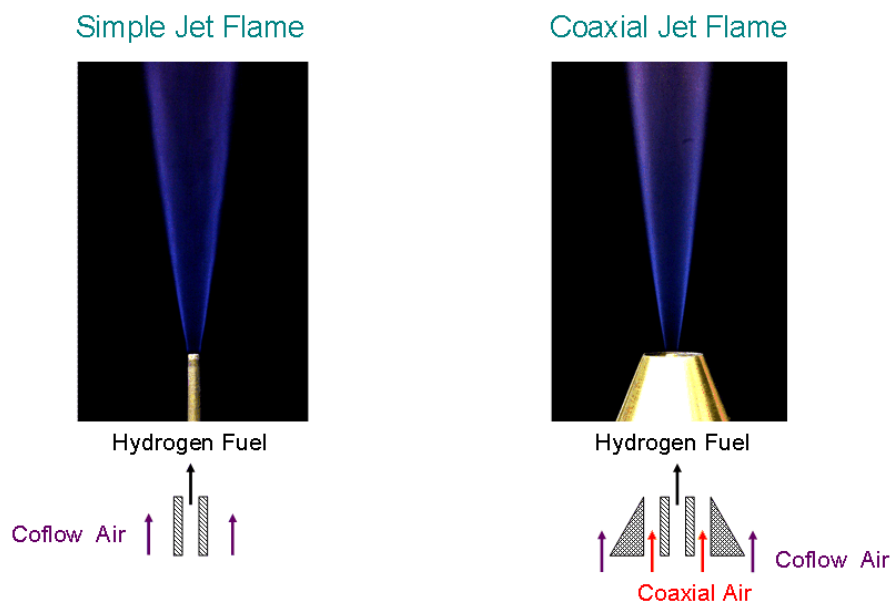


Fig. 1.2 Examples of (a) simple jet flame and (b) coaxial jet flame (ref. [23]).

The essential features of a turbulent jet issuing into a still ambient fluid, or a secondary stream, have been established, experimentally and numerically [24]. Although the general features on relatively simple jet flows are well known, little is known about the complicated flow field that arises from the interaction of two or more turbulent jets. In many practical combustion systems such as gas turbine combustors, furnaces, aircraft engines and rockets, coaxial jets are widely used because of their ability to provide high mixing performances in simple and safe configurations. Figure 1.2 shows the examples of

simple and coaxial jet flames. Simple jet flame has only a fuel jet, which is issued into a still or coflowing air. Coaxial jet flame, however, has a coaxial air jet as well as a central fuel jet, with surrounding coflow air or not. Such coaxial jet flame has some advantages in that coaxial air increases mixture homogeneity and shortens the characteristic flow time for nitrogen oxides (NO_x) formation, therefore, resulting in a lower NO_x emission index than that in simple jet flames without coaxial air. The emission of NO_x is known to be strongly related to flame temperature and the mixing level of cold fresh combustible mixture with hot gas product, especially for non-premixed jet flames in which the fluid mechanics may play an important role. Moreover, excess cold air entrained by the coaxial air may cool down the flame temperature [25].

Despite of advantages on low NO_x emissions of coaxial flames, the coaxial flames have disadvantages of stability characteristics arising from higher momentum of air flows. Higher momentum of coaxial air flows can cause higher strain or scalar dissipation on flame surfaces which can lead flame extinction.

Thus, the objective of this study is to investigate NO_x emission characteristics and stability characteristics of H₂/CO syngas turbulent non-premixed jet flames. For these purposes, the following studies were performed.

1. In Chapter 3, NO_x emission characteristics and emission index of NO_x (EINO_x) scaling of H₂ and H₂/CO syngas jet flames were investigated. We measured flame length and NO_x concentration simultaneously and assessed previous NO_x scaling. And new scaling parameter was suggested and assessed for hydrogen flames. Further, modified scaling of EINO_x was suggested and assessed for H₂/CO syngas jet flames.
2. In Chapter 4, stability characteristics of H₂/CO syngas simple and coaxial jet flames were investigated. Stability of single fuel jet flame with varying fuel composition was first studied. Effects of coaxial air nozzle diameter and fuel nozzle lip thickness were studied for hydrogen coaxial flames. Also, stability limits on fuel jet velocity and air jet velocity diagram was studied and near field

flame behavior near detachment condition was observed.

3. In Chapter 5, strain rates on flame surface and OH layer thickness which possibly govern local extinction were investigated using simultaneous PIV and OH PLIF measurements. Particularly, extreme near field region was observed where local extinctions due to high strains and high scalar dissipations lead the flame blowoff or liftoff. Relationship between strain rate on OH layer and OH layer thickness was examined and probability density function of OH layer was compared for the flames in stable and near detachment.

CHAPTER 2

EXPERIMENT AND MEASUREMENT SYSTEMS

2.1 Combustor and Nozzles

Experiments were performed in a rectangular-shaped combustor, shown in Fig. 2.1. The latter was equipped with four large quartz windows to provide convenient optical access to the flame. The axisymmetric fuel nozzle was located at the bottom center of the combustor and was surrounded by the coaxial air shroud (see Fig. 2.1). The fuel nozzles were made of stainless steel with various inner diameter d_f (3.0, 3.5 and 4.0 mm) and two different rim-thicknesses l , measuring respectively 0.45 and 0.9 mm. The coaxial air nozzles, made of brass, had inner diameters d_a respectively equal to 10.1, 12.4, and 15.0 mm. The fuel and coaxial air nozzle contractions were designed based on the Stokes-Beltrami streamline equations [26] to give uniform velocity profiles. A coflowing air stream was supplied from the bottom plane around the fuel and coaxial nozzles in order to maintain lean conditions in the combustor.

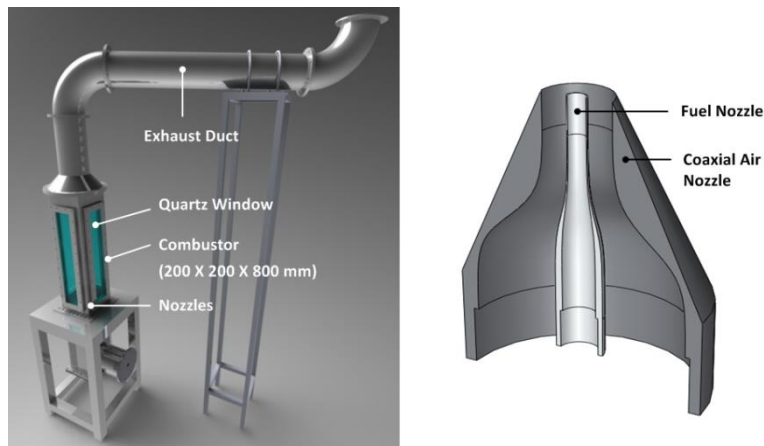


Fig. 2.1 3-D view of the combustor (left) and sectional view of the nozzles (right).

In order to ignite the flame, remote control of igniter was used to avoid direct exposure into the hazardous CO gas. Igniter was made by nichrome (Ni-Cr) wire which can be heated by high applied voltage (approximately 75V in this study). The igniter was installed on an arm which can be rotated by rotary solenoid. We applied voltages on the Ni-Cr wire and turn on the rotary solenoid when we ignite the flame and this is shown in Fig. 2.2.

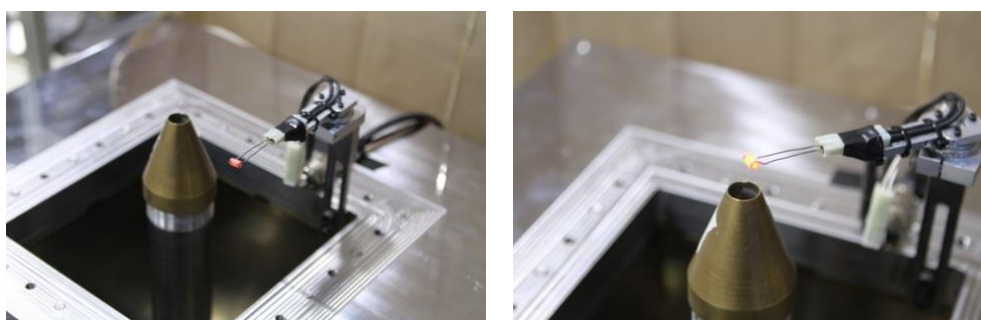


Fig. 2.2 Igniter operating: heated wire (left) and working solenoid (right).

The combustible gases (Air liquide, 99.95% purity) and in-house compressed air were individually metered using calibrated thermal mass flow controllers (Brooks 5851S/5853S). Hydrogen and carbon monoxide were supplied through a mixing chamber filled with 3 mm diameter glass beads for mixing enhancement. A coflowing air stream was controlled by a choked orifice (4 mm diameter, 45 degree-tapered) which was well calibrated by mass flow meter. The coflowing stream was passed through 20 mm diameter glass beads layer (400 mm height) and several layers of honeycombs (~ 3 mm hexagonal mesh, 200 mm height) and its output velocity was set to be lower than 0.2 m/s to avoid any perturbing effect in the combustion area of interest. We confirmed velocity distribution of the coflowing air. Velocities were measured by hot-wire at 48 points on exit plane for 110, 180, 245, and 313 standard liter per minute (SLPM), which are equivalent to calculated average velocity of 0.05, 0.082, 0.112, and 0.143 m/s respectively.

As shown in Fig. 2.3, measured velocities have well agreement with calculated values and great homogeneity even though central velocities are lower than averages due to wall effects by nozzle tube.

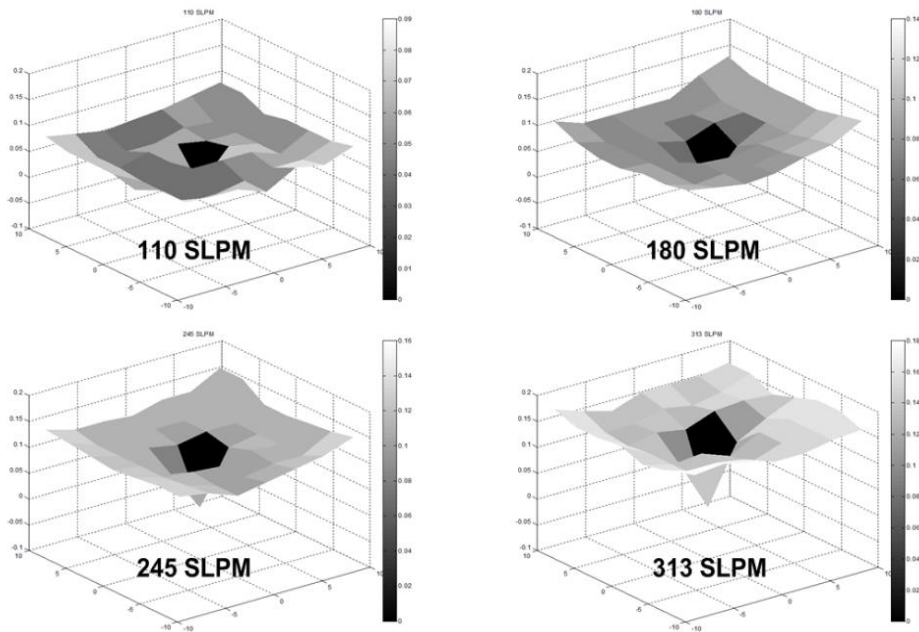


Fig. 2.3 Velocity distributions of coflowing air measured by hot-wire anemometry for each flow condition.

2.2 Flame Imaging

In this study, OH^* chemiluminescence images were recorded to measure flame length and flame structure. Many other studies used direct photography to identify flame length; however, images produced by this method are not good indicators of the reaction zone. We confirmed that the visible flame length of the pure hydrogen flame is longer than that of the OH^* based flame length. It has been generally known that the flame length measured by the flame temperature is 70% of visible flame length. The flame residence time in jet diffusion flame could be calculated from mean length and volume of flame, as defined in the literatures [27]. However, the OH^* chemiluminescence image should be used since OH radicals are good indicators of the reaction zone, which is a high temperature region where thermal NO_x can be produced. Thus, OH^* images were acquired using a ICCD camera (PI-MAX, Princeton Instruments, 512×512 pixel CCD) with a UV-Nikkor objective ($f = 105$ mm; $f/4.5$) and 307.1 ± 5 nm narrow bandpass filter. OH^* images were taken with 0.4 ms exposure time and 100 images were averaged for obtaining flame lengths and observing flame behaviors at near field region. The threshold value used to define the flame was 5% of the maximum intensity of the averaged image. The flame length was defined as the axial distance from the fuel nozzle exit to the tip of the flame.

2.2.1. Chemiluminescence Spectroscopy

Chemiluminescence, like atomic emission spectroscopy (AES), uses quantitative measurements of the optical emission from excited chemical species to determine analyte concentration; however, unlike AES, chemiluminescence is usually emission from energized molecules instead of simply excited atoms. The bands of light determined by this technique emanate from molecular emissions and are therefore broader and more complex than bands originating from atomic spectra. Furthermore, chemiluminescence can take place in either the solution or gas phase, whereas AES is almost strictly as gas

phase phenomenon. Like fluorescence spectroscopy, chemiluminescence's strength lies in the detection of electromagnetic radiation produced in a system with very low background. And on top of this, because the energy necessary to excite the analytes to higher electronic, vibrational, and rotational states (from which they can decay by emission) does not come from an external light source like a laser or lamp, the problem of excitation source scattering is completely avoided. The major limitation to the detection limits achievable by chemiluminescence involves the dark current of the photomultiplier (PMT) necessary to detect the analyte light emissions. If the excitation energy for analytes in chemiluminescence doesn't come from a source lamp or laser, where does it come from? The energy is produced by a chemical reaction of the analyte and a reagent. An example of a reaction of this sort is shown below:



In gas phase chemiluminescence, the light emission (represented as $h\nu$) is produced by the reaction of an analyte (dimethyl sulfide in the above example) and a strongly oxidizing reagent gas such as fluorine (in the example above) or ozone, for instance. The reaction occurs on a time scale such that the production of light is essentially instantaneous; therefore, most analytical systems simply mix analytes and the reagent in a small volume chamber directly in front of a PMT. If the analytes are eluting from a gas chromatographic column then the end of the column is often fed directly into the reaction chamber itself. Since as much of the energy released by the reaction should (in the analyst's eye) be used to excite as many of the analyte molecules as possible, loss of energy via gas phase collisions is undesirable, and therefore a final consideration is that the gas pressure in the reaction chamber be maintained at a low pressure (~ 1 torr) by a vacuum pump in order to minimize the effects of collisional deactivation. It must be stated that the ambiguous specification of "products" in the above reaction is often necessary because of the nature and complexity of the reaction. In some reactions, the chemiluminescent emitters are relatively well known. In the above reaction the major

emitter is electronically and vibrationally excited HF; however, in the same reaction, other emitters have been determined whose identities are not known and these also contribute to the total light detected by the PMT. To the analytical chemist the ambiguity about the actual products in the reaction is, in most case, not important. All the analyst cares about is the sensitivity of the instrument (read detection limits for target analytes), its selectivity-that is, response for an analyte as compared to an interfering compound, and the linear range of response. In chapter 3 and 4, OH* chemiluminescence measurements were conducted to obtain the reaction region. Finally, we could obtain the flame lengths based on the radical (OH radical in this study) by high UV quantum efficiency ICCD camera rather than the visible flame length based on the visible mixed emissions by normal SLR camera.

2.2.2. Abel Transform

Abel convolution is one of optical diffraction tomography and integral transform, such as onion pilling method and back-projection algorithm. It is useful to transfer a 3-dimensional line-of-sight image to a 2-dimensional profile. The light emission measurement of chemiluminescence cannot capture the fine flame structure, because the signal is integrated through the depth of the flame. Therefore, each image was processed with Abel convolution. With Abel inverted images, the time-averaged flame structure profile can be reconstructed, if the flame shape is axisymmetric.

In mathematics, the Abel transformation, named for Niels Henrik Abel, is an integral transform often used in the analysis of spherically symmetric or axially symmetric functions. The Abel transform of a function $f(r)$ is given by:

$$F(y) = 2 \int_y^{\infty} \frac{f(r) r dr}{\sqrt{r^2 - y^2}} \quad (2.2)$$

Assuming $f(r)$ drops to zero more quickly than $1/r$, the inverse Abel transform is given by:

$$f(r) = -\frac{1}{\pi} \int_r^{\infty} \frac{dF}{dy} \frac{dy}{\sqrt{y^2 - r^2}} \quad (2.3)$$

In Chapter 4, the OH^* chemiluminescence signal was processed through inverse Abel transform to transfer a 3D line-of-sight image into a 2D flame profile and the OH radical is treated as a marker of heat release in a reaction zone.

2.3 NOx Measurement System

A NOx analyzer (Horiba, Mexa-720NOx) with zirconia-ceramic sensor was used to measure the NOx concentration (see Fig. 2.4). From the operation principle of zirconia sensor (Fig. 2.5), NOx concentration was calculated from the current due to NO electrolysis. Similar study [28] has shown that the sensor should be located at least two flame lengths from the fuel nozzle exit where the NOx products were quenched. The products were found to be well mixed with the dilution air. It was also confirmed that NOx concentrations were constant downstream of the measuring points (i.e., 3, 4, and 5 combustor lengths from the nozzle). Thus, the NOx concentration was measured at point about three combustor lengths from the nozzle. NO sampled gas was required, thus reducing the response time up to 0.7 seconds. The measurement range was 0 to 3,000 ppm. The measured NOx concentration values, χ_{NOx} (in ppm) was converted into the emission index of NOx (EINOx), which is a conventional parameter defined by the total grams of NOx produced when 1kg of fuel is burned [29]. For a hydrogen and carbon monoxide syngas jet flame, EINOx is determined using:

$$EINOx = 0.001 \left(\frac{MW_{\text{NO}_2}}{MW_{\text{Fuel}}} \right) \chi_{\text{NOx}} \frac{1}{2} \left(1 + \frac{4.76}{\Phi_G} \right) \quad (2.4)$$



Fig. 2.4 Zirconia-ceramic sensor of non-sampling type NO_x analyzer.

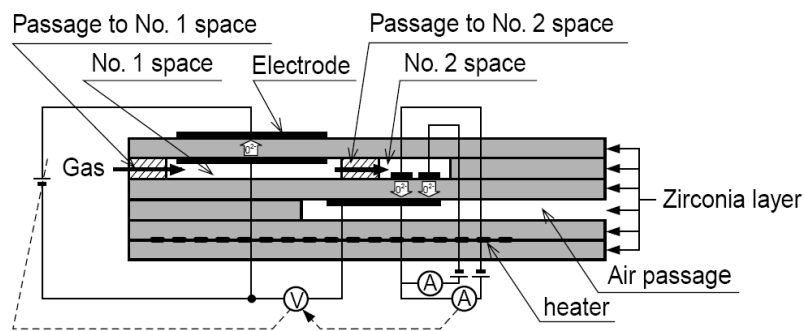


Fig. 2.5 Operation principles of NO_x sensor.

2.4 Simultaneous PIV and PLIF Diagnostics

2.4.1. OH PLIF Measurement

Laser induced fluorescence (LIF) is described as the absorption of a photon by a molecule of radical, followed by an emission of a photon as the molecules undergoes the transition from a higher level energy state to a lower one. Figure 2.6 shows the schematic of energy transfer process. Some of the molecules will relax to the initial state by emission of photon. Several relaxation processes are possible including (a) spontaneous emission, (b) stimulated emission by exterior stimulus, (c) quenching by collision of molecules, (d) redistribution of energy level, and (e) change of molecular component by chemical reaction. However, the rapid or spontaneous emissions of photons are termed as LIF. The frequency of LIF signal can have different value from that of inducing laser beam.

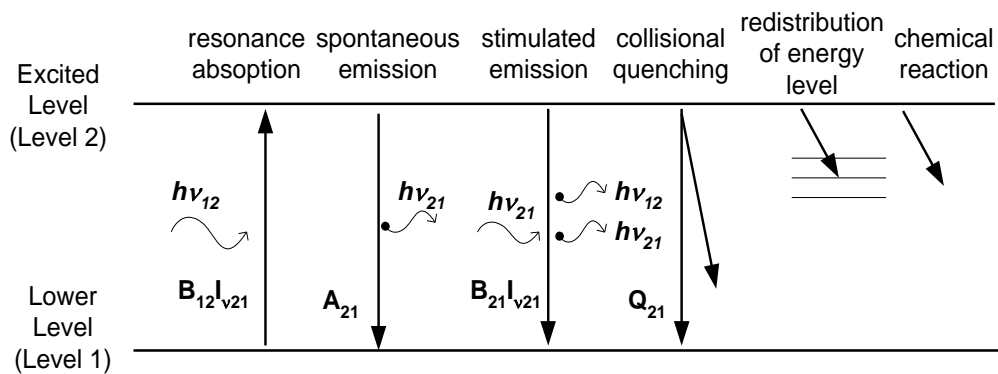


Fig. 2.6 Schematic of energy transfer process. Relaxation processes emission of photons.

Table 2.1 Formation and destruction of OH radical.

Fast OH formation by two-body reactions (1~5nsec)
$\text{H} + \text{O}_2 \leftrightarrow \text{OH} + \text{O}$ $\text{O} + \text{H}_2 \leftrightarrow \text{OH} + \text{H}$ $\text{H} + \text{HO}_2 \leftrightarrow \text{OH} + \text{OH}$
Slow destruction by three-body recombination reactions (~20μsec)
$\text{H} + \text{OH} + \text{M} \leftrightarrow \text{H}_2\text{O} + \text{M}$

OH PLIF was used to obtain spatially and temporally resolved images of the reaction zone in various combustors. As described in Table 2.1, the OH radical concentration increases rapidly around the flame in about 20 μsec and then decomposes slowly in 1 to 5 ms by a 3-body recombination reaction [30]. Thus, near the flame front exists super-equilibrium OH. The OH radical, which is intermediate product of chemical reaction, has a concentration of more ten times than that of O or H radicals [31]. Therefore, the OH radical is found to emit more intensive fluorescence signal than other species when absorbing laser light. Hence, the fluorescence signal of OH radical is widely used as an indicator of flame front in reacting flows.

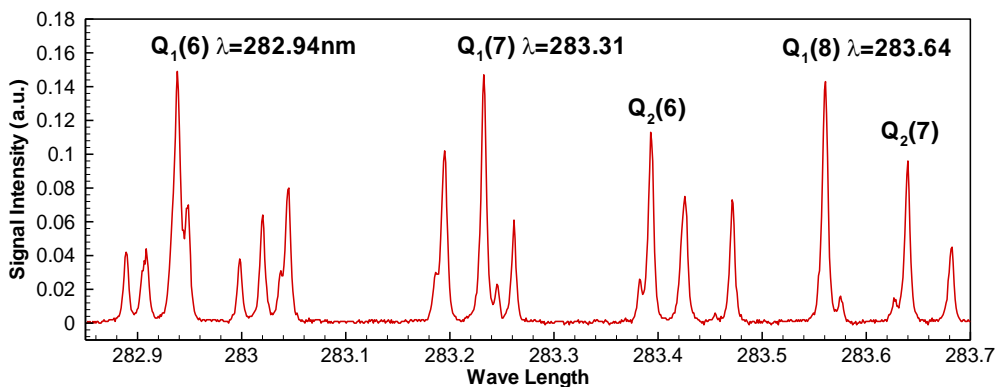


Fig. 2.7 OH excitation spectrum; In this study, $Q_1(6)$ was used for OH PLIF.

To observe the line positions for transition, we scanned the dye laser and recorded the signal at each step. We intended to use $Q_1(6)$ transition of the $A^2\Sigma^+ \leftarrow X^2\Pi$ ($v' = 1, v'' = 1$) band ($\lambda = 282.94$ nm) for the excitation wavelength and to collect the fluorescence signal from the $A-X$ (1, 0) and (0, 0) bands ($\lambda = 306 \sim 320$ nm). Using monochromator and PMT (photo-multiplier tube), in conjunction with a test flame in laminar premixed condition, a laser excitation scan was performed over the range of interest from $\lambda = 282.5$ nm to $\lambda = 283.5$ nm with 0.001 nm step. The monochromator was fixed at 315 nm to collect the fluorescence. The signal was multiplied by PMT and recorded through the boxcar averager. At every scanning step, 10 pulses of signal were recorded and averaged. After scanning the dye laser, the OH excitation spectrum can be obtained as shown in Fig 2.7. Among the peak values of excitation spectrum, we used $Q_1(6)$ as the excitation wavelength of OH radical.

When the location of $Q_1(6)$ line was detected, the fluorescence spectrum could be obtained by recording the LIF signal at each scanning step of the monochromator. Figure 2.8 is OH fluorescence spectrum graph for $Q_1(6)$. Peak value is found at 320nm.

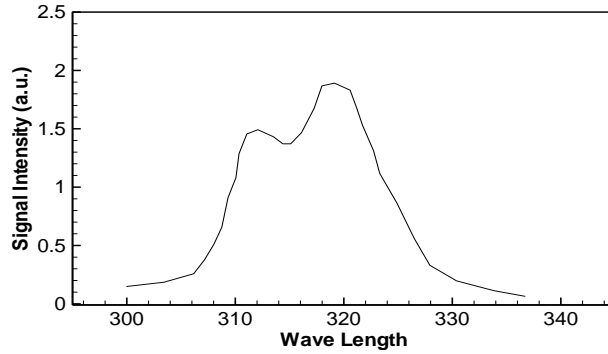


Fig. 2.8 OH fluorescence spectrum for $Q_1(6)$.

PLIF System

For OH PLIF, an Nd:YAG pumped dye laser was turned to $Q_1(6)$ transition of the $A^2\Sigma^+ \leftarrow X^2\Pi$ ($v' = 1, v'' = 1$) band ($\lambda = 282.94$ nm). $Q_1(6)$ transition line is generally used in the measurement of molecular concentration because it has large LIF signal and the dependency for temperature is low. Fluorescence from the $A-X$ (1, 0) and (0, 0) bands ($\lambda = 306 \sim 320$ nm) were collected with a UV-Nikkor 105 mm/f 4.5 objective. Because UV light cannot penetrate the common glass, all the lenses should be made with quartz. The region of interest was focused onto the ICCD camera of Princeton Instrument (PI-MAX 1K). Two filters (WG-305 and UG-11) were used to block scattered signal lights. Transmittance of each filter is shown in Fig. 2.9.

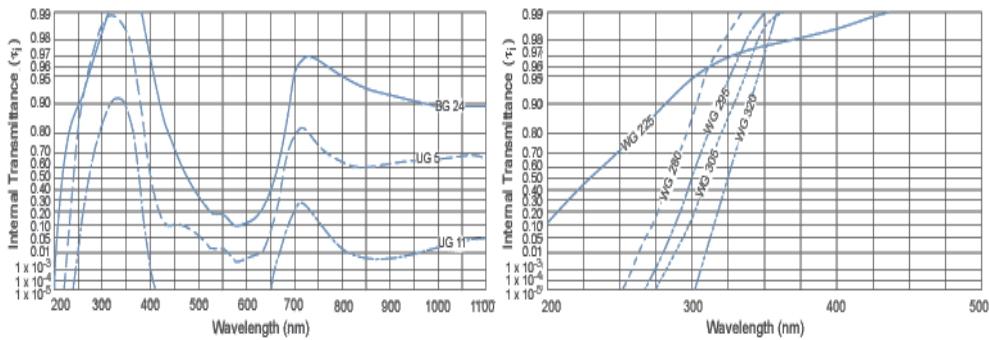


Fig. 2.9 Transmittance of UG11 (left) and WG305 (right).

2.4.2. PIV Measurement

A particle image velocimetry (PIV) is the measurement technique, which obtains the velocity vector fields of a flow by comparing consecutive two images. The experimental set-up of PIV system consists of several sub-systems: light source system, detecting system, and particle seeding system as shown in Fig. 2.10. Small particles have to be seeded into flow to perform PIV technique because PIV measures only the velocity of particles by comparing the displacement of the particle images illuminated by the sequential light pulses, not the flow itself.

Generally, a double pulsed Nd-YAG laser is used as a light source and a high speed CCD camera is employed to obtain instantaneous particle images at a measurement plane. There are no specific rules for particle seeding system; however, the size of particle should be determined by considering whether particles can follow the flow well or not [32]. In most cases, it is necessary to add tracer particles into the flow. These particles are illuminated at the measurement plane of the flow at least twice times within a short interval. The light scattered or fluoresced by particle is recorded either on a single frame or on sequential frames. The displacement of the particle images recorded by the light pulses is calculated through evaluation of the PIV.

To calculate the displacement of the particles grabbed by a CCD camera, it is necessary to divide the image into a grid. The grid is called as an interrogation spot. After setting the interrogation spot size, one interrogation spot of the first images is picked and compared with all the interrogation spot of the second images. The displacement between the interrogation spot of the first image and the interrogation spot of the second image represents one vector of flow field. By conducting this work in all the interrogation spots, whole vectors of flow-field are obtained. This process is called as a correlation.

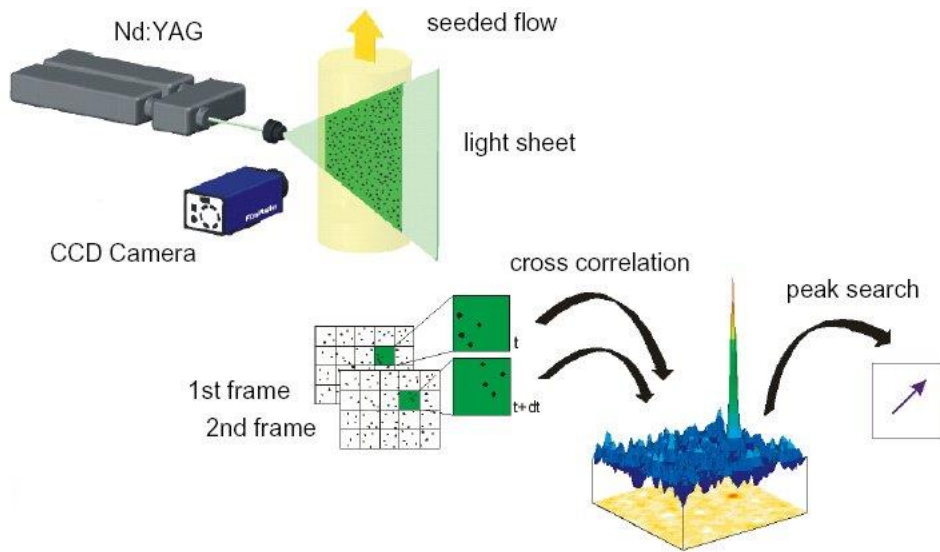


Fig. 2.10 Principle of typical PIV system.

The correlation function is expressed as follows:

$$h(s_x, s_y) = \int_0^{\infty} \int_0^{\infty} f(x, y)g(x + s_x, y + s_y)dx dy \quad (2.5)$$

The expression can become simple as conducting Fourier transformation for a convenience's sake in calculating. Here, F and G are Fourier transformed function of each f and g , and they mean Fourier transform operator.

$$F(h) = F^*(f) \times F(g) = F^* \times G \quad (2.6)$$

$$h = F^{-1}(F^* \times G) \quad (2.7)$$

Equation 2.5 is the same expression of spatial masking in an image processing technique. Thus, it means that a correlation is a kind of masking concepts. According to this concept, the correlation can be called as a process to figure out distribution of the similarity by signal distribution in an image plane. Equation 2.7 makes us use fast Fourier transform (FFT) algorithm which reduces the calculation time drastically. The interrogation spot size of $2n \times 2n$ should be chosen to use FFT algorithm because FFT algorithm is a method by dividing even and odd terms. However, the calculation time becomes short by $\log_2 N/N$ times comparing with direct Fourier transform (DFT) algorithm.

A correlation method is separated into auto-correlation and cross-correlation by the number of functions. Mathematically, auto-correlation is the case; $f(x; y) = g(x; y)$ in Eq. 2.5 and cross-correlation is the case; $f(x; y) \neq g(x; y)$. Experimentally, an auto-correlation is used for the case where the first image at $t = t_1$ and the second image at $t = t_2$ are recorded in one frame (called as a single frame/double exposure mode) and cross-correlation is used for the case where the first image at $t = t_1$ and the second image at $t = t_2$ are recorded in separated frames (called as a double frame/single exposure mode). Comparing with an auto-correlation method, a cross-correlation method has some merits as follows:

1. Directional ambiguity problem can be avoided easily.
2. The algorithm is simple because there is only one peak as a result of correlation.
3. Dynamic range is relatively large.

However, it was difficult to satisfy hardware requirements for cross-correlation. Specially, a time interval was a problem in most cases because the device, which satisfied both high resolution condition and short time interval (microsecond), was very expensive. Nowadays, it becomes relatively inexpensive and popular. Thus, most PIV systems use a cross-correlation method.

2.4.3. Simultaneous Measurement System

Figure 2.11 shows the experimental setup for PIV and OH PLIF measurements. The velocity field and the OH radical concentrations were measured simultaneously from the test section and the correlation between the flow property and chemical reaction was examined. As a laser system for the simultaneous measurements of the flow field, two Nd:YAG laser (Continuum Surelite II PIV and Continuum Surelite I) and a dye laser system (Continuum ND 6000) were used.

For PIV measurement, two second-harmonic beams ($\lambda = 532$ nm) were used. The two beams of the dual head Nd:YAG laser (Continuum Surelite II PIV) were provided at intervals depend on flow conditions. The other beam of the Nd:YAG laser (Continuum Surelite I) was supplied as pumping source of the dye laser (Continuum ND 6000). UV beam produced through the dye laser and frequency doubler was combined with the 532 nm beams from PIV laser at dichroic mirror which allow 532 nm beam to be transmitted and UV beam to be reflected. The combined beams were changed to sheet beams through the set of cylindrical lenses. A delay generator controlled the time separation among three laser beams, CCD camera, and ICCD camera. The pulse separation was confirmed using a photo-diode. Scattering signals from seeding particles were recorded on a high resolution (1600×1200) CCD camera (Viewworks, VH-2MC-M) equipped with f/2.8 AF Micro Nikkor 105 mm lens. Velocity vectors were calculated by means of FFT-based cross-correlation technique. The delay generator controlled the opening time of the camera shutter for the synchronization with the laser pulse.

For OH PLIF measurements, the 532 nm beam from the Nd:YAG laser (Continuum Surelite I) was changed to 567 nm with the dye laser and this 565.86 nm beam was changed to UV light (282.93 nm) after it passes the frequency doubler. The output beam was minutely tuned to $Q_1(6)$ transition of the $A^2\Sigma^+ \leftarrow X^2II$ ($v' = 1, v'' = 1$) band ($\lambda = 282.93$ nm) and fluorescence from the A-X(1, 0) and (0, 0) bands ($\lambda = 306 \sim 320$ nm) was collected with a UV-Nikkor 105 mm f/4.5 lens. The image was focused onto ICCD camera (Princeton Instrument, PI-MAX 1K, 1024×1024 pixels). This camera was fitted

with WG-305 and UG-11 color glass filters to block scattering signal and the incident light of flame.

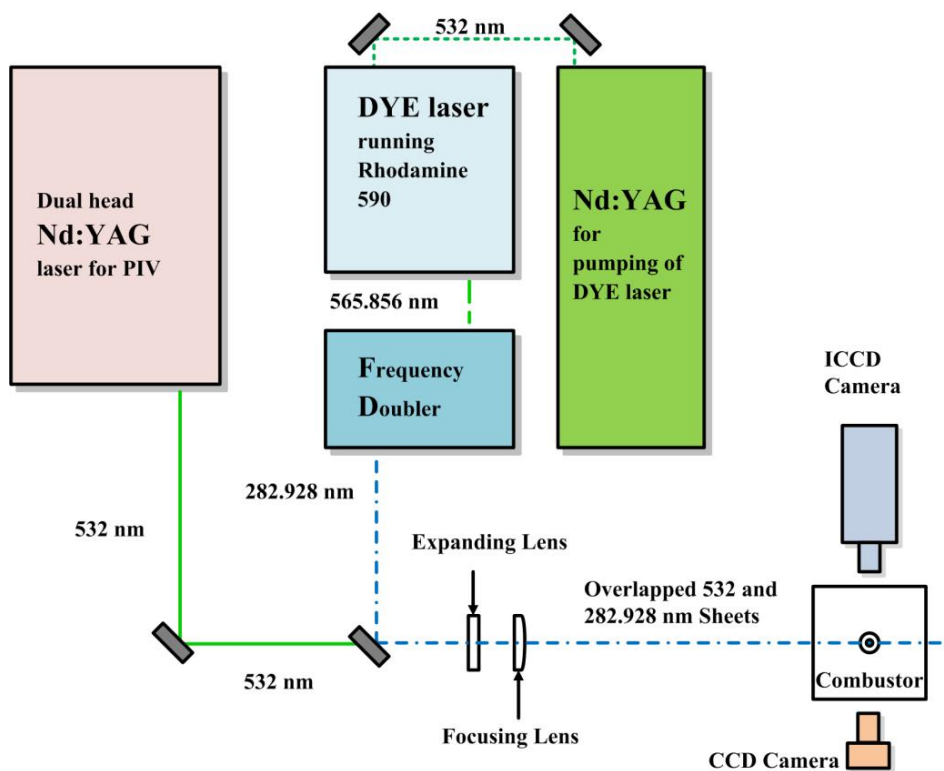


Fig. 2.11 Experimental setup for PIV and OH PLIF simultaneous measurements.

CHAPTER 3

NO_x SCALING OF H₂/CO SYNGAS TURBULENT NON-PREMIXED JET FLAMES

3.1 Background and Objectives

The recent development of Integrated Gasification Combined Cycle (IGCC) plants for power generation has demanded improved understandings of the combustion characteristics of synthesis gas (syngas). Syngas is a mixture of mainly hydrogen (H₂) and carbon monoxide (CO), which can be obtained from the coal gasification process prior to the combustor in a power plant. Recent research has investigated the characteristics of syngas combustion, focusing on its fundamental combustion properties, including, chemical kinetics [5-7], laminar [8-10] and turbulent [11,12] flame speeds, autoignition propensities [13-15], and turbulent jet characteristics [16,17]. Moreover, research on the characteristics of nitric oxides (NO_x) emissions of syngas flames have been investigated not only for fundamental flames [16,18,19] but also for practical gas turbine combustors [20-22]. Non-premixed flames are usually applied in practical IGCC gas turbine combustors because syngas potentially causes flashback in premixed type combustors due to high burning velocities. Nevertheless, by contrast to large amount of other researches on syngas flames such as swirling premixed flame, counterflow diffusion flame, and so on, relatively little research on turbulent non-premixed jet flames of syngas has been conducted.

Over the past several decades, advances have been made in understanding the kinetics of nitric oxide formation in non-premixed jet flames. There are several contributions: the thermal, prompt NO_x, and NNH, N₂O pathways. The thermal NO_x is formed through the extended Zeldovich mechanism; however, prompt NO_x is formed by oxidation of atomic nitrogen, cyanides, and amines produced by hydrocarbon fragments

attacking bimolecular nitrogen. Prompt NO_x is not very sensitive to temperature, and it contributes between 10 to 30 ppm in hydrocarbon flames, whereas thermal NO_x contributes up to several hundred ppm [33]. Hence, thermal NO_x may be the main contributor to NO_x production in practical systems with high temperature combustion. Rørtveit et al. [34] numerically simulated NO_x formation in diluted hydrogen counterflow flames. Their analysis showed that the thermal NO contributes over 90% of NO emission for high temperature hydrogen diffusion flames and NNH and N₂O mechanisms contribute less than 10%. Moreover, thermal NO_x is main contributor also in H₂/CO syngas non-premixed flames, since it produces high temperature and does not have hydrocarbon fragments. Giles et al. [18] numerically simulated NO_x emission of counterflow H₂/CO syngas diffusion flames and confirmed that most of NO_x emission is produced by a thermal route rather than an NNH or prompt route.

The global NO_x formation characteristics of non-premixed jet flames have been widely reported. In particular, many studies of hydrogen flames, which can neglect prompt NO_x, have been investigated [29,33,35-41]. Lavoie and Schlader [39] studied the nitric oxide levels of hydrogen-air turbulent diffusion flames. The nitric oxide levels were found to scale with the characteristic “jet time”. Peters and Donnerhack [33] investigated a theoretical formula for the NO emission index using probability density function and asymptotic analysis. They considered the simplest case and neglected the effects of strain, radiation super-equilibrium oxygen chemistry, and prompt NO. The study showed that the NO_x emission index (EINO_x) for a turbulent jet flame is predicted to be equal to

$$EINO_x \sim S_{NO}(Z_b) \epsilon [L^3 / (U_f d_f^2)] \quad (3.1)$$

where L is flame length, U_f is fuel jet velocity, and d_f is fuel nozzle diameter. EINO_x is defined as the total grams of NO_x produced when 1 kg of the fuel is burned [29,36]. $S_{NO}(Z_b)$ is the maximum reaction rate and ϵ represents the reaction zone thickness of NO production in the mixture fraction space. Both parameters are related to combustion chemistry and are highly dependent on the gas temperature. Discrepancies between the

experimental data and the theoretical formula were reported. They were attributed the lack of turbulence modeling. Chen and Driscoll [29] extended the theoretical EINOx scaling given by Peters and Donnerhack [33] by considering the turbulence effects. Flame sheet wrinkling caused by turbulence was considered by increasing the flame sheet area by a factor (A_T/A_0) , where A_T and A_0 are the wrinkled and averaged flame area, respectively. This factor can be scaled as Re^m . Broadening the flame thickness δ was also considered, which can be scaled as $(D/\sigma)^{1/2}Da^n$, where D is the gas mass diffusivity, σ is the strain rate, and Da is the Damkohler number. The latter is equal to $[(U_f/d_f)/(S_L^2/\alpha)]^{-1}$, where S_L is the maximum laminar burning velocity and α is the thermal diffusivity. The following scaling was obtained.

$$\frac{EINOx}{(L^3/U_f d_f^2)} \sim Re^{(m-\frac{1}{2})} Da^n \sim \left(\frac{U_f}{d_f}\right)^{1/2} \quad (3.2)$$

The H_2 flame data showed agreement with the above scaling for $m = 1/2$ and $n = -1/2$, which means that the EINOx normalized by flame residence time is proportional to the square root of the global strain rate shown in Eq. 3.2. Gabriel et al. [37] found that most inert-diluted hydrogen flames [35,38,41] investigated in experiments and modeling have verified the above scaling, which is also called 1/2-power scaling. Driscoll et al. [36] subsequently studied the effects of residence time and Damkohler number on the nitric oxide levels of turbulent jet diffusion flames. Helium-diluted hydrogen flame was studied to eliminate effects of radiative cooling, prompt NOx, and buoyancy. The effective jet diameter d_f^* introduced in the work of Thring and Newby [42] was addressed instead of d_f in the previous scaling in Eq. 3.2 in order to compare jet flames with different jet fluids. The scaling proposed by the authors is defined as follows:

$$\frac{EINOx}{(L^3/U_f d_f^{*2})} \sim \left(\frac{U_f}{d_f^*}\right)^{1/2} \quad (3.3)$$

where d_f^* is defined as $m/(\pi\rho_a J/4)^{1/2}$, with m is the jet mass flowrate and J is the jet momentum flux. The results for the helium-diluted hydrogen jet flames satisfy the 1/2-power scaling for each composition. However the datasets of all fuel compositions were not found to collapse into a single line.

To extend the findings of previous works, the present study investigated NOx emission characteristics and EINOx scaling of non-premixed turbulent jet flames for H₂/CO syngas. The objectives of this study were (a) assessment of the previous NOx scaling and proposition of the modified scaling for hydrogen flames in momentum-buoyancy transition region and (b) proposition of the modified scaling for syngas H₂/CO flames. Flame length, one of the main parameters of NOx formation, was first investigated. Assessments of the well-known 1/2-power scaling for pure hydrogen flame were performed on the hydrogen and syngas flames. The proper parameters of flame residence time were considered, and a modified scaling of syngas jet flame was proposed.

3.2 Experimental Methods

All experiments were performed in a confined, atmospheric pressure, non-premixed jet combustor facility (see Fig. 3.1). The facility consists of a combustion chamber, dedicated flow control, visualization, and a NOx measurement unit. The combustor is rectangular in shape and surrounded by four quartz plates, which provides convenient optical access. The fuel nozzle, made of SS, was located at the bottom center of the combustor. A co-flowing stream of air was supplied from the bottom plane around the fuel nozzle in order to control the global equivalence ratio (Φ_G). The latter is defined as an equivalence ratio based on fuel flow rate and co-flow air flow rate. It can be expressed as follows:

$$\Phi_G = \frac{(m_a/m_f)_{st}}{(m_a/m_f)} \quad (3.4)$$

where m_a is co-flow air flow rate and m_f is fuel flow rate.

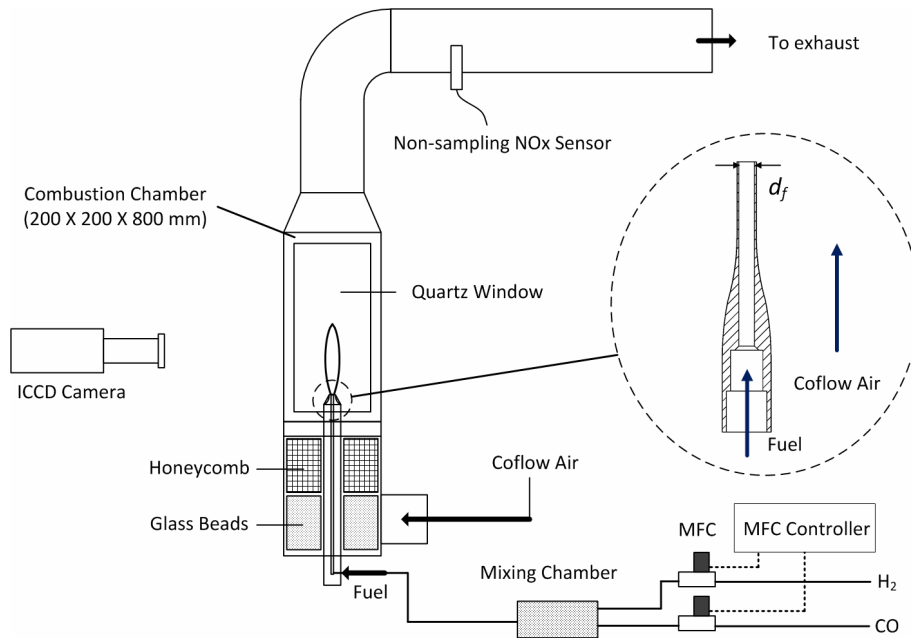


Fig. 3.1 Schematic of experimental apparatus and fuel nozzle (dotted circle) for turbulent non-premixed jet flames.

Gaseous H_2 and CO (Air Liquid, 99.95% purity) flow rates were individually metered with the calibrated thermal massflow controllers (Brooks 5851S/5853S). The fuel gases were supplied through a mixing chamber filled with 3 mm diameter glass beads to enhance the mixing process. The co-flow air was supplied by an in-house compressor and controlled by a well-calibrated choked orifice (4 mm diameter, 45° tapered). The air flow was passed through several layers of honeycombs. The velocity of the stream was set at lower than 0.2 m/s to avoid disturbing effect in the combustion area.

In this study, OH^* chemiluminescence images were recorded to measure flame length. Many other studies used direct photography to identify flame length; however, images produced by this method are not good indicators of the reaction zone. Figure 3.2(a)

shows comparisons of the visible and OH* chemiluminescence appearances of the flames. The 100% H₂ flame shown in the visible image is slightly longer than that of the OH* image. However, the OH* images of other flames are longer than the visible images of other flames. Near infra-red emission due to vibrationally excited water molecules [43,44] are dominant in downstream of the hydrogen jet flame. Consequently, the visible flame length of the pure hydrogen flame is longer than that of the OH* based flame length. Thus, the OH* chemiluminescence image should be used since OH radicals are good indicators of the reaction zone, which is a high temperature region where thermal NO_x can be produced. The OH* images were acquired using a ICCD camera (PI-MAX, Princeton Instruments, 512 × 512 pixel CCD) with a UV-Nikkor objective (f = 105 mm; f/4.5) and 307.1 ± 5 nm narrow bandpass filter. The exposure time was 0.4 ms, and 100 images were accumulated. Figure 3.2(b) shows the definition of the flame length. The threshold value used to define the flame was 5% of the maximum intensity of the accumulated image. The flame length was defined as the axial distance from the fuel nozzle exit to the tip of the flame.

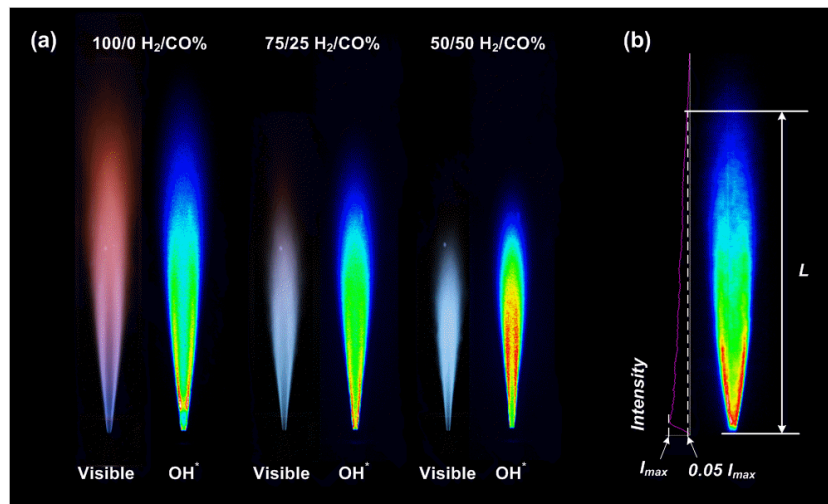


Fig. 3.2 (a) Comparisons of flame appearances through visible and OH* Chem. for 100/0, 75/25, and 50/50 H₂/CO%, and (b) flame length definition.

A NOx analyzer (Horiba, Mexa-720NOx) with zirconia-ceramic sensor was used to measure the NOx concentration. Similar study [28] has shown that the sensor should be located at least two flame lengths from the fuel nozzle exit where the NOx products were quenched. The products were found to be well mixed with the dilution air. It was also confirmed that NOx concentrations were constant downstream of the measuring points (i.e., 3, 4, and 5 combustor lengths from the nozzle). Thus, the NOx concentration was measured at point about three combustor lengths from the nozzle. The measured NOx concentration was converted into the EINOx.

The co-flowing air stream was used to supply a sufficient amount of air to the combustor. Since the combustor is confined and the combustion is non-premixed type, enough co-flowing air should be provided in order to simulate free ambient air to ensure complete combustion of the reactant. The effect of the global equivalence ratio (Φ_G) on the flame length was checked, as shown in Fig. 3.3. With the increased co-flow air flowrate (i.e., decrease of Φ_G), the flame length increased down to $\Phi_G = 0.5$. In the region of $0.5 < \Phi_G < 1.0$, it is here thought that the increase in air flow induced complete combustion of the reactant downstream of the flame. Consequently the flame length was increased. However, in the range of $\Phi_G \leq 0.5$, the flame length was constant. When the amount of co-flow air is sufficient to induce complete combustion, the flame length is no longer affected by the air flowrate. The results of the co-flow air effect test confirmed that flame length is not affected by Φ_G in the range of $\Phi_G \leq 0.5$. Therefore, in this study, the Φ_G was fixed at 0.5 in all experimental conditions.

Experiments were conducted for four fuel compositions (100/0, 75/25, 50/50, and 25/75 H₂/CO% Vol.) and three fuel nozzle diameters ($d_f = 2.5, 3.0, \text{ and } 3.5 \text{ mm}$). In each case, the fuel jet was turbulent, and the flame was attached to the nozzle rim. The Reynolds number (Re_f) is varied from 4000 to the upper limits mentioned in Table 3.1 corresponding to the flame detachment. The fuel jet Reynolds number was defined as $Re_f = (\rho_f U_f d_f) / \mu_f$, where μ_f is dynamic viscosity of the fuel. These experimental conditions are shown in Table 3.1. The properties of each fuel composition used to calculate the jet Reynolds number and other parameters are shown in Table 3.2.

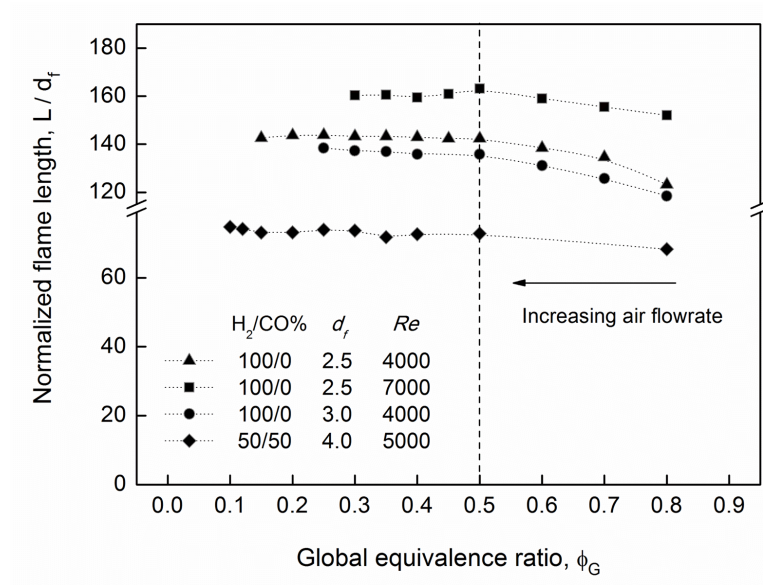


Fig. 3.3 Effects of the co-flow air on flame length for H_2/CO non-premixed turbulent jet flame.

Table. 3.1 Experimental conditions for turbulent non-premixed syngas jet flames.

H_2/CO [% Vol.]	Re_f	d_f [mm]	Φ_G
100 / 0	4000 – 13000		
75 / 25	5000 – 20000		
50 / 50	5000 – 21000	2.5 / 3.0 / 3.5	0.5
25 / 75	5000 – 14000		

Table. 3.2 Properties of the H₂/CO mixtures (@ 300 K, 1 bar).

H ₂ /CO [% Vol.]	100 / 0	75 / 25	50 / 50	25 / 75
ρ_f [kg/m ³]	0.082	0.346	0.610	0.874
μ_f [μPa·s]	9.17	15.3	17.0	17.6
MW [g/mol]	2.016	8.515	15.013	21.512
f_{st}	34.061	8.064	4.574	3.192
T_{st} [K]	2385	2377	2376	2379

3.3 Flame Length Characteristics

Because the flame length governs the flame residence time, it can be the main parameter affecting thermal NO_x production. The flame appearances are shown in Fig. 3.4. The images were obtained using OH* chemiluminescence and taken at $d_f = 2.5$ mm. Generally, in turbulent momentum jet flames, the flame length is almost constant with Re [45]. Generally, the flame length is almost constant with Re in turbulent momentum jet flames [45]. However, the comparison of the first group (cases a, b, and c) shows that the flame length for pure H₂ increases as Re_f increases. It is believed that the pure H₂ flames investigated in this study are not in the momentum-dominated region, which is discussed below. The comparison of another group (c, d, and e) with fixed Re_f showed that in the syngas fuel, the flame length decreases as the CO content increases, which is presumably caused by the decreasing stoichiometric air-fuel mass ratio (f_{st}) as the CO content increases. Further details of this effect are provided below.

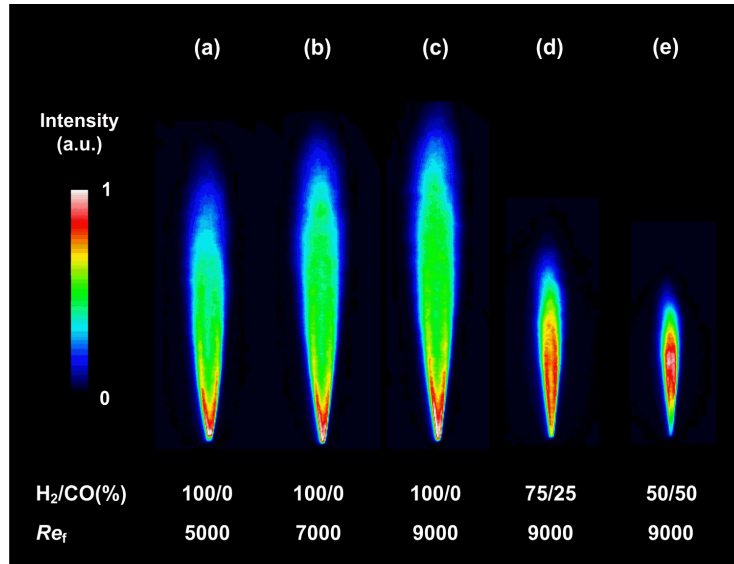


Fig. 3.4 Comparisons of flame appearances from OH* chemiluminescence images according to Re_f (a, b, and c) and fuel composition (c, d, and e) for $d_f = 2.5$ mm.

The normalized flame lengths with various fuel nozzle diameters of the present study's and Chen and Driscoll's [29] hydrogen jet flame are shown in Fig. 3.5(a). The present study shows that flame lengths are slightly increased with increasing Re_f up to $Re_f \approx 10000$, whereas in the $Re_f > 10000$ region, flame lengths are almost constant with Re . However, in Chen and Driscoll's results, normalized flame lengths are almost constant in all turbulent regions ($Re_f > 4000$).

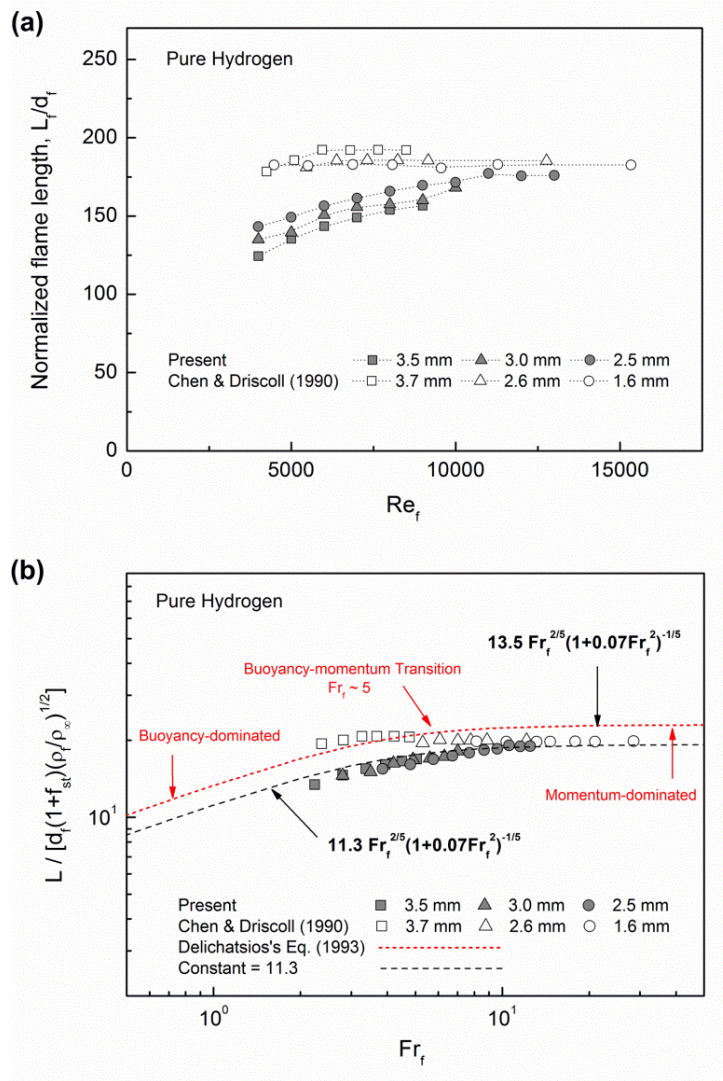


Fig. 3.5 Trends of flame length for pure hydrogen jet flame: (a) Normalized flame lengths according to Re_f , (b) Characteristic flame lengths according to characteristic Froude number.

We introduced the previous report of Delichatsios [46] to confirm the region of the jet flames. According to Delichatsios [46], turbulent jet flames can be classified into three regions: buoyancy-dominated, momentum-dominated, and buoyancy-momentum transition. With respect to the flame length, the length of the jet flame increases according to the Froude number in buoyancy-dominated region, whereas the length is constant with the Froude number in momentum-dominated region. Between the latter two regions is the buoyancy-momentum transition region where the length slightly increases according to the Froude number. Delichatsios [46] reported a semi-empirical correlation for the flame height of turbulent jet flames, which can be expressed as follows:

$$\frac{L}{d_f} = \frac{13.5 Fr_f^{2/5}}{(1 + 0.07 Fr_f^2)^{1/5}} (f_{st} + 1) (\rho_f / \rho_\infty)^{1/2} \quad (3.5)$$

where Fr_f is the characteristic Froude number, defined as

$$Fr_f = \frac{U_f}{\left(\frac{\overline{\Delta T_{fa}}}{T_\infty} g d_f \right)^{1/2} (f_{st} + 1)^{3/2} \left(\frac{\rho_f}{\rho_\infty} \right)^{1/4}} \quad (3.6)$$

where ρ_∞ is the density of the ambient air, T_∞ is the ambient temperature of the surrounding air, $\overline{\Delta T_{fa}}$ is the modified mean flame temperature rise inside the turbulent flame, and g is the gravitational constant. Figure 3.5(b) shows the results in Chen and Driscoll [29] and the present study. The characteristic flame length is plotted with the characteristic Froude number. The results of the present study are in good agreement with Delichatsios's correlation (shown as the red dotted line in Fig. 3.5(b)) in terms of tendency, whereas the scale is smaller than the correlation. This discrepancy in the scale was presumably caused by the measuring method. Delichatsios [46] used datasets in previous work by Kalghatgi [47], who measured the flame length with still photographs. In general, the visible flame length is known to be larger than that based on temperature

or concentration [48]. The OH^* chemiluminescence measurement used here is much closer to the latter method than visible photographs are. Thus, the flame length datasets in this work are smaller than the empirical correlation. If the constant of Eq. (3.5) is altered from 13.5 to 11.3, the datasets in the present study are in good agreement with the correlation (see the black dotted line in Fig. 3.5(b)). As shown in Fig. 3.5(b), both studies were conducted in buoyancy-momentum transition region, not in momentum-dominated region where the Froude number is around 5. Therefore, it is general that the flame length is slightly increased with increasing Fr_f in this region. The results of the present study show that the characteristic flame length increases with Fr_f , whereas Chen and Driscoll's [29] results are constant. It is thought that these discrepancies are caused by the higher co-flow air velocity in Chen and Driscoll [29]. Because of the differences in co-flow air condition, Chen's results [29] are in momentum-dominated region even though the fuel jet condition (i.e., Fr_f) is in transition region. In summary, the present work was conducted in buoyancy-momentum transition region, whereas Chen and Driscoll's [29] study was conducted in momentum-dominated region.

Figure 3.6(a) shows the normalized flame length of the syngas jet according to various nozzle diameters and fuel compositions. The flame length scale decreases as the CO content in the syngas fuel increases. However, the rate of decrease in the length scale is reduced with increased CO content. As explained above, the flame length of the turbulent jet flame depends on the stoichiometric air-fuel mass ratio. According to the flame length scaling [36], normalized flame length is proportional to f_{st} and $\rho_f^{1/2}$, which is expressed as follows:

$$L/d_f = C \cdot (1 + f_{st}) \cdot (\rho_f/\rho_a)^{1/2} \quad (3.7)$$

where C is a constant. The flame length decreases as the CO content in the syngas fuel increases because the decreasing rate of f_{st} has greater significance than the increasing rate of $\rho_f^{1/2}$, as shown in Table 3.2. The theoretical values of normalized flame length based on Eq. (3.7) with a constant of 19.3 for all fuel compositions are shown as straight

lines in Fig. 3.6(a).

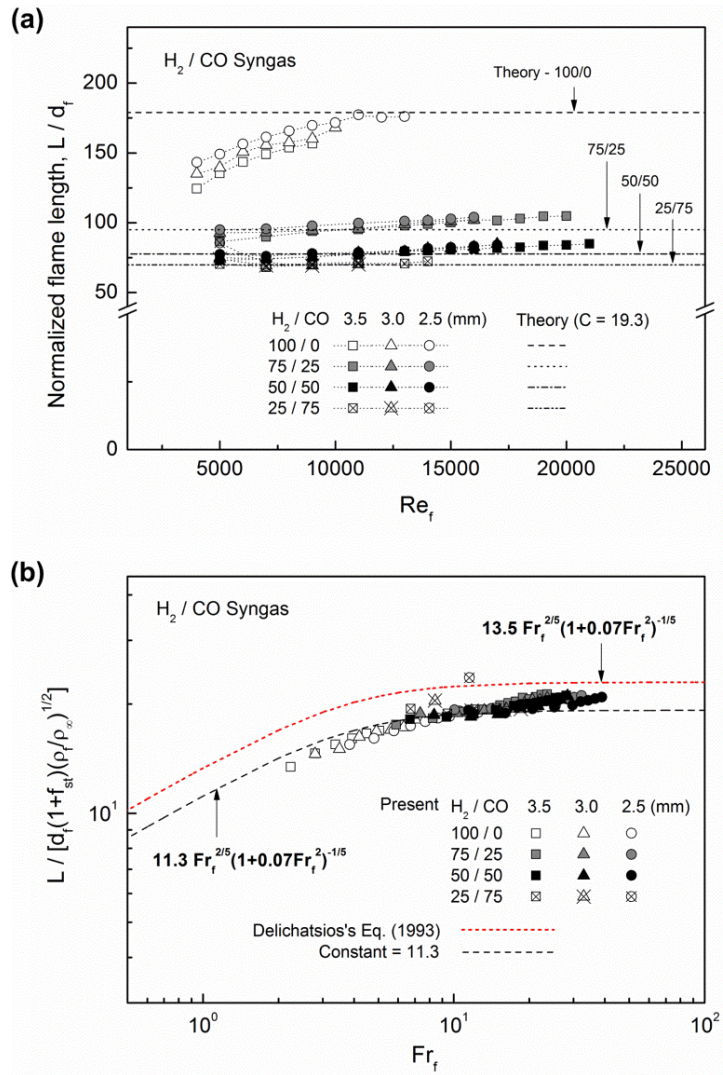


Fig. 3.6 Trends of flame length for H_2/CO syngas jet flame: (a) Normalized flame lengths according to Re_f and theoretical values with $C = 19.3$, (b) Characteristic flame lengths according to characteristic Froude number.

The theoretical lengths are well matched with the experimental datasets. In particular, since the theoretical correlation is based on the similarity of the momentum driven jets, pure H₂ flames are matched at higher Re_f when the jet flames are close to the momentum-dominated region. Equation (3.5) shows the same result for the momentum-driven jet. If the Froude number goes to infinity the normalized flame length yields exactly the same formula as Eq. (3.7). In a syngas jet flame with higher CO content, the flame length is less dependent on Re_f . This trend is presumably due to the shortened length scale with increased CO content, which causes the jet flame to be close to the momentum-dominated region instead of transition region. Figure 3.6(b) shows the characteristic flame length according to the characteristic Froude number for syngas jet flames. As CO content increases in syngas, the Froude number is in higher region and characteristics flame lengths slightly increase, but not too significantly. All cases of fuel composition are in good agreement trend with Delichatsios's [46] empirical correlation, which is shown as red dotted line (Fig. 3.6(b)), but not in terms of scale. As previously discussed, discrepancy of scale is attributed by measuring method. If the constant is changed from 13.5 to 11.3 in Eq. (3.5), the datasets are in good agreement with the correlation that is shown as the black dotted line (Fig. 3.6(b)). Thus, the results of the present study showed that the syngas jet flames are in the buoyancy-momentum transition region even though some conditions are close to the momentum-dominated region.

In order to make sure of non-similarity of the flames in this study, a comparison between the actual flame volume, V , and the L^3 was conducted. If the similarity of the mixture fraction field is satisfied for the flames, the L^3 will be proportional to the V . In Fig. 3.7, the L^3 is plotted according to the V for pure hydrogen flames. As shown in this figure, the L^3 is not proportional to the V but increasing with the slope larger than unity. It can be interpreted that the L^3 over scales the flame volume because only the flame length L is increased by buoyancy effects while the flame width is rarely affected by buoyancy.

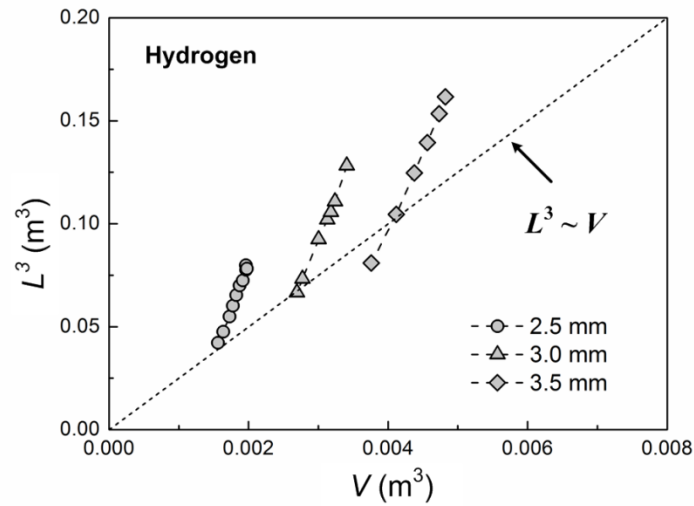


Fig. 3.7 Similarity confirmation: the cubic of flame length L^3 according to the actual flame volume V for pure hydrogen flames.

3.4 NOx Emission

Figure 3.8 shows NOx emission and EINOx characteristics according to Re_f for various nozzle diameters and syngas fuel compositions. As shown in Fig. 3.8(a), NOx emission decreases with increasing Re_f . For a given nozzle diameter and fuel composition, the residence time, which is a main parameter affecting thermal NOx formations, decreases with Re_f because of the higher exit velocity. Even though the flame length increases with Re_f (see Fig. 3.6(a)), the corresponding increase of residence time is insignificant compared to the effects on shortening the residence time by increased exit velocity. As the CO content increases in the syngas fuel, NOx emissions decrease because of the decreased flame length. The shortened flame decreases the flame residence time, which causes decreasing NOx emissions. When Re_f and fuel composition are fixed, NOx emissions increase as the nozzle diameter increases. The flame length is proportional to the nozzle diameter, and the nozzle exit velocity is inversely proportional to the nozzle diameter with fixed Re_f . Therefore, the residence time increases with increased nozzle

diameter.

Figure 3.8(b) shows EINO_x trends corresponding to those in Fig. 3.8(a). All trends are consistent with NO_x emission shown in Fig. 3.8(a). Only the scales of each fuel composition show discrepancies with NO_x trends. For example, at Re_f of 5000, the EINO_x of the flames are around 9, 1.6, 0.75, and 0.45 for 100/0, 75/25, 50/50, and 25/75% H₂/CO, respectively. The EINO_x is drastically decreased with increasing CO in syngas fuel because of the larger molecular weight (or density) of the syngas fuel with higher CO content. The definition of EINO_x uses the fuel mass consumption as the reference. Hence, the molecular weight (or density) of the fuel has a large effect on the EINO_x value. In fact, the molecular weight of pure hydrogen (2.016 g/mol) is about 10.7 times smaller than that of 25/75% H₂/CO syngas fuel (21.512 g/mol).

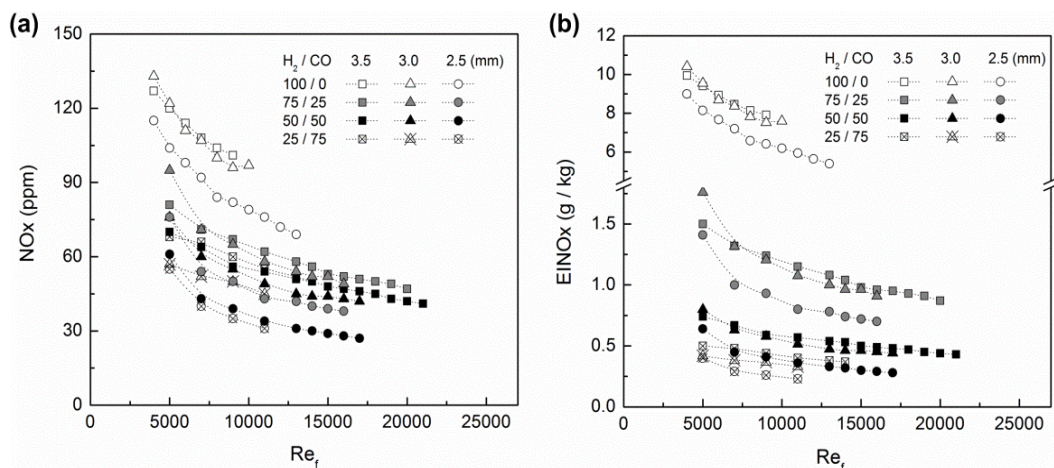


Fig. 3.8 Trends of (a) NO_x and (b) EINO_x depending on Re_f , d_f , and fuel composition.

3.5 EINO_x Scaling of Pure Hydrogen Flame

We applied EINO_x scaling correlations to the dataset of present study for pure hydrogen jet flame. Fig. 3.9 shows the results for the present datasets and those of

Driscoll et al. [36]. The present results showed that EINOx has little dependence on the global strain rate (U_f/d_f^*). This is presumably because the flame length varies according to nozzle exit velocity. As explained in the previous section, Chen and Driscoll's [29] result showed an almost constant flame length with Re_f , whereas the present result shows the flame length increasing with Re . Hence, the scaling proposed by Driscoll et al. [36] satisfies only the flame, which is constant in length with Re_f . Thus, the new parameter is considered for application to the extended range of turbulent jet flames, including both the momentum-dominated and buoyancy-momentum transition regions. In Driscoll's scaling [36], EINOx is normalized by the flame residence time, which is expressed as $L^3/(U_f d_f^{*2})$, that is, the flame volume divided by the fuel volume flowrate. Here, the flame volume is scaled as L^3 , which is based on the assumption that the momentum-dominated jet flame maintains the self-similarity of the stoichiometric mixture fraction field.

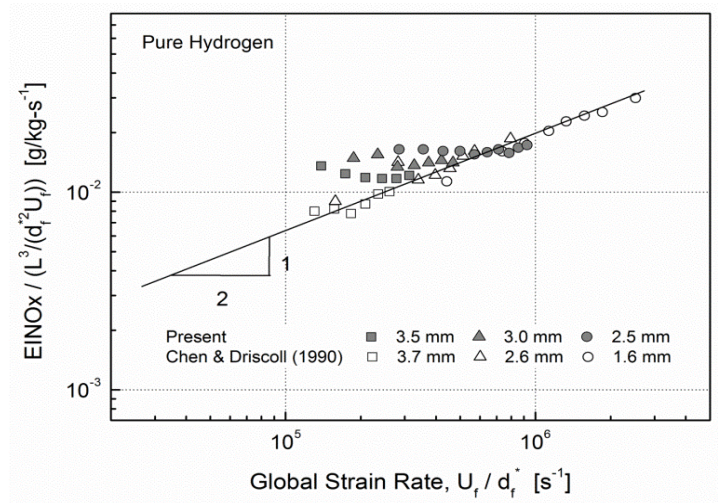


Fig. 3.9 EINOx scaling for pure hydrogen jet flame based on Driscoll et al.'s [36] approach: EINOx divided by flame residence time $L^3/(d_f^{*2}U_f)$ with global strain rate U_f/d_f^* .

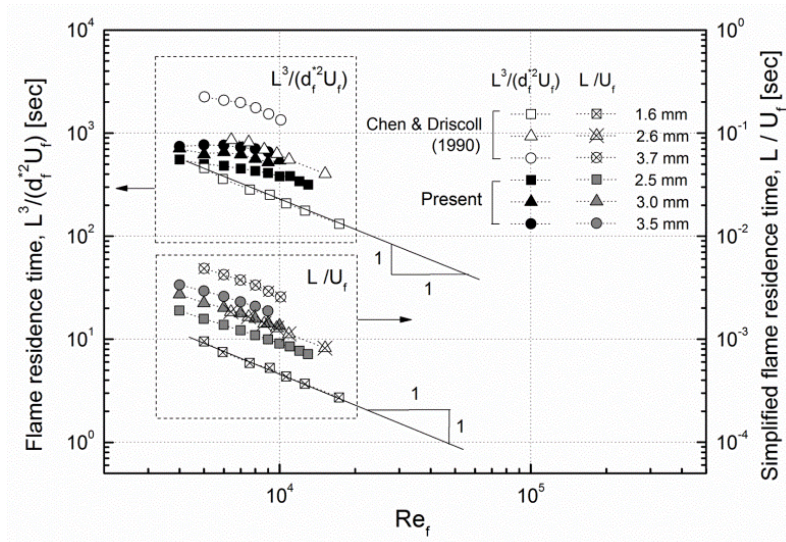


Fig. 3.10 Comparison of previous flame residence time $L^3/(d_f^2 U_f)$ and simplified flame residence time L/U_f for the hydrogen flame data in Chen and Driscoll [29] and in the present study.

However, if buoyancy effects exist in the flame, the similarity cannot be maintained. Thus, the flame residence time is not appropriately scaled in the buoyancy-momentum transition region. Instead of the latter flame residence time, a simplified residence time, L/U_f , is used since the buoyancy affects the flame in the vertical direction. Moreover, if the normalized flame lengths (L/d_f^*) are constant with Re_f (e.g., the results in Chen's study [29]), the flame residence time, $L^3/(U_f d_f^{*2})$, can be also scaled as L/U_f , which is identical to the simplified flame residence time herein introduced. This parameter is consistent with the global residence time referred to in previous studies [33,36,39]. Figure 3.10 shows a comparison of two flame residence time parameters with Re_f . In Chen and Driscoll [29], the previous flame residence time, scaled as $L^3/(U_f d_f^{*2})$, is inversely proportional to the Re_f because the flame length is constant with Re_f , whereas it is rarely decreased with Re_f in the present study. It is possible that L^3 is over scaled and cannot be scaled as flame volume in buoyancy-momentum transition jet because the similarity

cannot be maintained. However, the simplified flame residence time shows decreasing with the slope slightly larger than -1 in the present results. The slight larger slope is presumably caused by increasing flame length by buoyancy effect. Chen and Driscoll's [29] results showed decrease with -1 slope, which was reasonable for both flame residence time parameters since the lengths were constant. This simplified residence time, L/U_f , is applied to the previous scaling (Eq. (3.3)) instead of $L^3/(U_f d_f^2)$. The modified scaling is expressed as follows:

$$\frac{EINO_x}{(L/U_f)} \sim \left(\frac{U_f}{d_f^*} \right)^{1/2} \quad (3.8)$$

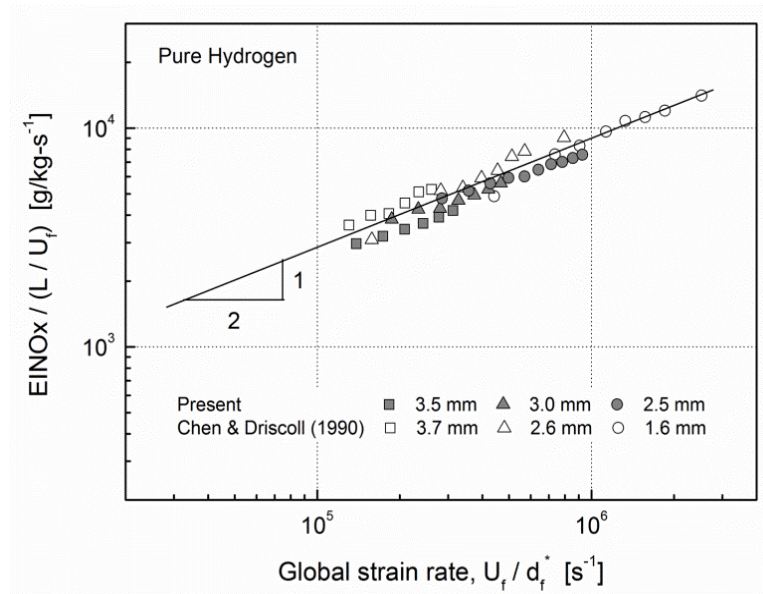


Fig. 3.11 Modified EINO_x scaling for pure hydrogen jet flame: EINO_x divided by simplified flame residence time L/U_f with global strain rate U_f/d_f^* .

Figure 3.11 shows the modified scaling for H₂ jet flame results in Chen and Driscoll [29] and those of the present study. The datasets in Chen and Driscoll [29] are in reasonable alignment with the modified scaling. Moreover, the results of present study are also aligned well with the new scaling, in spite of the increased flame length with increased fuel velocity. It is here thought that the new scaling satisfies the turbulent syngas jet flame, which is in buoyancy-momentum transition region as well as momentum-dominated region. The scaling shows well the relationships of the EINO_x, the flame residence time, and the global strain rate for the thermal NO_x dominant turbulent jet flames, regardless of the presence of buoyancy.

3.6 EINO_x Scaling of H₂/CO Syngas Flames

Figure 3.12(a) shows the EINO_x scaling in Driscoll et al. [36] for the H₂/CO syngas jet flames investigated in the present study. It was found that the normalized EINO_x increases with the global strain rate. The datasets are grouped according to the fuel compositions. However, for each composition, the datasets are not in good agreement with the 1/2-power curves. Discrepancies between the datasets and the scaling curves are slightly reduced as the CO content in the syngas fuel increase, since the flame is close to the momentum-driven region. Nevertheless, they are not in good agreement with the 1/2-power curves. Figure 3.12(b) shows the proposed modified scaling (Eq. (3.8)) for the syngas jet flames. From the least-squares fitting, the correlation coefficients (R²) shows that it is well scaled with high H₂ content fuels and relatively poorly scaled with high CO content fuels. In spite of the relatively poor R² in higher CO contents fuels, it is found that the scaling aligns well with the results of this study. Consequently, the simplified residence time is a better parameter than the previous residence time for the scaling of syngas jet flames in buoyancy-momentum transition region. However, the scaling cannot collapse the datasets of all fuel compositions into a single line. The constants of the scaling of each fuel composition are 8.1, 1.8, 0.95, and 0.65, respectively.

Some parameters affecting EINO_x levels were considered in order to collapse the

distributed 1/2-power scaling of syngas jet flames. First, we considered the flame temperature variation with respect to the fuel composition. According to the thermal NOx analysis in Peters and Donnerhack [33], EINOx is proportional to the NO production rate, which depends on the gas temperature. Thus, the flame temperature governs the NOx production rate. However, stoichiometric flame temperatures of H₂ and CO at STP condition (1 bar, 300 K) are almost the same, and those of syngas fuels are also almost the same, as shown in Table 3.2. Hence, the effects of flame temperature on NOx production with respect to each syngas fuel composition could be excluded. Moreover, an appropriate reference was considered. EINOx is defined using fuel mass consumption as a reference. However, it is inappropriate to compare each composition because the mass consumptions of air, the nitrogen source for thermal NOx, with respect to the fuel compositions are not the same. Therefore, we propose that the mass flowrate of air participating in the reaction should be the reference, not the mass flowrate of the fuel. Figure 3.13(a) shows a conceptual schematic of the process of N₂ consumption and NOx production. NOx production depends on amount of N₂ that passes the hot reaction zone. If m_f kg of fuel participate in the reaction, $m_{a,st}$ kg of air participates in the reaction, thus forming the stoichiometric condition. Therefore, in NOx scaling, NOx production per N₂ consumption (m_{NOx}/m_{N_2}) should be considered, not per fuel consumption ($m_{NOx}/m_f = EINOx$). The N₂, source of the thermal NOx, included in the air is proportional to the amount of air participating in the reaction ($m_{N_2} \sim m_{a,st}$). The NOx production per N₂ consumption can be expressed as follows:

$$\frac{m_{NOx}}{m_{N_2}} = \left(\frac{m_{NOx}}{m_f}\right) \cdot \left(\frac{m_f}{m_{N_2}}\right) \sim \left(\frac{m_{NOx}}{m_f}\right) \cdot \left(\frac{m_f}{m_{a,st}}\right) = EINOx \cdot \frac{1}{f_{st}} \quad (3.9)$$

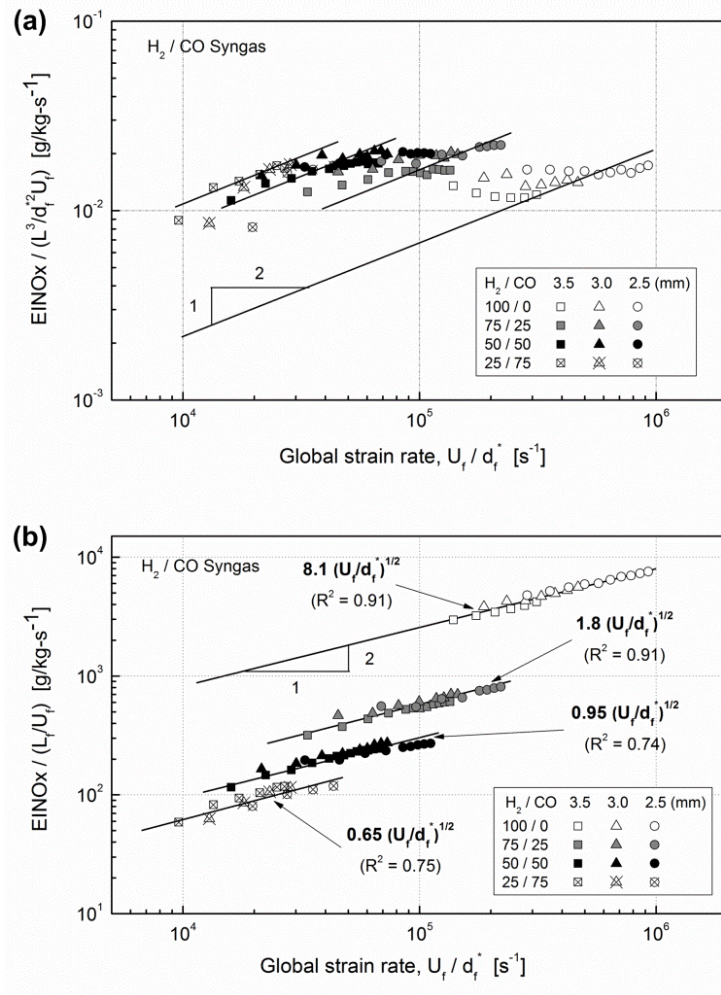


Fig. 3.12 EINOx scaling for H_2/CO syngas jet flame (a) Scaling based on Driscoll et al.'s [36] approach: EINOx divided by flame residence time $L^3/(d_f^{*2}U_f)$ with global strain rate U_f/d_f^* (b) Modified scaling: EINOx divided by simplified flame residence time L/U_f with global strain rate U_f/d_f^* .

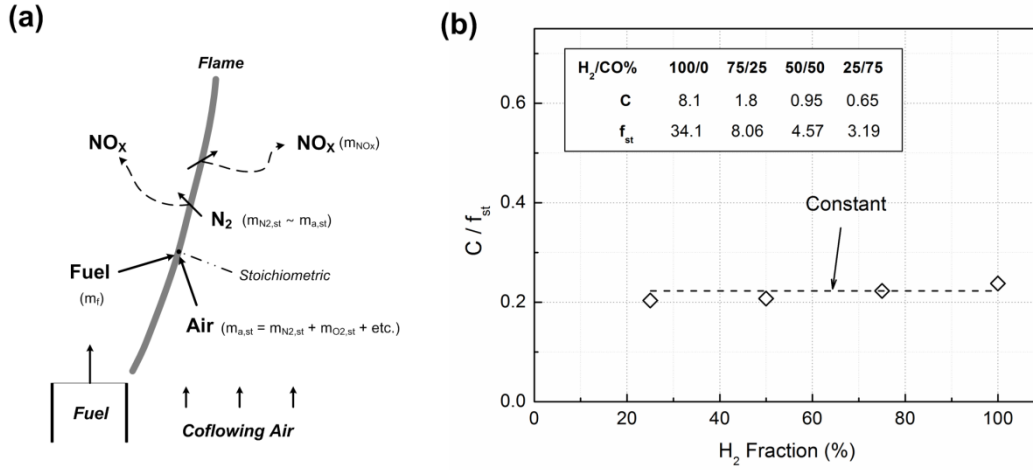


Fig. 3.13 (a) Conceptual schematic of relationship between nitrogen consumption and NO_x production, (b) Constant C/f_{st} according to H₂ fraction in syngas fuel.

The scale differences according to fuel composition, as shown in Fig. 3.12(b), could be resolved by applying the latter parameter ($EINO_x/f_{st}$) instead of $EINO_x$. Figure 13(b) shows that the scales divided by f_{st} (i.e., C/f_{st}) are almost constant for all fuel composition. Consequently, applying $EINO_x/f_{st}$ could collapse all datasets into a single line. The scaling applied $EINO_x/f_{st}$ is expressed as follows:

$$\frac{EINO_x}{(L/U_f)} \cdot \left(\frac{1}{f_{st}}\right) \sim \left(\frac{U_f}{d_f^*}\right)^{1/2} \quad (3.10)$$

Figure 3.14 shows the datasets for syngas fuels in the present study with the modified scaling. All datasets are in good agreement with the 1/2-power curve and are collapsed into a single line. Moreover, the correlation coefficient (R^2) of 0.98 shows that the scaling predicts all the datasets extremely well.

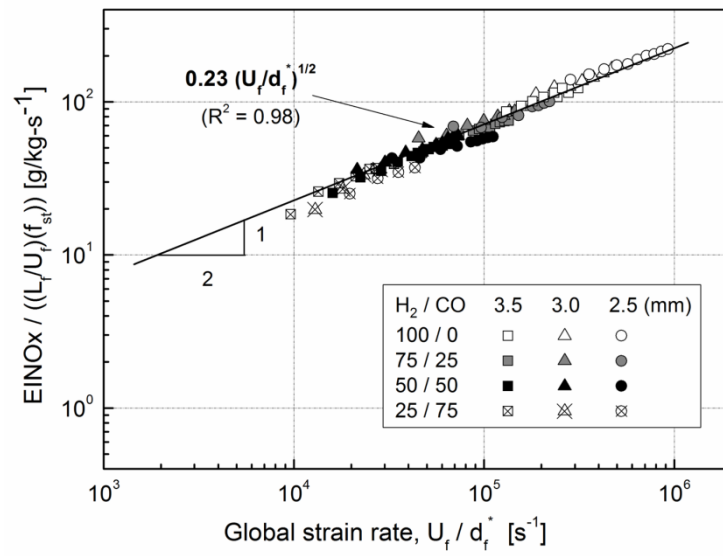


Fig. 3.14 Modified EINO_x scaling for H₂/CO non-premixed turbulent jet flame: EINO_x/f_{st} divided by simplified flame residence time L/U_f with global strain rate U_f/d_f^* .

CHAPTER 4

STABILITY CHARACTERISTICS OF H₂/CO SYNGAS TURBULENT NON-PREMIXED JET FLAMES

4.1 Background and Objectives

The recent development of Integrated Gasification Combined Cycle (IGCC) plants for power generation has stressed the importance of better understanding the combustion characteristics of synthetic gas, a.k.a. syngas, a gaseous blend with hydrogen and carbon monoxide as primary components. Extensive and intensive experimental investigations have followed, especially focused on the fundamental combustion properties of such blends, including for instance, laminar [8-10] and turbulent [11,12] flame velocities, autoignition propensities [13-15] and the underlying chemical kinetic aspects [5-7]. Applied research has not been at rest, and much progress has been achieved in the flame dynamic area with numerous contributions stemming from Gas Turbine (G.T.) model combustor studies (e.g. flame stability and combustor performances [20-22]). Although a large body of work has been dedicated to the lean premixed combustion mode, the high reactivity of hydrogenated fuels and the inherent risks for the G.T. hardware have rendered non-premixed combustion of syngas fuels more attractive. The need of flaring gases in IGCC units to ensure safe operation during gasifier start-up/shutdown and emergency situations equally underlines the necessity of leading comprehensive investigations on syngas turbulent diffusion flames.

Table 4.1 Summary of milestone investigations related to jet flame stability characterization (*: shroud size not mentioned in the graphs, **: high temperature 300-1000 K, ***: 0.2 and 1.2 mm fuel nozzle → 2 deg. tapered on the outside).

Authors / Year / Ref.	Diagnostics	Fuel Jet	Coaxial Jet	d_f {mm}	l {mm}	d_a {mm}	U_f {m/s}	U_a {m/s}	Additional Comments
Vranos et al. – 1968 [28]	Direct visualization	H ₂	Air	1.7 → 8.2	0.07 → 1.1	27.6, 48.8	Up to ~1200	×*	<ul style="list-style-type: none"> For small lip thicknesses (0.07 → 0.39 mm), residual flame not observed at blowoff. In the region of residual and full-bodied flame, an eddy system exists in the injector lip.
Takeno and Kotani – 1975 [29]	Schlieren	City Gas, H ₂	Air**	1	0.5	100	< 1400	5-50	<ul style="list-style-type: none"> Stability phenomena found to be very sensitive to the burner rim thickness.
Mizutani and Yano – 1978 [30]	Mie scattering, Thermocouple, Hot wire anemometry, G.C.	CH ₄ , C ₃ H ₈	Air	7.6	0.5 → 6	50	< 11.5	< 5	<ul style="list-style-type: none"> Air/fuel side counter-rotating eddies in the nozzle rim wake.
Takahashi et al. – 1985 [32]	LDV	H ₂ /N ₂ , H ₂ /Ar, H ₂ /He	O ₂ /N ₂ , O ₂ /Ar, O ₂ /He	2.39, 3.99	< 0.08	150	< 800	< 0.2	<ul style="list-style-type: none"> Coaxial air channel open 30 mm below the jet exit to enhance entrainment. Critical mean jet velocity found to be independent of the fuel nozzle I.D.
Takahashi and Schmoll – 1991 [33]	LDV	CH ₄	Air	9.45	0.2, 1.2, 2.4***	26.92	< 23	< 4.4	<ul style="list-style-type: none"> Lip thickness of the fuel tube identified as a “critical factor” governing the flame stability type.
Takahashi et al. – 1991 [34]	Schlieren, Direct visualization	H ₂	Air	0.6 → 5	0.02, 0.03, 0.04	100, 150	< 700	< 40	<ul style="list-style-type: none"> Marked effect of the fuel nozzle I.D. on the critical velocities Marked effect of the air nozzle size on the critical velocities → importance of the velocity gradient in the coaxial air boundary layer Negligible effect of the flame confinement
Present study	Direct visualization, OH* Chem.	H ₂ , H ₂ /CO	Air	3	0.45, 0.9	10.1, 12.4, 15	< 450	< 65	

The global combustion characteristics of turbulent non-premixed jet flames have been widely reported, especially for attached and lifted jet flames of common hydrocarbons [49-52]. If many studies devoted to single jet flames can be found in the literature, less research has been focusing on the stability characteristics of jet flames with coaxial air, although widely required for the safe operation of conventional non-premixed combustors. The literature review, hereafter provided, recalls the milestone contributions in this area, with an emphasis on both single and coaxial jet flames of hydrogen, cases that are essential to the understanding of syngas jet flame combustion. The studies of interest are listed in the Table 4.1 along with their associated experimental parameters. The pioneering study of Vranos et al. [53] investigated flames of concentric air and hydrogen jets with the injector diameter and lip thickness as primary geometric variables. Flames of various nature were identified (e.g. aerated, full-bodied, residual-rim or lifted flames) and obtained stability limits were qualitatively discussed with an emphasis on the preponderant role of the air/fuel molecular diffusivity, air/fuel boundary layers and injector lip thickness in the flame stabilization process. Takeno and Kotani [54] subsequently reported stability limits of city gas and hydrogen jet flames developed in a high temperature coflowing stream of air. Two distinct stability limits were observed, including: 1/ blowoff of the rim-stabilized flame, 2/ break-off or extinction of the turbulent portion of the flame at the transition point from laminar to turbulent flow. The attachment mechanisms of jet diffusion flame with a coaxial flow were investigated by Mizutani and Yano [55] for methane and propane fuels. The role and importance of counter-rotating eddies developed in the nozzle rim wake were further analyzed. A mechanistic interpretation of the flame stability characteristics (i.e. blowoff, blowout) is proposed for the thick rim cases based on the flame-eddies interactions in the nozzle rim wake. For thin rim thicknesses ($l < 2\sim 3$ mm for methane and $l < 1\sim 2$ mm for propane), flames were found to stabilize above the recirculation zones, presumably by the flame propagation mechanism highlighted in the early works of Vanquickenborne and Van Tiggelen [56]. Not including coaxial cases, nevertheless of noticeable importance, is the seminal investigation of Takahashi and coworkers [57] that analyzed the stability of

single jet flames of pure hydrogen and hydrogen/diluents blends. Critical fuel jet velocities (i.e. the fuel velocity at which blowoff or liftoff first occur) were measured for various fuel jet compositions and a simple flame stability model, based on the local balance of the burning and incoming reactant velocities at the flame base, was proposed. The latter model essentially relies on the assumption that fuel and air premixing occurs in a “dark space” between the flame base and the nozzle burner and hence, that a premixed laminar flame ahead of the diffusion zone governs the stability characteristics of the turbulent flame. The detachment (“lifting”) mechanisms of methane jet flames with coaxial air were subsequently studied and categorized by Takahashi and Schmoll [58]. They reported three types of distinct mechanisms, including: 1/ the flame base stability lifting, based on the afore-described balance between flame and incoming stream velocities, 2/ the local flame extinction lifting. The latter is controlled by the local flame extinction at the break point of the reactive jet due to shear-generated vortices; 3/ the lean-limit extinction lifting, essentially controlled by the flame holding in the immediate wake of a thick-rim fuel tube. While the type 1 was observed for thin and moderate rim thicknesses ($l = 0.2$ mm and 1.2 mm respectively), type 2 and 3 appeared at large rim thicknesses ($l = 2.4$ mm). Similar investigations were led by Takahashi and coworkers for hydrogen/coaxial air jet diffusion flames [59]. Flame stability limits performed on sharp-edged fuel tubes could be classified in four categories, including: 1/ a jet entrainment-controlled region (low coaxial air velocity), 2/ a coaxial air-controlled region, 3/ a turbulent-laminar transition region, and 4/ a laminar flame region (low fuel velocity). The velocity gradient of the incoming air stream in the vicinity of the burner rim was identified as a correlating variable for the flame stability limit data.

Although several studies have been dedicated to the detailed structure of non-premixed jet flames of syngas mixtures with or without coaxial streams [60-62], systematic investigations of their global stability characteristics are rather scarce. It is clear from the afore-detailed review that these characteristics are strongly depending on the burner geometry and fuel type that are considered. Thus, syngas jet flame stability limits cannot be directly inferred from those of the “better-known” hydrogen jet flame.

The present study hence focuses on the determination of the detachment stability (blowoff, liftoff)* of attached jet flames using a well-defined burner design. The influence of the syngas composition, coaxial burner geometry and fuel/air stream velocities is analyzed in detail. Critical fuel velocities $U_{f,c}$ are first reported for single jet flames at various syngas compositions. Effects of the coaxial shroud size and fuel nozzle rim thickness are further investigated in the case of a pure hydrogen jet flame. At last, the stability limits of syngas jet flames with coaxial air are reported. In order to qualitatively understand the detachment mechanisms of the syngas flames, OH^* chemiluminescence imaging near the stability limits is conducted. Flame behaviors at the stability limits are accordingly discussed.

4.2 Experimental Methods

Experiments were performed in a rectangular-shaped combustor, shown in Fig. 4.1. The latter was equipped with four large quartz windows to provide convenient optical access to the flame. The axisymmetric fuel nozzle was located at the bottom center of the combustor and was surrounded by the coaxial air shroud. The fuel nozzles were made of stainless steel with an inner diameter d_f of 3.0 mm and two different rim-thicknesses l , measuring respectively 0.45 and 0.9 mm. The coaxial air nozzles, made of brass, had inner diameters d_a respectively equal to 10.1, 12.4, and 15.0 mm. A coflowing air stream, controlled by a choked orifice (4 mm diameter, 45 degree-tapered), was supplied from the bottom plane around the fuel and coaxial nozzles in order to maintain lean conditions in the combustor. The coflowing stream was passed through several layers of honeycombs (~ 3 mm hexagonal mesh) and its output velocity was set to be lower than 0.2 m/s to avoid any perturbing effect in the combustion area of interest.

* In the present investigation, “blowoff” corresponds to the flame detachment from the burner rim directly followed by extinguishment. On the other end, “liftoff” is observed when the flame detaches from the burner rim and re-stabilizes further downstream where favorable flow conditions are met.

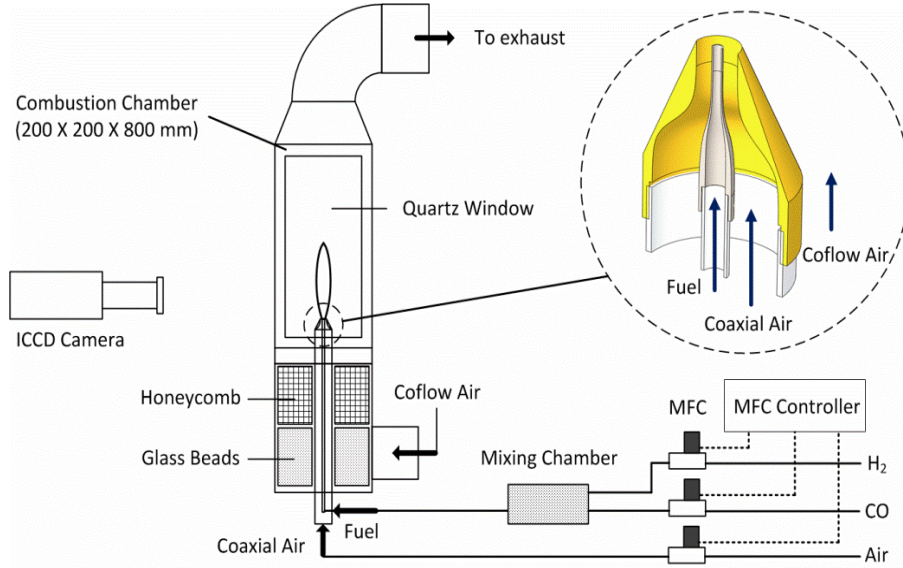


Fig. 4.1 Schematics of the experimental apparatus and the nozzle geometry (dotted circle).

The combustible gases (Air liquide, 99.95% purity) and in-house compressed air were individually metered using calibrated thermal mass flow controllers (Brooks 5851S/5853S). Hydrogen and carbon monoxide were supplied through a mixing chamber filled with 3 mm diameter glass beads for mixing enhancement.

All experiments were performed at least twice to ensure repeatability. The flame detachment events were performed at fixed fuel velocity, while the air velocity was slowly increased until blowoff/liftoff occurred. Both fuel and coaxial air jets were injected at turbulent conditions ($Re > 3500$), the corresponding Reynolds numbers Re_f and Re_a being defined as:

$$Re_f = \frac{U_f \cdot d_f}{\nu_f} \quad (4.1)$$

with U_f the fuel jet exit velocity and ν_f the fuel kinematic viscosity, and

$$Re_a = \frac{U_a \cdot \{d_a - (d_f + 2 l)\}}{2 \nu_f} \quad (4.2)$$

with U_a the coaxial air exit velocity and ν_a the air kinematic viscosity. The operating conditions for the syngas jet flames with coaxial air are reported in Table 4.2.

Table 4.2 Experimental conditions for syngas jet flames with coaxial air ($d_f = 3.0$ mm and $d_a = 12.4$ mm).

H₂/CO (Vol. %)	100/0	90/10	80/20	75/25	70/30	60/40	50/50
U_f (m/s)	130 - 410	110 - 290	70 - 230	65 - 200	60 - 200	50 - 160	40 - 130
$Re_{f,min}$	3550	4490	3650	3760	3830	3820	3610
$Re_{f,max}$	11200	11840	12000	11510	12750	12210	11720
U_a (m/s)				17.1 – 69.5			
Re_a				4490 - 13490			
U_{co} (m/s)				< 0.2			

Figure 4.2 shows the typical appearance of the syngas jet flames for different H₂/CO contents. For the pure H₂ case (a), the upstream region of the flame appears light blue while the downstream one is found to be markedly red. The blue and red emissions can be respectively attributed to the existence of a weak violet/blue continuum ($\lambda \sim 400\text{-}500\text{ nm}$), presumably due to reactions between radical species (e.g. H, OH) [44] and a strong continuum in the near IR region ($\lambda > 650\text{ nm}$) due to vibrationally excited water molecules [43,44]. As the CO content is increased, the flame luminosity successively shifts to bright blue (case b) to almost white (case c). This luminescence change can be attributed to the enhanced formation of CO₂^{*} radicals known for their broadband emission across the entire spectrum of visible wavelengths (340 ~ 650 nm) [64].

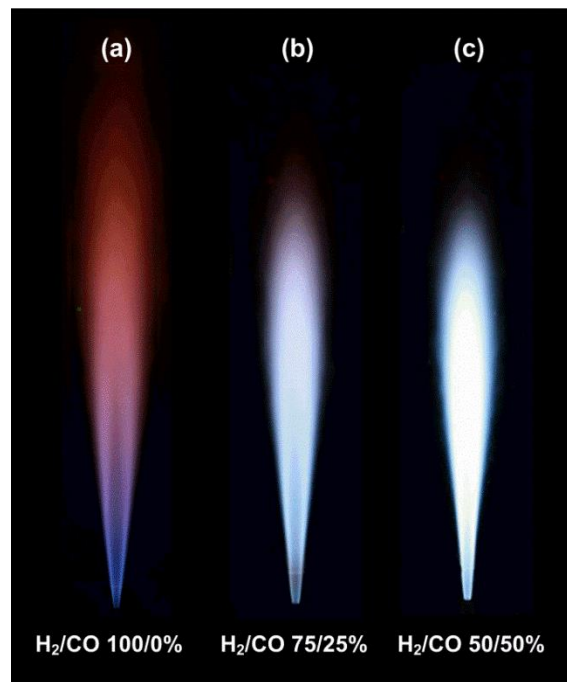


Fig. 4.2 Syngas jet flame luminescence photographs: (a) pure H₂, (b) 75/25, and (c) 50/50 H₂/CO%.

The flame chemiluminescence images were acquired with a UV-Nikkor objective ($f = 105$ mm; $f/4.5$) equipped with dedicated filters (WG-305 and UG-11) and mounted on an ICCD camera (PI-MAX, Princeton Instruments Inc., 512×512 pixel CCD). The exposure time was set to 100 msec and 10 images were acquired and averaged. The region of interest corresponds to a 12.1×12.1 mm area located near the nozzle exit. The spatial resolution is $23.6 \mu\text{m}$ in all cases.

4.3 Single Jet Flames of Syngas

Figure 4.3(a) shows the critical fuel jet velocities versus fuel hydrogen mole fraction for single jet flames of syngas. The results of Takahashi et al. [57] for nitrogen/argon/helium-diluted hydrogen flames are reported as well. Helium case aside, all datasets display the same qualitative trend. Critical fuel velocities are characterized by a moderate linear increase up to 90% of hydrogen followed by a sharp increase in the last 10%. $U_{f,c}$ values for pure hydrogen in air ($\sim 530 \text{ m}\cdot\text{s}^{-1}$) agree well for both experimental studies. Additional insight can be gained if the present results are analyzed in the framework of the simplified stability model proposed by Takahashi and coworkers [57]. To further substantiate the flame/flow velocity balance concept developed in that work [57], evolutions of the maximum laminar premixed flame velocity $S_{u,max}$ are plotted in Fig. 4.3(b). It is seen that the $S_{u,max}$ curves do not strictly correlate with the reported critical fuel velocities, especially at higher hydrogen contents. It is here thought that an additional parameter affects the critical fuel velocity evolution such as reported in Fig. 4.3(a). In the course of the present study, it was observed that the flame base locations were markedly different depending on the syngas mixture compositions, even if jet fuel velocities were matched. Flame bases were located closer to the air/fuel side for higher/lower hydrogen content fuel respectively. Provided that the flame base is at stoichiometric conditions, this observation underlines the importance of the stoichiometric air to fuel mass ratio $(m_a/m_f)_{st}$.

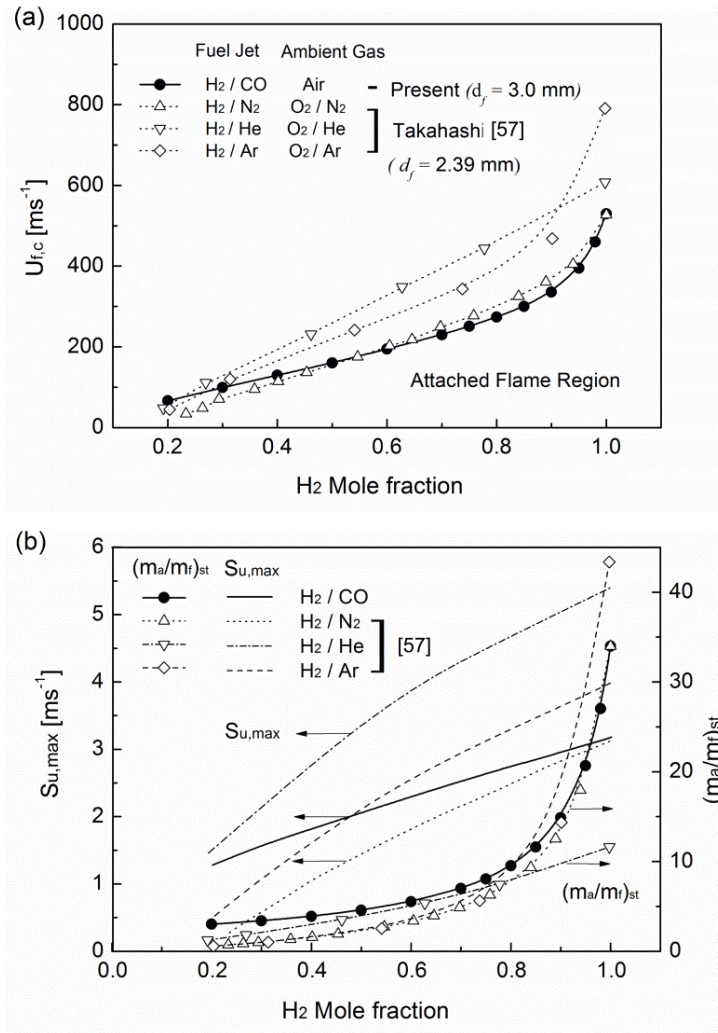


Fig. 4.3 Single jet flame stability of syngas fuels: (a) Critical fuel jet velocity versus hydrogen mole fraction in the fuel jet, (b) Maximum laminar flame speed ($S_{u,max}$) and air to fuel mass ratio at stoichiometric condition ($(m_a/m_f)_{st}$) versus hydrogen mole fraction in the fuel jet.

Figure 4.4 shows the conceptual schematic of flow velocity at the flame base for three different $(m_a/m_f)_{st}$ cases (see a, b and c). If the $(m_a/m_f)_{st}$ ratio is large (case c), a large amount of air is needed to achieve stoichiometric conditions. As a result, the flame base is located closer to the air side where the incoming flow velocity is significantly lower than the core velocity of the fuel jet. Hence, the flame can be stabilized at higher fuel jet velocities which shed the light on the steep $U_{f,c}$ increases observed in Fig. 4.3(a). As shown in Fig. 4.3(b), evolutions of the $(m_a/m_f)_{st}$ ratios clearly correlate with the critical fuel velocities presented in Fig. 4.3(a), thus confirming the importance of the flame base location in the flame stabilization process. For lower $(m_a/m_f)_{st}$ cases (case a), $U_{f,c}$ and $S_{u,max}$ curves readily correlate (smooth linear increases with the hydrogen mole fraction) which suggests that the flame stability limit is merely sensitive to the flame base location.

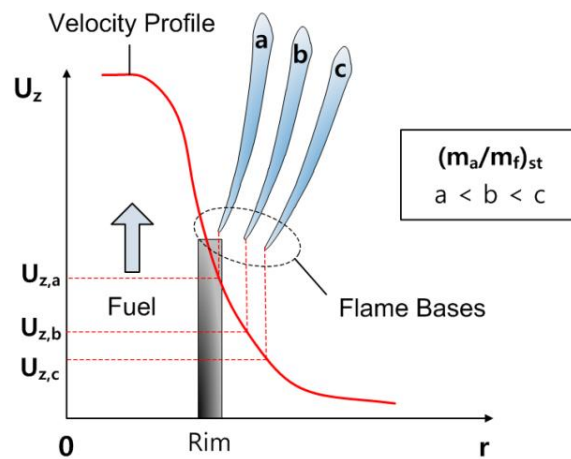


Fig. 4.4 Conceptual schematic of the flame base location depending on the $(m_a/m_f)_{st}$ ratio.

4.4 Jet Flames with Coaxial Air Jet

4.4.1. Hydrogen Flames

Figure 4.5 shows the stability limits of pure hydrogen jet flames with coaxial air for different shroud sizes. Several regions can be distinguished on the stability map, including: 1/ the attached flame region, where the flame is anchored to the nozzle rim, 2/ the lifted flame region, where the flame is stabilized at a distant point from the nozzle exit, and 3/ the blowoff/blowout region where the attached/lifted flames are respectively blown-off/blown-out. Appearances of the hydrogen jet flame are shown in Fig. 4.6(a) for a fixed fuel velocity of 370 m/s. The attached flame with coaxial air (2) is shorter than the single jet flame (1) due to fuel-air mixing enhancement. A further increase in the coaxial air leads to the flame liftoff (3).

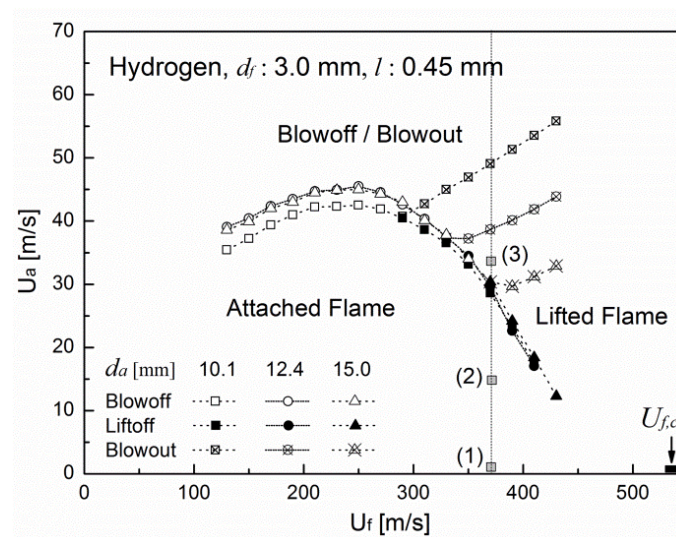


Fig. 4.5 Stability limits of pure hydrogen jet flames with coaxial air for various air shroud sizes ($d_a = 10.1, 12.4, \text{ and } 15.0 \text{ mm}$).

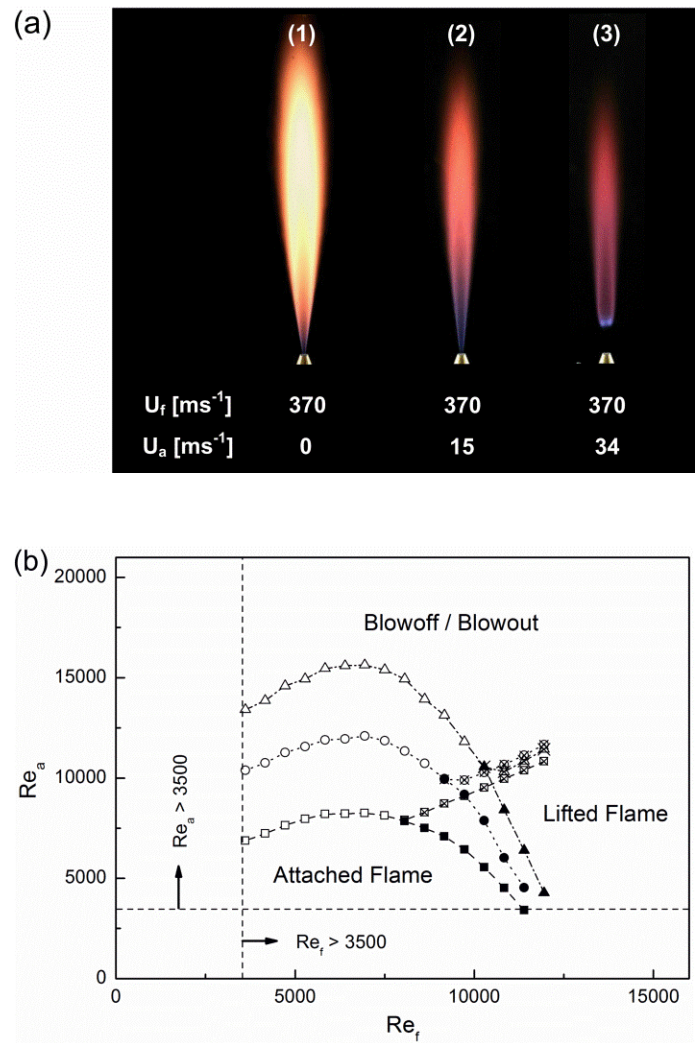


Fig. 4.6 (a) Flame appearances including: 1/ attached single jet flame without coaxial air, 2/ attached flame with coaxial air, 3/ lifted flame, (b) Stability limits in terms of air/fuel Reynolds numbers (Legend: same as Fig. 4.5).

As shown in Fig. 4.5, the detachment characteristics of the hydrogen flame are almost independent of the air nozzle diameter d_a , hence showing that the turbulent state of the coaxial stream (hereby quantified by the Reynolds number Re_a based on the coaxial jet exit conditions) does not significantly influence the reported stability limits. This fact is substantiated by the early experimental investigations of Takahashi et al. [65] and Takeno and Kotani [54] in which residual laminar flames were observed at the base of fully turbulent jet flames of hydrogen. Clearly, local flow characteristics in the direct vicinity of the fuel nozzle wake govern the stability behavior of such flames. Note here that discrepancies in the stability limits of hydrogen jet flames have been previously reported by Takahashi et al. [59] for large air shrouds ($d_a = 100$ and 150 mm). These discrepancies were presumably due to different velocity gradients developed in the boundary layers of the coaxial streams [59]. The stability limits shown in Fig. 4.5 are re-plotted in Fig. 4.6(b) with the Reynolds numbers Re_f and Re_a as primary variables. Interestingly, the blowout limits of the lifted flames (crossed symbols) almost collapse into a single line. This result is sound if one considers that jet flame blowout stabilities are essentially governed by far field turbulence characteristics, as discussed by Dahm and Mayman [66].

Figure 4.7 shows the rim thickness effect on the detachment stability of pure hydrogen flames with coaxial air. The datasets reported by Vranos et al. [53] and Takahashi et al. [59] are added as well. Given the differences in the experimental apparatuses, the present results agree surprisingly well with those reported in ref. [53]. So do the datasets of refs. [53] and [59] for small rim thicknesses. In overall, it can be noticed that the stability limits are strongly dependent on the burner rim thickness. Thicker rim results (0.39 and 0.71 mm in previous work [53], 0.45 and 0.9 mm in the present study) show that the stability limits are non-monotonic. As the rim thickness increases, it is hypothesized that a larger fuel flux is entrained in the recirculation zone formed in the wake of the burner rim. Hence, a larger flux of air is needed to reach the flame lean extinction limit and the flame is consequently sustained at higher coaxial air velocities. A similar argument can be used to qualitatively interpret the increasing

branches of the stability curves at a fixed rim thickness: as U_f increases, more fuel is entrained in the burner rim wake and lean-limit extinction conditions are only met for higher air inputs, i.e. higher coaxial air velocities. If this simple mechanism is supported by the early observations of Takahashi and coworkers [58] for methane/air diffusion flames (mechanism governing the “Type III” limit [58]), the resulting detachment event does not lead to a lifted flame configuration. We finally note that the present interpretation only holds for the increasing branch of the stability curves since the non-monotonic trends observed in Fig. 4.7 clearly indicate a change in the flame detachment mechanism involved at higher fuel velocities. This will be further discussed in the next section.

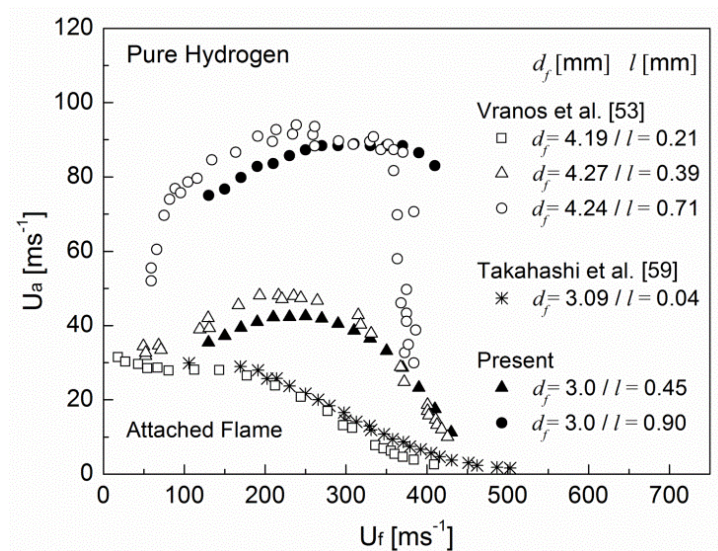


Fig. 4.7 Detachment stability limits of hydrogen jet flames with coaxial air for various fuel nozzle rim thicknesses.

In the case of thin rim thicknesses ($l < 0.21$ mm), the flame detachments occur at lower coaxial air velocities and display a monotonic decreasing behavior. In this particular case, the detachment mechanism should be significantly different from the

afore-described one, and a marked dependence of the stability limit on the reactant inter-diffusion characteristics is to be expected.

4.4.2. H₂/CO Syngas Flames

The detachment stability limits of attached syngas jet flames are shown in Fig. 4.8 for $d_a = 12.4$ mm and $l = 0.45$ mm. The critical fuel velocities for the single jet flame cases are reported as well (see crossed symbol for $U_a = 0$ m/s). Akin to the pure hydrogen case, bell-shaped stability curves are obtained for all syngas compositions. As the CO mole fraction increases, the stability curves drift to the left and upward. The motion to the left is related to the critical fuel velocity decrease at increasing CO content, itself presumably governed by the respective $S_{u,max}$ and $(m_a/m_f)_{st}$ ratio of the considered fuel/air blend, as discussed in section 3.1. On the other hand, the upward motion seems to be related to the progressive increase of the fuel jet mass flux, as further illustrated hereafter.

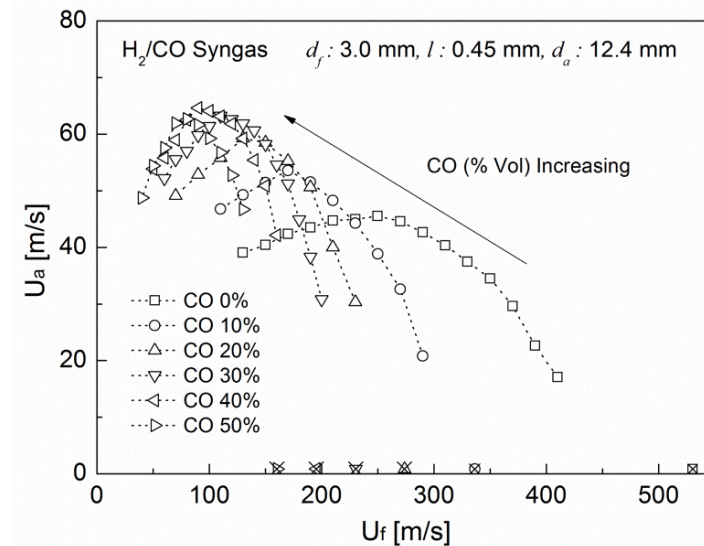


Fig. 4.8 Detachment stability limits of syngas jet flames with coaxial air ($d_f = 3.0$ mm, $l = 0.45$ mm, and $d_a = 12.4$ mm); crossed symbols are the stability limits for the single jet flame cases (see $U_a = 0$ m/s).

OH^* chemiluminescence images near the detachment limits are shown in Fig. 4.9. The images were taken at four different velocity conditions along the stability curves (see A to D) for three different fuel compositions, including: (a) pure hydrogen, (b) 75/25, and (c) 50/50 H_2/CO .

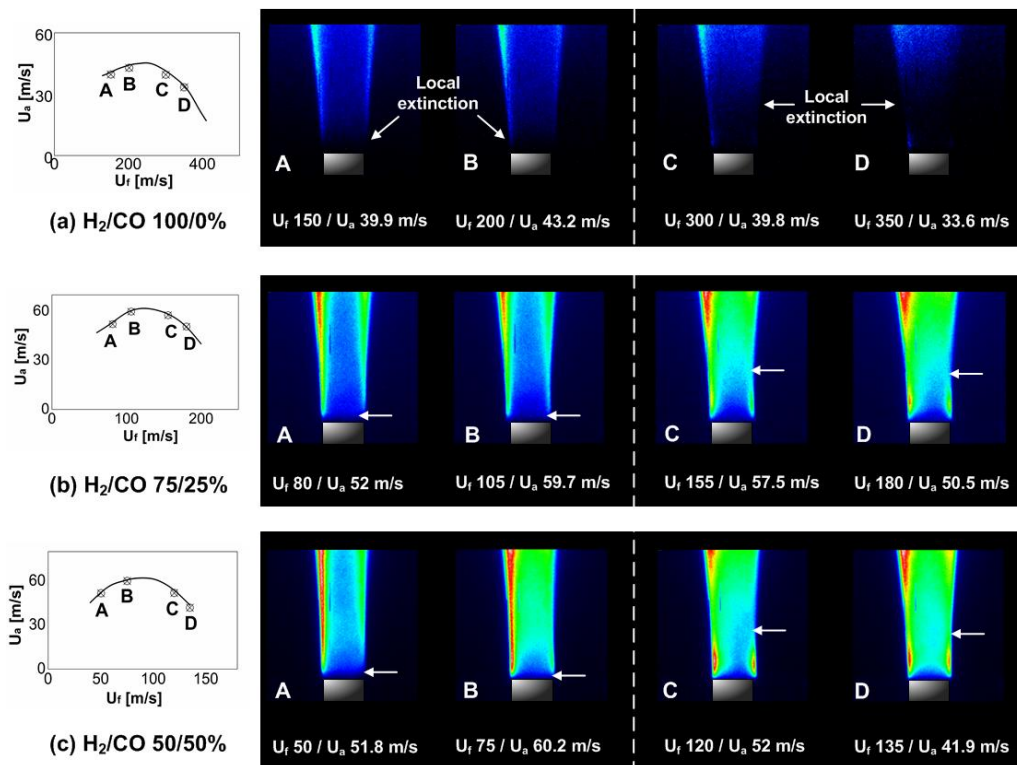


Fig. 4.9 Averaged OH^* chemiluminescence images near the nozzle exit for the: (a) 100/0% H_2/CO , (b) 75/25% H_2/CO , and (c) 50/50% H_2/CO jet flames (Region of interest: 12.1×12.1 mm, $d_f = 3.0$ mm, $l = 0.45$ mm, and $d_a = 12.4$ mm). White arrows show the region of local extinction.

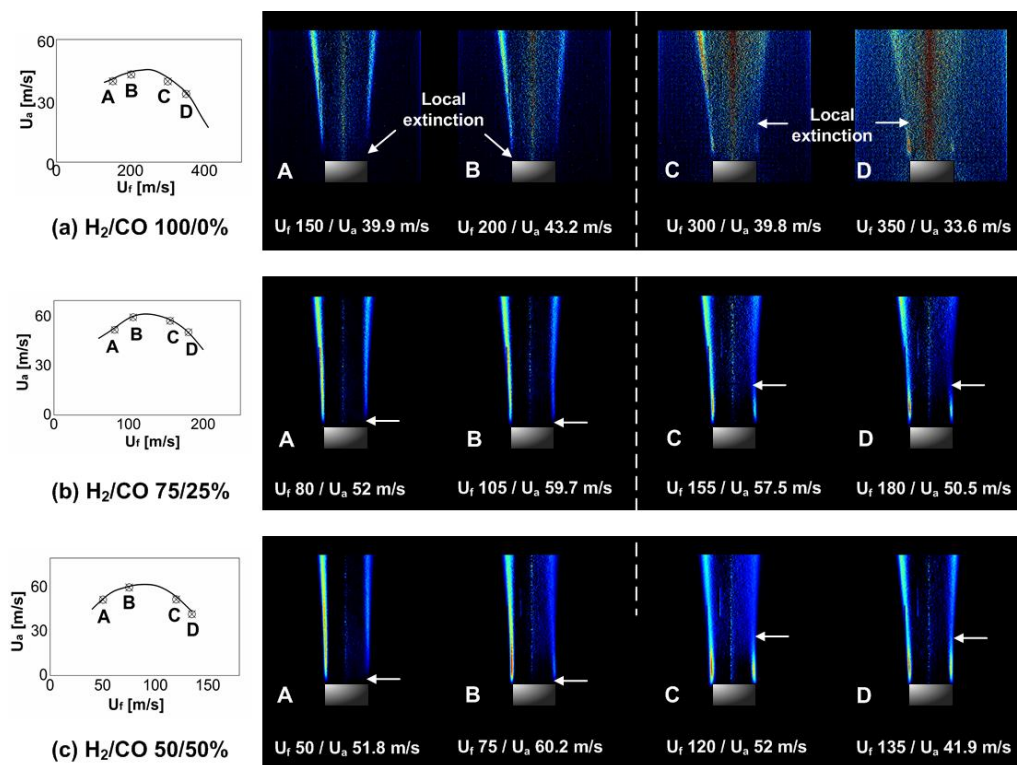


Fig. 4.10 Inverse Abel transformed images of the averaged OH^* chemiluminescence images in Fig 4.9: (a) 100/0% H_2/CO , (b) 75/25% H_2/CO , and (c) 50/50% H_2/CO jet flames (Region of interest: 12.1×12.1 mm, $d_f = 3.0$ mm, $l = 0.45$ mm, and $d_a = 12.4$ mm). White arrows show the region of local extinction.

Moreover, the inverse Abel transformed images corresponding to Fig. 4.9 are shown in Fig. 4.10. The points A-B and C-D are respectively located on the increasing and decreasing branches of the stability curves. The OH^* chemiluminescence signals are found to be slightly asymmetric due to infinitesimal alignment imperfections introduced while centering the coaxial nozzles. Both sides of the recorded flames show however the same qualitative trend. It is observed that the flame behaviors for A and B and those for C and D are significantly different (see white arrows). In the case of A and B, local extinction of the flame close to the fuel nozzle rim is observed. For C and D, however, local extinction of the flame is found downstream of the nozzle ($\sim 1.5 d_f$), while an annular flame remains in the nozzle rim wake. It is here thought that the flame detachment mechanism characterizing the increasing stability branch is mainly controlled by the lean flammability limit of the fuel/air mixture formed at the flame base, as originally described by Takahashi et al. [58]. As the coaxial air velocity increases, the local equivalence ratio in the rim wake vicinity decreases until lean extinction conditions at the flame base occur. The flame base, presumably sustained by a laminar premixed flame structure, cannot propagate against the incoming flow and is ultimately blown off or lifted. On the other hand, the OH^* chemiluminescence imaging suggests that the flame detachment mechanism in the decreasing region is controlled by local flame extinction due to high hydrodynamic strain, which is in line with previous observations underlining the importance of shear-generated vortices in the stability of diffusion jet flames [67]. In the latter case, downstream extinction by strain occurs close to the breakpoint of the turbulent jet before reaching lean flammability conditions in the burner rim wake, hence explaining the annular flame structure observed in Figs. 4.10(a)-(c).

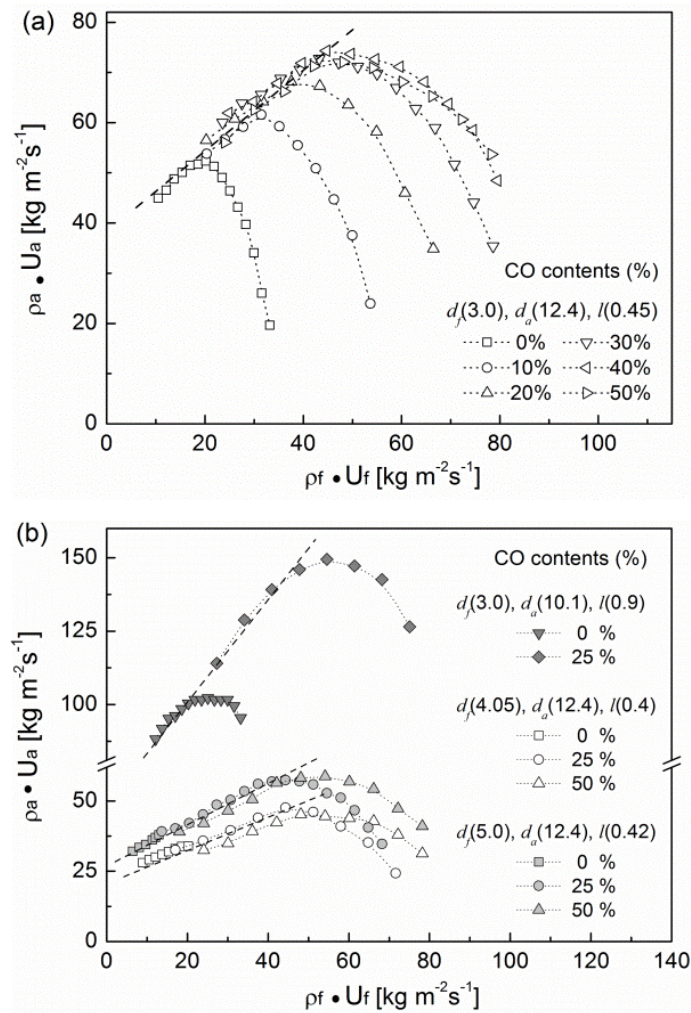


Fig. 4.11 Detachment stability limits of syngas jet flames with coaxial air in terms of air/fuel mass fluxes: (a) datasets of Fig. 4.8, (b) complimentary datasets for additional burner geometries.

It is clear from Fig. 4.10 that the increasing and decreasing branches of the stability curves are governed by different mechanisms, and thus, a successful “global” scaling of the syngas stability limits presented in Fig. 4.8 should not be expected. It shall however be pointed out that a simple scaling of the ascending stability branches exists, and the latter can be interpreted on the basis of the lean flammability concept evocated above. Assuming that the air and fuel influx entrained in the burner rim wake are proportional to the global air and fuel mass fluxes and recognizing that flammability limits of syngas in air are weakly depending on the fuel mixture composition up to 50% carbon monoxide addition (see Wierzba and Kilchyk [68]), the ascending stability limits should roughly collapse into a single line while plotted in the air versus fuel max flux reference. The datasets provided in Fig. 4.8, accordingly re-plotted in Fig. 4.11(a), agree with this assertion. Figure 4.11(b) shows that this result is independent of the burner geometry that is considered (extra cases provided for $d_f = 4.05$ mm and $l = 0.9$ mm). We shall finally emphasize that the non-monotonic variations of the syngas flame stability limits is strongly related to the fuel nozzle thickness l , as discussed earlier for the hydrogen cases in section 4.4.1. As a matter of fact, it is seen in Fig. 4.12(a) that the syngas stability curve extrema originally presented in Fig. 4.8 all collapse together if the fuel nozzle exit velocity is normalized by the critical fuel velocities for the single jet cases ($U_{f,c}$). This shows that the change in the detachment mechanisms is primarily governed by the fuel nozzle thickness, independently of the fuel composition that is considered. This is further illustrated in Fig. 4.12(b) where the extrema scaling is confirmed for a larger fuel nozzle diameter ($d_f = 4.05$ mm) and a larger lip thickness ($l = 0.9$ mm). In the present work, transitions from one stability mechanism to the other are recorded at $U_f/U_{f,c} = 0.49$ and 0.61 for $l = 0.4$ and 0.9 mm respectively.

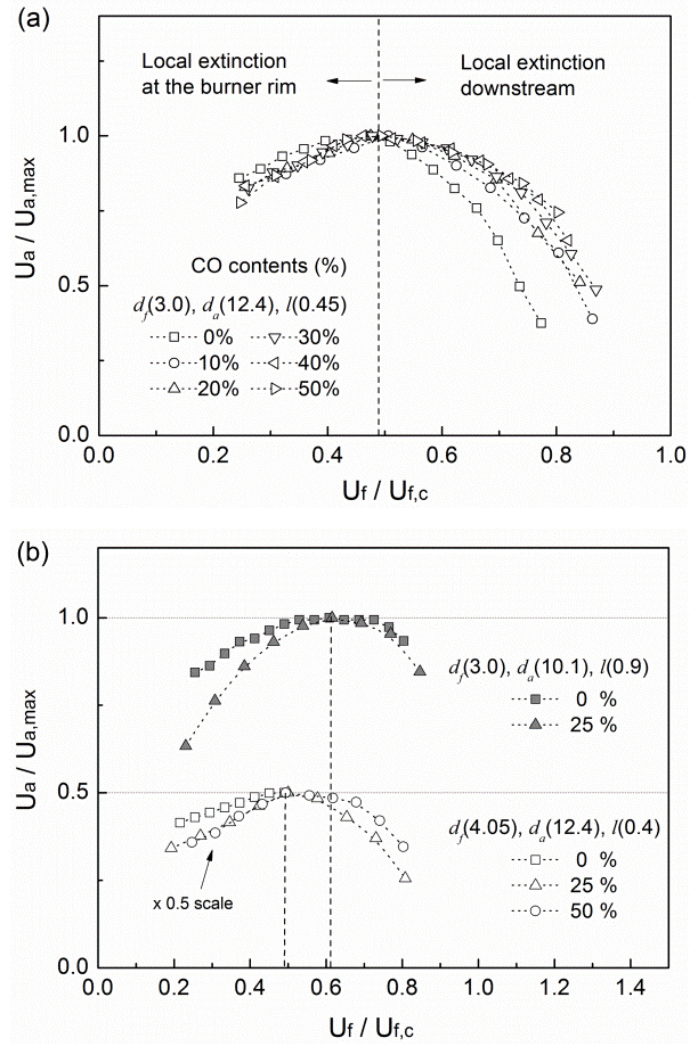


Fig. 4.12 Detachment stability limits of syngas jet flames - coaxial air velocity U_a normalized by the maximum coaxial air velocity $U_{a,max}$ as a function of fuel jet velocity U_f normalized by the critical fuel velocity of the single jet case $U_{f,c}$: (a) Datasets of Fig. 4.8, (b) Additional cases for $d_f = 4.05$ mm (1/2 scaled for enhanced legibility) and $l = 0.9$ mm.

CHAPTER 5

NEAR FIELD STRAIN RATE AND OH LAYER CHARACTERISTICS OF H₂/CO SYNGAS TURBULENT NON-PREMIXED JET FLAMES

5.1 Background and Objectives

Turbulent non-premixed jet flames with coaxial air are widely used in practical combustors due to increased mixing rate and simple configuration. If the coaxial air flow rate increased with fixed fuel flow rate, the detachment (blowoff or liftoff) occurs at a certain air velocity ($U_{a,bo}$). A lifted flame can be sustained by the balancing of premixed flame or edge flame propagations and the flow, if the conditions of turbulent properties, flow and chemical kinetics at a certain point on stoichiometric contour are favorable. Otherwise, the flame is blown off. The detachment of coaxial jet flame with moderate lip thickness appears into two types [17,58]. In relatively low fuel jet velocity region (regime I), the detachment of the flame is governed by local extinction due to lean flammability of the premixed stabilization point on the nozzle lip (see Fig. 5.1(a)). However, in relatively high fuel jet velocity region (regime II), the detachment is controlled by local extinction near the nozzle exit due to high strain or high scalar dissipation (see Fig. 5.1(b)). They are shown as non-monotonic trends (increasing-decreasing) in fuel and air jet velocity domain.

A number of experimental studies on turbulent non-premixed jet flames characterized the structures by planar laser-induced fluorescence (PLIF) of flame radicals such as OH and CH [69,70], in some cases combined with particle image velocimetry (PIV) [71-76], or combined with Rayleigh scattering [77-79] to assess the relationship between the reaction zone and kinematic quantities such as strain rate, vorticity, and dilataion or scalar dissipation rate. Donbar et al. [71] applied PIV/CH-PLIF to methane

diffusion jet flame and found that the flame chemistry and diffusion processes do not respond to the rapidly-varying strain field. Studies using PIV/OH-PLIF in turbulent non-premixed flames [71-74] showed that the principal compressive strain axis was found to align at approximately 45° to the flow direction in lower part of the flame. However, for high Reynolds number, the OH structures do not tend to align orthogonal to the principal compressive strain axis. Hult et al. [75] used high repetition PIV/OH-PLIF and found that individual extinction events could be correlated to local strain fields and vertical flow structures. Studies using Rayleigh scattering with PLIF or Raman scattering revealed the relationship between local extinction and scalar dissipation rate. Kelman and Masri [77] have reported that the scalar dissipation rate did not significantly influence flame extinction while Sutton and Driscoll [78,79] observed that regions of local extinction appear to correspond to an overlap of strong dissipation layers and the stoichiometric contour.

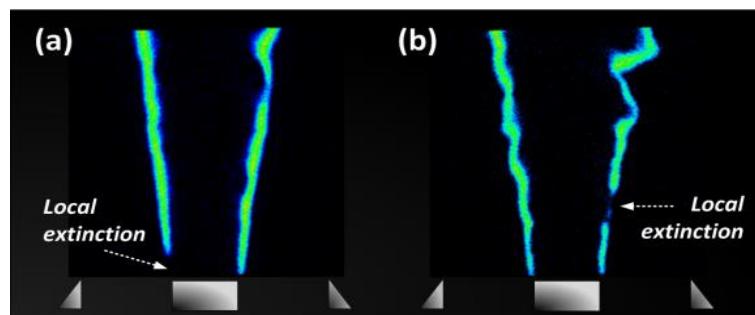


Fig. 5.1 OH PLIF images of the flame near detachment condition in (a) regime I and (b) regime II.

Recently, with increasing concern on integrated gasification combined cycle (IGCC), plenty of research on hydrogen (H_2) and carbon monoxide (CO) syngas combustion has been conducted for fundamental studies (e.g. [5-19]) and for practical gas turbine combustors (e.g. [20-22]). In this study, we investigated on H_2/CO syngas turbulent jet flames. We examined their stability characteristics and particularly focused on the

detachment of the flame in regime II, which is controlled by local extinction with high strain or high scalar dissipation. We measured velocity field and OH distribution with simultaneous PIV and OH PLIF of turbulent syngas non-premixed flames and investigated flow properties, such as velocity and strain rate, and OH layer thickness. Especially, we observed near field region since the detachment is controlled by local extinction appears extremely near field region. Experiments were performed at various points near detachment conditions and stable conditions in regime II. Finally, we focused on examining the effects of strain rate and OH layer thickness on the detachment and their relationship.

5.2 Experimental Methods

5.2.1. Experimental Apparatus and Conditions

Schematics of experimental setups are shown in Fig. 5.2. The cross section of the combustor test section is a square of 200 by 200 mm and the height is 800 mm. The axisymmetric fuel nozzle was located at the bottom center of the combustor and surrounded by the coaxial air shroud (see Fig. 5.3(a)). The fuel nozzle has a 3.0 mm inner diameter (d_f) and a 0.45 mm rim-thickness (l). The coaxial air nozzle has an inner diameter (d_a) of 12.4 mm.

The experimental conditions of syngas coaxial air flames are shown in Table 5.1. Three fuel compositions ($H_2/CO\%$: 100/0, 75/25 and 50/50) were investigated. Both regime I and II near detachment condition were investigated and three different Re_f conditions in regime II near detachment were investigated. And we compared the flame near detachment and the stable flame which have identical Re_f . The fuel jet Reynolds number is defined as $Re_f = U_f d_f / \nu_f$, where U_f is averaged fuel jet exit velocity and ν_f is kinematic viscosity of the fuel. The coaxial air Reynolds number is defined as $Re_a = U_a \{d_a - (d_f + 2l)\} / 2\nu_a$, where U_a is averaged air exit velocity and ν_a is kinematic viscosity of the air.

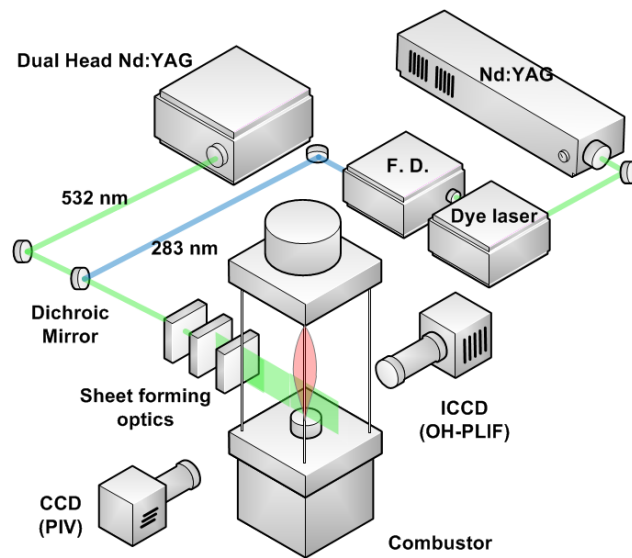


Fig. 5.2 Schematics of the experimental setup for simultaneous PIV and OH PLIF measurements.

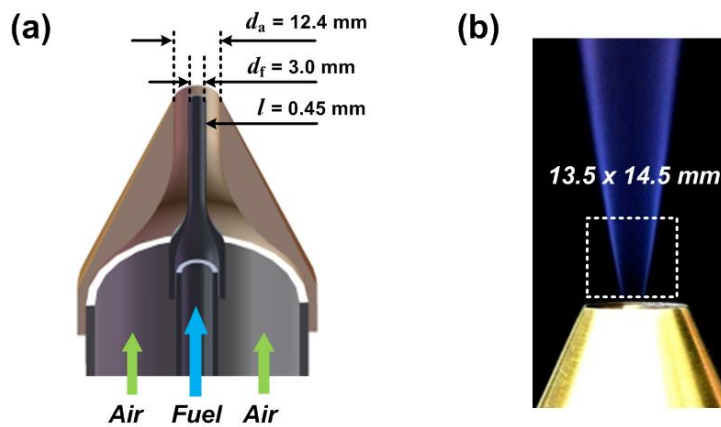


Fig. 5.3 Schematics of the nozzles: (a) the nozzle configurations and dimension, and (b) field of view for PIV and OH PLIF simultaneous measurement.

Table 5.1 Experimental conditions (*ND: near detachment, ST: stable).

Case	H ₂ /CO	Regime	Re _f	U _f (m/s)	Re _a	U _a (m/s)	Z _s	U _s (m/s)	U _a /U _{a,d}	Remarks*
1		I	5200	190	8200	29		33.6	0.95	ND
2		II	7900	290	7800	27.6		35.5	0.95	ND
3	100/0	II	8700	320	6800	24	0.0282	32.4	0.95	ND
4		II	9600	350	5200	18.5		28.4	0.95	ND
5		II	8700	320	4200	15		23.7	0.6	ST
6		I	4400	90	9600	34		40.2	0.95	ND
7		II	6900	140	11500	41		51.9	0.95	ND
8	75/25	II	7800	160	11000	39	0.110	52.3	0.95	ND
9		II	8800	180	9700	34.5		51.0	0.95	ND
10		II	7800	160	5600	20		35.4	0.5	ST
11		I	6800	75	10100	36		43.0	0.95	ND
12		II	9500	105	10700	38		50.0	0.95	ND
13	50/50	II	10800	120	9400	33.5	0.179	49.0	0.95	ND
14		II	12200	135	7000	25		44.7	0.95	ND
15		II	10800	120	5600	20		37.9	0.55	ST

5.2.2. Simultaneous PIV and OH PLIF diagnostics

A schematic diagram of setup for the simultaneous PIV and OH PLIF measurement is shown in Fig. 5.2. For PIV measurements, a seeding particle ZrO_2 , which has a nominal size of $1\ \mu m$, was inserted into fuel and coaxial air stream. The laser sheets were provided by dual head Nd:YAG laser (Continuum, Surelite II PIV) and the scattered signals from seeding particles were recorded by 1600×1200 CCD camera (Viewworks, VH-2MC-M). The laser power is about 100 mJ/pulse and the duration of each pulse is within 10 ns. The time separation between two laser pulses ranges from $0.33\ \mu s$ to $1.5\ \mu s$ according to experimental conditions.

PLIF measurements of the $Q_1(6)$ transition of the $A^2\Sigma^+ - X^2\Pi$ ($v' = 1, v'' = 0$) band of OH radical were made near 282.93 nm. For producing 282.93 nm light, 532 nm light from Nd:YAG laser (Continuum, Surelite I) served as the pump source for a dye laser (Continuum, ND-6000) which was tuned to ~ 565.86 nm and then frequency-doubled. Fluorescence from the A-X(1,0) and (0,0) bands at 306-320 nm was collected with a UV-Nikkor 105 mm $f/4.5$ objective. The image was focused onto the 512×512 ICCD Camera (Princeton Instrument, PI-MAX II). WG-305 and UG-11 filters were used to block scattering signals and the incident light of the flame.

The field of view for PIV and OH PLIF were 13.5×18.0 mm and 14.5×14.5 mm located just above the nozzle exit, respectively. Finally, we obtained joint area of 13.5×14.5 mm when we conducted post-processing. For the PIV system, the interrogation spot size is 48×48 pixels with a 50% overlap, which is equivalent to a vector spatial resolution of 0.27×0.27 mm. The resolution of OH PLIF images is about $28.2\ \mu m$ and thus the spatial resolution of this experiment is limited by the PIV resolution. 120 images of PIV and OH PLIF were taken for each condition.

5.3 Stoichiometric velocity, U_s

Donbar et al. [71] measured CH PLIF and PIV in turbulent non-premixed jet flame and considered the conditional mean axial velocity at the stoichiometric contour. They

noted that the velocity on the flame surface is close to $Z_s U_f$, where Z_s is the stoichiometric mixture fraction and U_f is the bulk nozzle exit velocity. Subsequently, Han and Mungal [72] investigated this concept further with the governing equations of the mixture fraction and the axial velocity:

$$\frac{\partial}{\partial t}(\rho Z) + \frac{\partial}{\partial x_i}(\rho u_i Z) = \frac{\partial}{\partial x_i} \left(\rho D \frac{\partial Z}{\partial x_i} \right) \quad (5.1)$$

$$\frac{\partial}{\partial t}(\rho u_1) + \frac{\partial}{\partial x_i}(\rho u_i u_1) = -\frac{\partial p}{\partial x_1} + \frac{\partial}{\partial x_i} \left(\rho \nu \frac{\partial u_1}{\partial x_i} \right) \quad (5.2)$$

where u_1 indicates the axial direction velocity. Eqs. (5.1) and (5.2) have similar formal structure except for two aspects, which are the pressure gradient term, $\partial p / \partial x_1$, and transport property values, D and ν , where D is the molecular diffusion coefficient and ν is the kinematic viscosity. Thus, if we assume uniform pressure condition ($\partial p / \partial x_1 \approx 0$) and unity Schmidt number ($Sc = \nu / D$) in the combustion field, the former two equations become identical. Furthermore, for the high Reynolds number flows, the relative importance of the molecular diffusion and viscous term reduces. Thus, the non-unity Schmidt number would not affect the similarity significantly. Also, the density change by heat release affects both equations in the same manner. Therefore, the similarity between two equations remains valid even in the heat released environment.

The boundary conditions are also critical. For the boundary conditions at the nozzle exit line, the mixture fraction has a top-hat profile, while the axial velocity has a turbulent pipe flow profile. Moreover, the mixture fraction will be zero at the ambient flow, while the axial velocity will be a certain value consistent with the coflow air velocity. It is expected that the difference in the nozzle exit profile between mixture fraction and axial velocity will become insignificant far downstream because the jet can be assumed as a point source, where only the momentum flux is a significant factor. However, the coflow air carries momentum throughout the flow, thus the coflow air momentum will remain

important in determining the velocity on the flame surface.

From the discussions, the axial velocity of the stoichiometric mixture can be derived. In Fig. 5.4, a conceptual schematic of the ideal molecular mixing process in a uniform pressure environment is shown. If Z_s kg of fuel traveling at speed U_f mixes with $(1 - Z_s)$ kg of air traveling at U_a , the mixture velocity, U_s , can be computed from the momentum conservation as:

$$U_s = Z_s U_f + (1 - Z_s) U_a \quad (5.3)$$

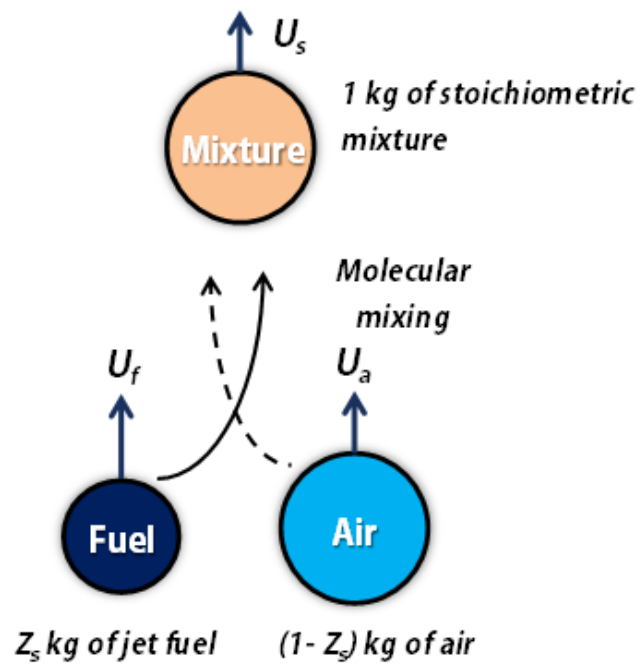


Fig. 5.4 Conceptual schematic of the ideal mixing process in a uniform pressure condition. The mixture velocity is the stoichiometric axial velocity, $U_s = Z_s U_f + (1 - Z_s) U_a$. (ref. [72])

For a non-uniform nozzle exit velocity profile such as in this case, the most appropriate value for the fuel jet velocity will be the momentum-averaged velocity, $U_f = J_0/m_0$, where J_0 and m_0 are the initial momentum and mass fluxes of the jet from the nozzle, respectively. For a top-hat velocity profile, momentum averaged velocity should be the same as the bulk velocity, U_b , which is defined as the volume flowrate divided by the exit area. However, for a flow from a tube, the two values are different. According to the analysis from Han and Mungal [72], the U_f/U_b ratio is almost unity in a turbulent pipe flow with high Reynolds number. Moreover, another aspect of Eq. (5.3) can be revealed if it is rearranged as:

$$U_s - U_a = Z_s(U_f - U_a) \quad (5.4)$$

This represents the velocity on the stoichiometric surface in a reference frame moving with constant velocity of U_a with assumptions of top-hat profile, unity Schmidt number, and uniform pressure distribution according to Eqs. (5.1) and (5.2).

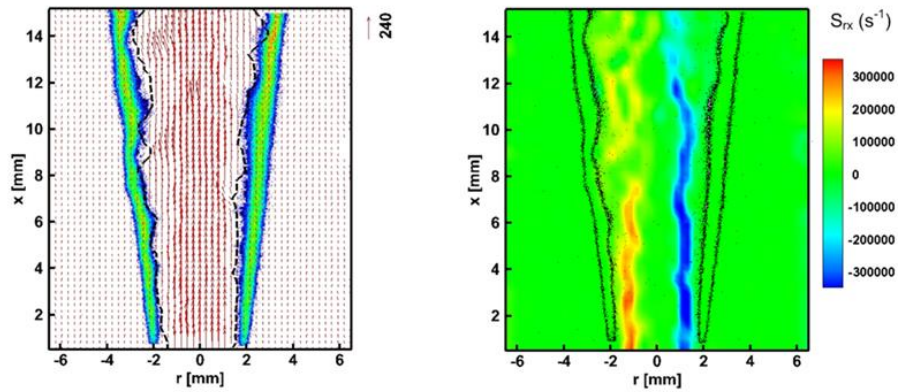
Considering the various assumptions involved in the concept of stoichiometric axial velocity, the validity of U_s to represent a characteristic axial velocity on the flame surface has to be assessed.

5.4 Instantaneous Velocity and Strain Rate Fields with OH Layers

Figures 5.5-5.7 show pairs of instantaneous velocity and shear strain rate field superimposed by the OH layer. These were taken at near field which is the range of $0.25 \leq x/d_f \leq 5.0$. Shear strain rate can be calculated from $S_{rx} = 1/2(\partial U_r/\partial x + \partial U_x/\partial r)$, where U_r is r -direction component of velocity and U_x is x -direction component of velocity. Upper pairs show the images in regime I and lower pairs show the images in regime II and all images were taken near detachment condition ($U_a/U_{a,bo} \approx 0.95$). In left image of each pair, dashed line represent the stoichiometric velocity U_s .

H₂/CO : 100/0

(a) Case 1: $Re_f = 5190$, $Re_a = 8160$



(b) Case 3: $Re_f = 8740$, $Re_a = 6750$

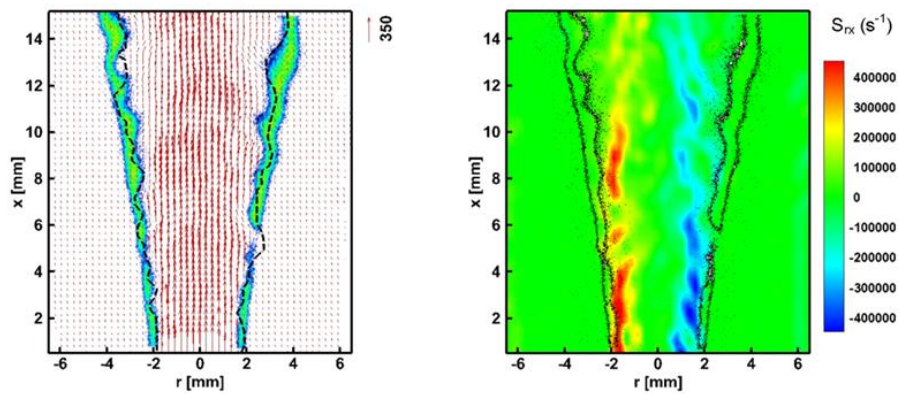
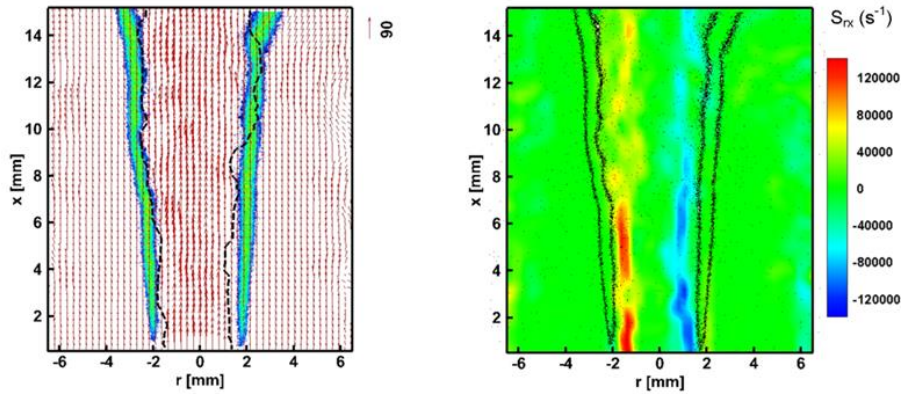


Fig. 5.5 Instantaneous velocity fields and strain rate fields superimposed by the OH layer near detachment conditions for H₂/CO 100/0: (a) for Regime I and (b) for Regime II. The dashed line represents the stoichiometric velocity U_s .

H₂/CO : 75/25

(a) Case 6: $Re_f = 4410$, $Re_a = 9560$



(b) Case 8: $Re_f = 7840$, $Re_a = 11000$

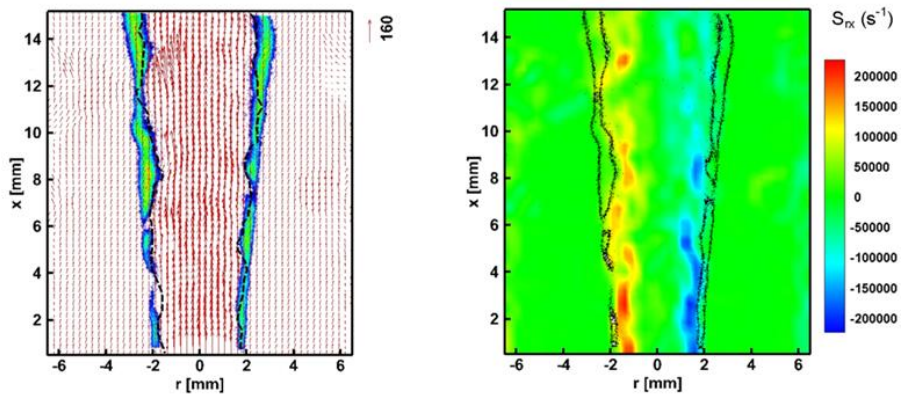
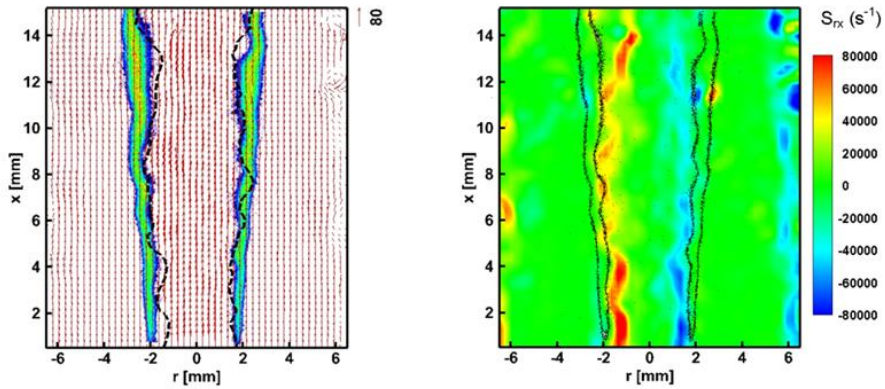


Fig. 5.6 Instantaneous velocity fields and strain rate fields superimposed by the OH layer near detachment conditions for H₂/CO 75/25: (a) for Regime I and (b) for Regime II. The dashed line represents the stoichiometric velocity U_s .

H₂/CO : 50/50

(a) Case 11: $Re_f = 6770, Re_a = 10100$



(b) Case 13: $Re_f = 10800, Re_a = 9420$

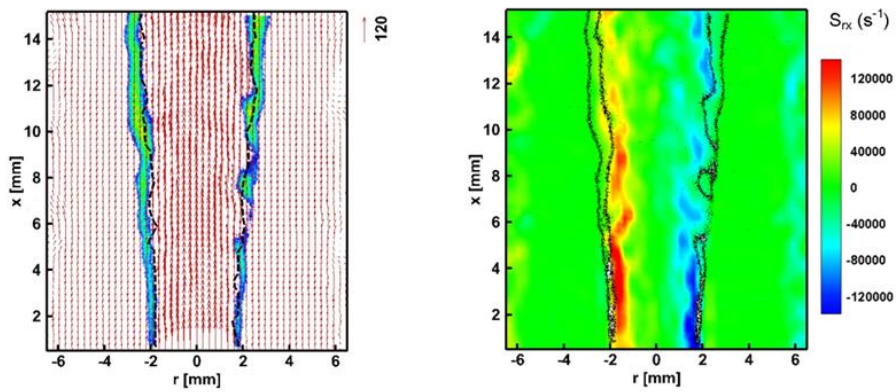


Fig. 5.7 Instantaneous velocity fields and strain rate fields superimposed by the OH layer near detachment conditions for H₂/CO 50/50: (a) for Regime I and (b) for Regime II. The dashed line represents the stoichiometric velocity U_s .

In Figs. 5.5-5.7, the dashed line represents the contour of U_s described in Eq. (5.3). Interestingly, the correspondence between the location of U_s and the inner edge of the OH layer is extremely good for all cases. In many laminar counterflow flame calculations (e.g. [70,72]), it is revealed that OH peak is located in relatively lean regions, thus Z_s contour is located fuel side of OH layer. Consequently, the inner edge of OH layer which is close to Z_s contour has good correspondence with U_s even at near field.

In regime I shown in Figs. 5.5(a)-5.7(a), OH layers are located closer to fuel side due to higher air-fuel velocity ratio than in regime since higher air momentum leads the Z_s to be located inside. However, shear strain rate on OH layer is relatively low since the velocity difference between fuel and air is smaller. Also, thickness of OH layer in this regime is significantly larger than in regime II.

In regime II shown in Figs. 5.5(a)-5.7(a), OH layer is located near high shear strain region which is similar to the results of other studies [72,73,76]. Particularly, inner edge of OH layer is well matched with high strain rate location. It is interpreted that high strain rate on the flame surface entrains air into fuel stream and enhance combustion or chemical reaction, unless the flame surface is extinguished by excessive strain rates [72]. Furthermore, local extinctions with high strain rates are shown in regime II. Especially, left lower side of the OH layer in Fig. 5.6(b) and right side of the OH layer of Fig. 5.7(b) show local extinctions with relatively high strain rates.

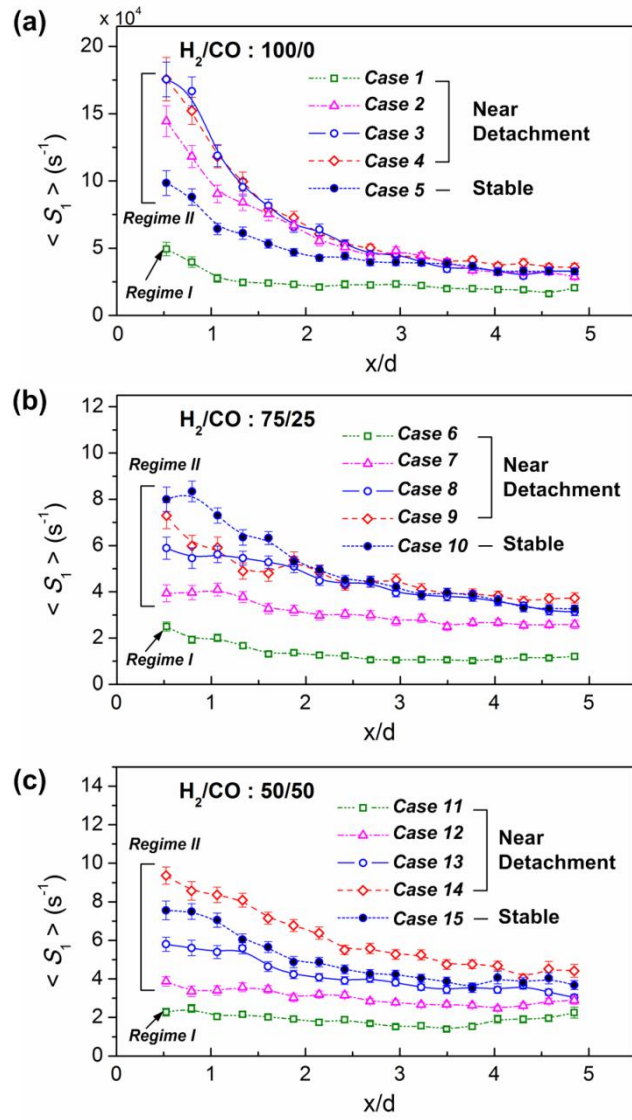


Fig. 5.8 Mean extensive principal strain rates, $\langle S_1 \rangle$, conditioned upon OH layer with x-axis: (a) H_2/CO 100/0, (b) 75/25/, and (c) 50/50.

5.5 Mean Strain Rates on OH Layer

The flamefront strain rate can play a key role in determining scalar dissipation rate χ which is the major parameter that governs the local chemical reaction. The mean measured extensive (maximum) principal strain rates, $\langle S_1 \rangle$, on OH layers along x direction are shown in Fig. 5.8 for all experimental conditions. S_1 was extracted at the radial point which has maximum OH intensity for each axial position. $\langle S_1 \rangle$ was calculated from averaging S_1 from 120 instantaneous images. Error bars shown here indicate the standard deviation of the mean, defined as the standard deviation divided by the square root of the number of samples, $\sigma/N^{1/2}$. It is observed that strain rates on OH layer are highest near nozzle exit and decrease with axial distances for all flames, which is consistent with the observation in other studies [72,76].

The mean strain rates of flames near detachment ($U_a/U_{a,bo} \approx 0.95$) in regime I (squares in Fig. 5.8) are significantly lower than other flames. This is consistent with instantaneous images in Figs. 5.5-5.7. Thus, this can be an evidence that the detachment in regime I is not governed by high strain rates on the flame.

For three flames near detachment of 100% H_2 flames in regime II, the maximum values $\langle S_1 \rangle$ near nozzle exit are almost identical ($\langle S_1 \rangle \approx 160000 \text{ s}^{-1}$) and decreasing trends of $\langle S_1 \rangle$ with the axial distance are similar. Although flames have different Re_t , the detachment occurs at the similar $\langle S_1 \rangle$. However, for 75/25 % and 50/50% H_2/CO flames, the maximum values of $\langle S_1 \rangle$ present significant differences. This implies that the detachment of the flames can appear with different strain rates for different fuel jet Reynolds numbers although the flames are in regime II. Further, we compared the flames near detachment (unfilled circles) and stable condition (filled circles). In 100% H_2 flames, the maximum $\langle S_1 \rangle$ value of the flame near detachment is about twice that of the stable flame since the higher airflow momentum leads the stoichiometric mixture fraction (Z_s) line to be inner side where the strain rate is higher. However, for 75/25% H_2/CO case, the stable flame has approximately 1.3 times larger maximum $\langle S_1 \rangle$ value than the flame near detachment. When the air velocity increases with fixed fuel velocity, Z_s line shifts toward

inner location where higher strain exists and the velocity gradient decreases. In this case, a decreasing of strain rate by reduced velocity gradient is larger than an increasing of strain rate by Z_s line shift. This observation also appears in 50/50% H_2/CO case. It is presumably due to higher density and smaller jet velocity of high CO content fuels which lead Z_s line shift and reduction of velocity gradient to be smaller and larger, respectively, when air velocity is increased. From these observations, it can be inferred that the detachment of the flame in regime II is not directly governed by high strain rate on the flame.

5.6 OH Layer Thickness

Another parameter which governs the local extinction is known as scalar dissipation rate χ . It characterizes the scalar gradients within the flowfield and is defined as

$$\chi = 2 D (\nabla \xi)^2 \quad (5.5)$$

where D is the molecular diffusivity and ξ is the mixture fraction. For large values of χ , an imbalance in the heat production and the heat diffusing away from the reaction could cause flame extinction [80]. The thickness of the CH layer in a laminar counterflow flame is given by asymptotic analysis [81] and numerical results [70]:

$$\delta_{CH} = 0.3 (D_0/\chi)^{1/2} \quad (5.6)$$

where D_0 is characteristic diffusivity. Thus, scalar dissipation governs the reaction zone thickness. Although OH radical may not be a proper indicator of flame surface because of slow removal due to three-body recombination reactions, there is no alternative way but OH in H_2 flames in this study. Thus, we assumed that the flame thickness is proportional to the OH thickness, then, Eq. (5.6) can be

$$\delta_{OH} \sim \chi^{-1/2} \quad (5.7)$$

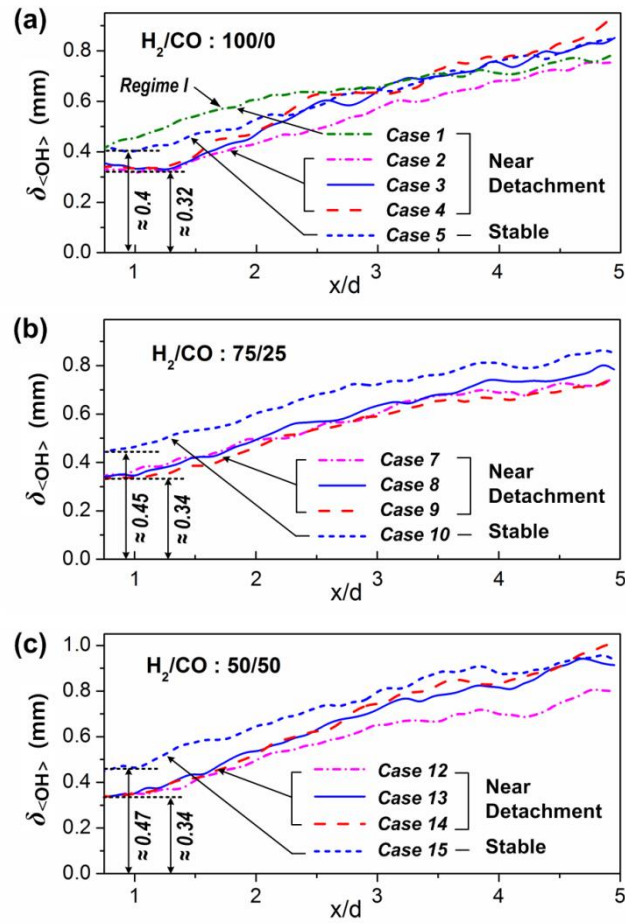


Fig. 5.9 Mean OH layer thickness ($\delta_{\langle \text{OH} \rangle}$) extracted from averaged OH PLIF images along axial direction: (a) H_2/CO : 100/0, (b) 75/25, and (c) 50/50. 120 instantaneous images were averaged for each case. Star indicates the minimum $\delta_{\langle \text{OH} \rangle}$ of each case.

Mean OH layer thickness ($\delta_{\langle\text{OH}\rangle}$) with axial direction are shown for all cases in Fig. 5.9. Averaged images from 120 instantaneous images of each case were used to extract thicknesses. Star symbols on y-axis show the minimum $\delta_{\langle\text{OH}\rangle}$ of each case. All flames have minimum $\delta_{\langle\text{OH}\rangle}$ near the nozzle and increase in axial direction because the radial profile of the mixture fraction evolves from a top-hat near nozzle exit to a smoother Gaussian-like function downstream. $\delta_{\langle\text{OH}\rangle}$ of the flame near detachment in regime I shown in Fig. 5.9(a) is significantly larger than other flames in regime II. From the relationship given in Eq. (5.7), it can be concluded that the detachment in regime I is not governed by high dissipation rate. Interestingly, in regime II, it is observed that the minimum values of $\delta_{\langle\text{OH}\rangle}$, located vicinity of nozzle exit, of the flames near detachment in are the almost identical, while those of the stable flames are approximately 1.2~1.4 times larger. Thus, it can be inferred that the detachment in regime II is highly dependent to χ near the nozzle exit where high strain rates on OH layer exist.

5.7 Relationship between Strain Rate and OH Layer Thickness

A scattered plot of the OH layer thickness (δ_{OH}) conditioned on the S_1 is shown in Fig. 5.10. Also the mean value of the δ_{OH} is shown (solid line). From the assumption that the dissipation rate is proportional to the local strain rate [82] and Eq. (5.7), the relation, $\delta_{\text{OH}} \sim 1/S_1^{1/2}$, can be deduced and it is also shown in the image (dotted line). δ_{OH} values are widely distributed in relatively low S_1 region and the distribution narrows and converges into low δ_{OH} value as S_1 increases. The mean value ($\overline{\delta_{\text{OH}}}$) decreases with S_1 , which is in agreement with the inverse relationship. However, the scaling does not agree with the mean profile since the relations are results from laminar counterflow flames. Nonetheless, the upper side of scattered points has good correspondence with the scaling. Donbar and Driscoll [71] showed that the reaction zone thickness does not respond to the high-frequency oscillating strain component. Broadly scattered distribution of δ_{OH} in low S_1 region is presumably due to high-frequency intermittent strain rates by relatively larger scale eddies shown in downstream of images. However, near the nozzle exit, very small

scale eddies exist and do not produce intermittence as large as reaction zone scale. Thus, only high strain by bulk velocity gradients and thin reaction zone by high scalar gradients are presented which result in converged distribution of δ_{OH} in high S_1 region.

Figure 5.11 shows the probability density function (pdf) of δ_{OH} for the flames near detachment and the stable flames. Also for each condition, pdfs for two ranges of extensive strain rate S_1 , high S_1 and low S_1 , are shown. The critical S_1 values (70000 s^{-1} for 100/0 and 50000 s^{-1} for 75/25 and 50/50 $\text{H}_2/\text{CO}\%$) are determined by approximate value of average. The pdfs of δ_{OH} are broadly distributed for the range of low S_1 values, while the distribution shifts such that the most probable value of δ_{OH} is near the minimum mean OH layer thickness $\delta_{<OH>}$ for the range of high S_1 value. In other word, OH layer thickness tends to distribute on wide range of S_1 value when relatively small S_1 is exerted, however, most OH layer tends to be thin when S_1 on flame increases, which is consistent with shown in Fig. 5.10. The most probable value of δ_{OH} for high S_1 shifts toward smaller value when the flame condition changes from stable to near detachment. This change of the pdf shows that increasing probability of existence of relatively thin OH layer which undergoes high strain rate leads the stable flames to be detached from the nozzle.

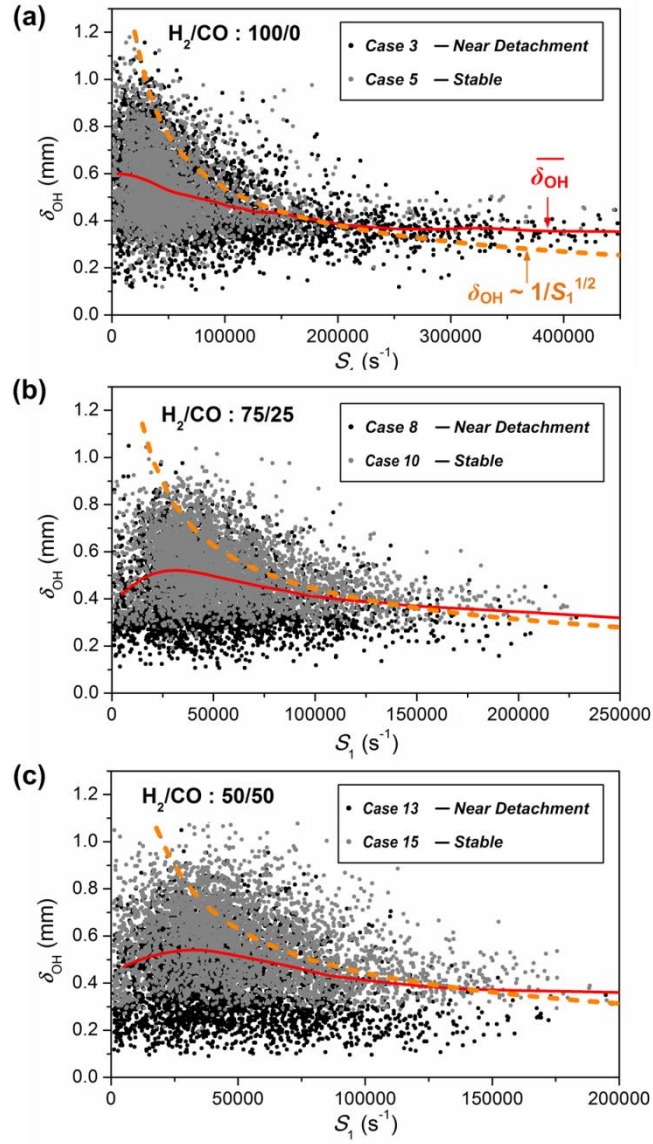


Fig. 5.10 Scatterplots of OH layer thickness (δ_{OH}) conditioned on extensive principal strain rate (S_1) for (a) 100/0, (b) 75/25 and (c) 50/50 H_2/CO flame. Black points are for near detachment condition ($U_a/U_{a,bo} \approx 0.95$) and gray points are for stable conditions ($U_a/U_{a,bo} \approx 0.6$). Solid line shows mean value, $\overline{\delta_{OH}}$.

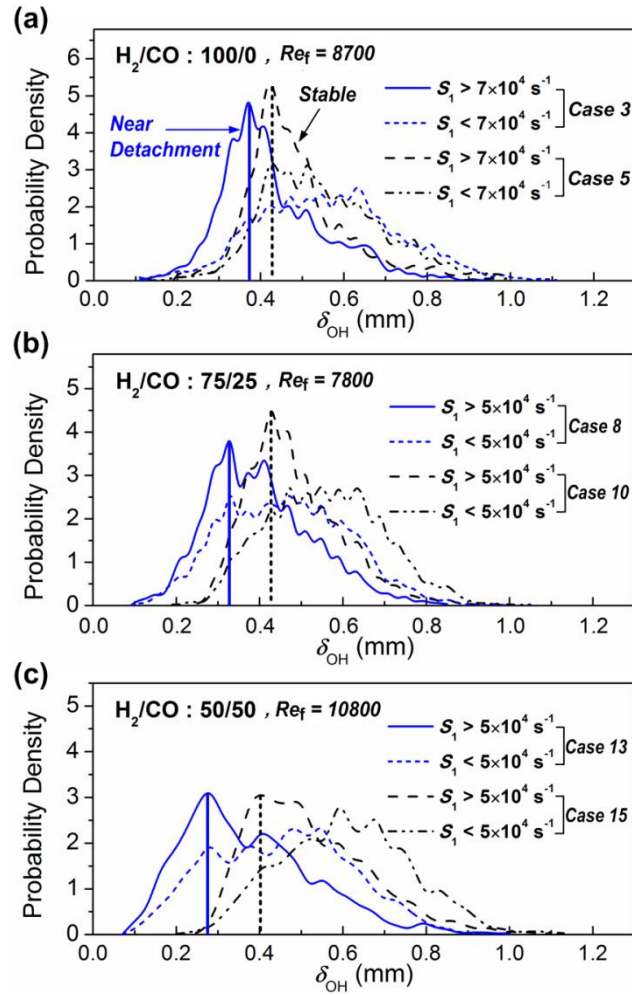


Fig. 5.11 Probability density function (pdf) of OH layer thickness (δ_{OH}) conditioned upon high S_1 and low S_1 at near detachment condition and stable condition.

CHAPTER 6

CONCLUSION

The experimental studies were performed on the NO_x scaling and stability characteristics of H₂/CO syngas turbulent non-premixed jet flames. NO_x emission characteristics and EINO_x scaling of H₂ and H₂/CO syngas jet flames were investigated. Previous NO_x scaling was assessed for measured flame length and NO_x concentration. Modified scaling of EINO_x was suggested and assessed for H₂/CO syngas jet flames. Stability characteristics of H₂/CO syngas simple and coaxial jet flames were investigated. Stability of single fuel jet flame with varying fuel composition was studied and effects of coaxial air nozzle diameter and fuel nozzle lip thickness were studied. Also, stability limits on fuel jet velocity and air jet velocity diagram was studied and near field flame behavior near detachment condition was observed. Strain rates on flame surface and OH layer thickness were investigated using simultaneous PIV and OH PLIF measurements. Particularly, extreme near field region was observed where local extinctions due to high strains and high scalar dissipations lead the flame blowoff or liftoff. Relationship between strain rate on OH layer and OH layer thickness was examined and probability density function of OH layer was compared for the flames in stable and near detachment. The conclusions drawn from the experimental results are as follows.

EINO_x scaling of H₂ and H₂/CO syngas jet flames were examined by measuring flame length and NO_x concentrations. The flame lengths of the syngas jet increase with Re_f . The characteristic flame length is also increased according to the characteristic Froude number. It is confirmed that the trends are identical with Delichatsios's empirical correlation and the jet flames are in the region of buoyancy-momentum transition. The NO_x emission decreases with increasing Re_f since the decreasing effect on the flame residence time by the increased fuel jet velocity is more significant than the increasing effects by lengthened flame. As the CO content increases in syngas fuel, the NO_x emission decreases since the flame length decreases according to the CO content. The

previous EINO_x scaling, which is based on flame residence time, $L^3/(d_f^{*2}U_f)$, is not appropriate for the present hydrogen jet results because the flame is not in the momentum-dominated region. The flame residence time cannot be valid in the buoyancy-momentum transition region because of the lack of jet similarity. The simplified flame residence time, L/U_f , is therefore considered, and the modified scaling, $EINO_x/(L/U_f) \sim (U_f/d_f^*)^{1/2}$, fits both the present results and Chen and Driscoll's results. The modified scaling also fits the results for the H₂/CO syngas jet flames. The modified scaling cannot collapse the data of all syngas fuel compositions into a single line because of the definition of EINO_x. The air mass amount participating in the reaction is considered as a reference instead of fuel mass amount. The modified scaling, $EINO_x/f_{st}/(L/U_f) \sim (U_f/d_f^*)^{1/2}$, collapses all datasets into a single line. However, the scaling is suitable only for H₂/CO syngas since the flame temperatures are almost the same in all compositions.

The detachment stability characteristics of attached H₂ and syngas jet flames with coaxial air were investigated by observing flame behaviors with varying fuel jet and air jet velocities. The critical fuel jet velocity of the single jet flame of syngas decreases with increase of CO content in syngas fuel. The importance of the maximum burning velocity (flame/flow balance concept) and stoichiometric mass ratio of air to fuel (which affects the flame base location) is underlined. Hydrogen jet flame cases show that the stability limits are almost independent of the coaxial nozzle size in the fuel/air stream velocity domain. On the other hand, blowout of the lifted hydrogen flames is clearly related to the jet turbulent characteristics. The fuel nozzle rim thickness strongly affects the detachment stability trends for jet flames with coaxial air. Non-monotonic (ascending/descending) trends were observed for all syngas compositions in the fuel/coaxial air velocity domain. Chemiluminescence imaging suggests that the ascending trends are governed by the lean flammability limit of the fuel/air mixture in the burner rim wake while descending trends are attributed to the local flame extinction downstream of the nozzle exit. A fuel/air mass flux scaling, demonstrated for the ascending stability branches, supports the concept of lean extinction in the burner rim wake. For the syngas compositions herein investigated, the stability curve extrema are found to be identical when the fuel nozzle velocity is

normalized by the single jet critical velocity, thus underlining the importance of the fuel nozzle lip thickness in the flame stability behavior.

For understanding the detachment phenomenon in descending region (Regime II) of a turbulent non-premixed jet flame, strain rate and OH layer characteristics were studied experimentally with simultaneous PIV and OH PLIF measurements. The mean principal strain rate S_1 on OH layer decrease with the axial distance and the maximum values of them are located near the nozzle exit. In some cases, the maximum S_1 on OH layer near nozzle exit appears higher in the stable flames than in the flames near detachment. For various fuel jet Reynolds number, the flames near detachment condition have almost identical minimum mean OH layer thicknesses $\delta_{<OH>}$ near the nozzle exit. The S_1 on OH layer and the OH thickness δ_{OH} present inverse relationships, however, δ_{OH} is broadly scattered within a small S_1 range. The pdfs of δ_{OH} show that the distribution is skewed toward lower values within a higher S_1 range while broad distribution around higher values appears within a lower S_1 range. Moreover, the most probable value of δ_{OH} shifts toward lower value near the minimum mean $\delta_{<OH>}$ as the flame condition is varied from stable to near detachment.

REFERENCES

- [1] Climate Change 2007: Synthesis Report. The Intergovernmental Panel on Climate Change, Valencia, Spain, 2007.
- [2] How the energy sector can deliver on a climate agreement in Copenhagen. *Special early excerpt of the World Energy Outlook 2009 for the Bangkok UNFCCC meeting*. The International Energy Agency, 2009.
- [3] Richards, G.A., Mcmillian, M.M., Gemmen, R.S., Rogers, W.A., and Cully, S.R. (2001) Issues for low-emission, fuel-flexible power systems. *Progress in Energy and Combustion Science*, 27, 141-169.
- [4] Stiegel, G.J. (1999) Integrated Gasification Combined Cycle. U.S. Department of Energy - Office of Fossil Energy, Federal Energy Technology Center.
- [5] Chaos, M. and Dryer, F.L. (2008) Syngas combustion kinetics and applications. *Combustion Science and Technology*, 180(6), 1053-1096.
- [6] Davis, S.G., Joshi, A.V., Wang, H., and Egolfopoulos, F. (2005) An optimized kinetic model of H₂/CO combustion. *Proceedings of Combustion Institute*, 30(1), 1283-1292.
- [7] Saxena, P., and Williams, F.A. (2006) Testing a small detailed chemical-kinetic mechanism for the combustion of hydrogen and carbon monoxide. *Combustion and Flame*, 145(1-2), 316-323.
- [8] Bouvet, N., Chauveau, C., Gökalp, I., and Halter, F. (2011) Experimental studies of the fundamental flame speeds of syngas (H₂/CO)/air mixtures. *Proceedings of Combustion Institute*, 33(1), 913-920.
- [9] Das, A.K., Kumar, K., and Sung, C.-J. (2011) Laminar flame speeds of moist syngas mixtures. *Combustion and Flame*, 158(2), 345-353.
- [10] Natarajan, J., Lieuwen, T., and Seitzman, J. (2007) Laminar flame speeds of H₂/CO mixtures: Effect of CO₂ dilution, preheat temperature, and pressure. *Combustion and Flame*, 151(1-2), 104-119.
- [11] Daniele, S., Jansohn, P., Mantzaras, J., and Boulouchos, K. (2011) Turbulent flame

- speed for syngas at gas turbine relevant conditions. *Proceedings of Combustion Institute*, 33(2), 2937-2944.
- [12] Venkateswaran, P., Marshall, A., Shin, D.H., Noble, D., Seitzman, J., and Lieuwen, T. (2011) Measurements and analysis of turbulent consumption speeds of H₂/CO mixtures. *Combustion and Flame*, 158(8), 1602-1614.
- [13] Dryer, F.L., and Chaos, M. (2008) Ignition of syngas/air and hydrogen/air mixtures at low temperatures and high pressures: Experimental data interpretation and kinetic modeling implications. *Combustion and Flame*, 152(1-2), 293-299.
- [14] Petersen, E.L., Kalitan, D.M., Barrett, A.B., Reehal, S.C., Mertens, J.D., Beerer, D.J., Hack, R.L., and McDonell, V.G. (2007) New syngas/air ignition data at lower temperature and elevated pressure and comparison to current kinetics models. *Combustion and Flame*, 149(1-2), 244-247.
- [15] Walton, S.M., He, X., Zigler, B.T., and Wooldridge, M.S. (2007) An experimental investigation of the ignition properties of hydrogen and carbon monoxide mixtures for syngas turbine applications. *Proceedings of Combustion Institute*, 31(2), 3147-3154.
- [16] Lee, J., Park, S., and Kim, Y. (2012) Effects of fuel-side nitrogen dilution on structure and NO_x formation of turbulent syngas non-premixed jet flames. *Energy and Fuels*, 26, 3304-3315.
- [17] Hwang, J., Bouvet, N., Sohn, K., and Yoon, Y. (2013) Stability characteristics of non-premixed turbulent jet flames of hydrogen and syngas blends with coaxial air. *International Journal of Hydrogen Energy*, 38, 5139-5149.
- [18] Giles, D.E., Som, S., and Aggarwal, S.K. (2006) NO_x emission characteristics of counterflow syngas diffusion flames with airstream dilution. *Fuel*, 85, 1729-1742.
- [19] Hwang, J., Sohn, K., Bouvet, N., and Yoon, Y. (2013) NO_x scaling of syngas H₂/CO turbulent non-premixed jet flames. *Combustion Science and Technology*, 185, 1715-1734.
- [20] Daniele, S., Jansohn, P., and Boulouchos, K. (2008) Lean premixed combustion of undiluted syngas at gas turbine relevant conditions: NO_x emissions and lean

- operational limits. *ASME paper*, GT2008-50265.
- [21] Lee, M.C., Seo, S.B., Yoon, J., Kim, M., and Yoon, Y. (2012) Experimental study on the effect of N₂, CO₂, and steam dilution on the combustion performance of H₂ and CO synthetic gas in an industrial gas turbine. *Fuel*, 102, 431-438.
- [22] Nakata, T., Sato, M., Ninomiya, T., and Hasegawa, T. (1996) A study on low NO_x combustion in LBG-fueled 1500°C-class gas turbine. *Journal of Engineering for Gas Turbines and Power*, 118, 534-540.
- [23] Kim, M. (2007) Local flow properties and flame-vortex interactions in turbulent hydrogen nonpremixed flames with coaxial air. *Ph.D Thesis*, Seoul National University.
- [24] O.J. Hinze, *Turbulence*, McGraw-Hill, New York, 1975.
- [25] Cheng, T.S., Chao, Y.-C., Wu, D.-C., Yuan, T., Lu, C.-C., Cheng, C.-K., and Chang, J.-M. (1998) Effects of fuel-air mixing on flame structures and NO_x emissions in swirling methane jet flames. *Proceedings of Combustion Institute*, 27, 1229-1237.
- [26] Cohen, M.J., Ritchie, N.J.B. (1962) Low speed three-dimensional contraction design. *Journal of the Royal Aeronautical Society*, 66, 231-236.
- [27] Becker, H.A., and Liang, D. (1982) Total emission of soot and thermal radiation by free turbulent diffusion flames. *Combustion and Flame*, 44, 305-318.
- [28] Drake, M.C., Correa, S.M., Pitz, R.W., Shyy, W., and Fenimore, C.P. (1987) Superequilibrium and thermal nitric oxide formation in turbulent diffusion flames. *Combustion and Flame*, 69, 347-365.
- [29] Chen, R.-H., and Driscoll, J.F. (1990) Nitric oxide levels of jet diffusion flames: Effects of coaxial air and other mixing parameters. *Proceedings of Combustion Institute*, 23(1), 281-288.
- [30] Seitzman, J.M., Ungut, A., Paul, P.H., and Hanson, R.K. (1990) Imaging and characterization of OH structures in a turbulent nonpremixed flame, *Proceedings of Combustion Institute*, 23, 637-644.
- [31] S. R. Turns, *An Introduction to Combustion*, McGraw-Hill, 1996.
- [32] Ahn, K., Kim, J.H., and Yoon, Y. (2003) Application of PIV to Over-expanded

- Supersonic Flows: Possibilities and Limits. *Journal of Visualization*, 6(4), 353-361.
- [33] Peters, N., and Donnerhack, S. (1981) Structure and similarity of nitric oxide production in turbulent diffusion flames. *Proceedings of Combustion Institute*, 18(1), 33-42.
- [34] Rørtveit, G.J., Hustad, J.E., Li, S.-C., and Williams, F.A. (2002) Effect of diluents on NO_x formation in hydrogen counterflow flames. *Combustion and Flame*, 130, 48-61.
- [35] Chen, J.-Y., and Kollmann, W. (1992) PDF modeling and analysis of thermal NO formation in turbulent nonpremixed hydrogen-air jet flames. *Combustion and Flame*, 88(3-4), 397-412.
- [36] Driscoll, J.F., Chen, R.-H., and Yoon, Y. (1992) Nitric oxide levels of turbulent jet diffusion flames: Effects of residence time and Damkohler number. *Combustion and Flame*, 88(1), 37-49.
- [37] Gabriel, R., Navedo, J.E., and Chen, R.-H. (2000) Effects of fuel Lewis number on nitric oxide emission of diluted H₂ turbulent jet diffusion flames. *Combustion and Flame*, 121, 525-534.
- [38] Kim, S.-H., Yoon, Y., and Jeung, I.-S. (2000) Nitrogen oxides emissions in turbulent hydrogen jet non-premixed flames: Effects of coaxial air and flame radiation. *Proceedings of Combustion Institute*, 28(1), 463-471.
- [39] Lavoie, G.A., and Schlader, A.F. (1973) A scaling study of NO formation in turbulent diffusion flames of hydrogen burning in air. *Combustion Science and Technology*, 8(5), 215-224.
- [40] Oh, J., Hwang, J., and Yoon, Y. (2010) EINO_x scaling in a non-premixed turbulent hydrogen jet with swirled coaxial air. *International Journal of Hydrogen Energy*, 35(16), 8715-8722.
- [41] Sanders, J.P.H., Chen, J.-Y., and Gökalp, I. (1997) Flamelet-based modeling of NO formation in turbulent hydrogen jet diffusion flames. *Combustion and Flame*, 111, 1-15.
- [42] Thring, M.W., and Newby, M.P. (1953) Combustion length of enclosed turbulent

- jet flames. *Proceedings of Combustion Institute*, 4, 789-796.
- [43] Gaydon, A.G. (1942) Flame spectra in the photographic infra-red. *Proceedings of the Royal Society of London, Ser. A*, 181, 197-209.
- [44] Shefer, R.W., Kulatilaka, W.D., Patterson, B.D., and Settersten, T.B. (2009) Visible emission of hydrogen flames. *Combustion and Flame*, 156, 1234-1241.
- [45] Hottel, H.C., and Hawthorne, W.R. (1953) Diffusion in laminar flame jets. *Third Symposium on Combustion, Flame and Explosion Phenomena*, Williams and Wilkins, Baltimore, pp. 254-266.
- [46] Delichatsios, M.A. (1993) Transition from momentum to buoyancy-controlled turbulent jet diffusion flames and flame height relationships. *Combustion and Flame*, 92(4), 349-364.
- [47] Kalghatgi, G.T. (1983) Personal communication – Flame height raw data. *The 9th International Colloquium on Gas Dynamics of Explosion and Reactive Systems*, Poitiers, France
- [48] Kim, S.-H., Kim, M., Yoon, Y., and Jeung, I.-S. (2002) The effect of flame radiation on the scaling of nitrogen oxide emissions in turbulent hydrogen non-premixed flames. *Proceedings of Combustion Institute*, 29, 1951-1956.
- [49] Becker, H.A., and Liang, D. (1978) Visible length of vertical free turbulent diffusion flames. *Combustion and Flame*, 32, 115-137.
- [50] Kalghatgi, G.T. (1984) Lift-off heights and visible lengths of vertical turbulent jet diffusion flames in still air. *Combustion Science and Technology*, 41, 17-29.
- [51] Kalghatgi, G.T. (1981) Blow-out stability of gaseous jet diffusion flames. Part I: in still air. *Combustion Science and Technology*, 26, 233-239.
- [52] Broadwell, J.E., Dahm, W.J.A., and Mungal, M.G. (1985) Blowout of turbulent diffusion flames. *Proceedings of Combustion Institute*, 20, 303-310.
- [53] Vranos, A., Taback, E.D., and Shipman, C.W. (1968) An experimental study of the stability of hydrogen-air diffusion flames. *Combustion and Flame*, 12, 253-260.
- [54] Takeno, T., and Kotani, Y. (1975) An experimental study on the stability of jet diffusion flame. *Acta Astronautica*, 2, 999-1008.

- [55] Mizutani, Y., and Yano, K. (1978) Blowout behavior and attachment mechanism of coaxial-flow jet diffusion flames. *Bulletin of JSME*, 21, 1634-1641.
- [56] Vanquickenborne, L., and van Tiggelen, A. (1966) The stabilization mechanism of lifted diffusion flames. *Combustion and Flame*, 10, 59-69.
- [57] Takahashi, F., Mizomoto, M., Ikai, S., and Futaki, N. (1985) Lifting mechanism of free jet diffusion flames. *Proceedings of Combustion Institute*, 20, 295-302.
- [58] Takahashi, F., and Schmoll, W.J. (1991) Lifting criteria of jet diffusion flames. *Proceedings of Combustion Institute*, 23, 677-683.
- [59] Takahashi, F., Mizomoto, M., Ikai, S., and Tsuruyama, K. (1990) Stability limits of hydrogen/air coflow jet diffusion flames. 28th Aerospace Sciences Meeting. Reno, Nevada.
- [60] Barlow, R.S., Fiechtner, G.J., Carter, C.D., and Chen, J.Y. (2000) Experiments on the scalar structure of turbulent CO/H₂/N₂ jet flames. *Combustion and Flame*, 120, 549-569.
- [61] Stärner, S.H., Bilger, R.W., Dibble, R.W., and Barlow, R.S. (1991) Piloted diffusion flames of CO/CH₄/N₂ and CO/H₂/N₂ near extinction. *Combustion and Flame*, 83, 63-74.
- [62] Masri, A.R., and Dibble, R.W. (1989) Spontaneous raman measurements in turbulent CO/H₂/N₂ flames near extinction. *Proceedings of Combustion Institute*, 22, 607-618.
- [63] Schefer, R.W., Kulatilaka, W.D., Patterson, B.D., and Settersten, T.B. (2009) Visible emission of hydrogen flames. *Combustion and Flame*, 156, 1234-1241.
- [64] Gaydon, A.G. *The spectroscopy of flames*. 2nd ed. New York, John Wiley & Sons, 1974.
- [65] Takahashi, F., Mizomoto, M., and Ikai, S. (1982) Transition from laminar to turbulent free jet diffusion flames. *Combustion and Flame*, 48, 85-95.
- [66] Dahm, W.J.A., and Mayman, A.G. (1990) Blowout limits of turbulent jet diffusion flames for arbitrary source conditions. *AIAA Journal*, 28, 1157-1162.
- [67] Takahashi, F., and Katta, V. (1995) Numerical experiments on the vortex-flame

- interactions in a jet diffusion flame. *Journal of Propulsion and Power*, 11, 170-177.
- [68] Wierzba, I., and Kilchyk, V. (2001) Flammability limits of hydrogen-carbon monoxide mixtures at moderately elevated temperatures. *International Journal of Hydrogen Energy*, 26, 639-643.
- [69] Joedicke, A., Peters, N., and Mansour, M. (2005) The stabilization mechanism and structure of turbulent hydrocarbon lifted flames. *Proceedings of Combustion Institute*, 30, 901-909.
- [70] Donbar, J.M., Driscoll, J.F., and Carter, C.D. (2000) Reaction zone structure in turbulent nonpremixed jet flames – from CH-OH PLIF images. *Combustion and Flame*, 122, 1-19.
- [71] Donbar, J.M., Driscoll, J.F., and Carter, C.D. (2001) Strain rates measured along the wrinkled flame contour within turbulent non-premixed jet flames. *Combustion and Flame*, 125, 1239-1257.
- [72] Han, D., and Mungal, M.G. (2003) Simultaneous measurements of velocity and CH distributions. Part 1: jet flames in co-flow. *Combustion and Flame*, 132, 565-590.
- [73] Rehm, J.E., and Clemens, N.T. (1998) The relationship between vorticity/strain and reaction zone structure in turbulent non-premixed jet flames. *Proceedings of Combustion Institute*, 27, 1113-1120.
- [74] Kothnur, P.S., Tsurikov, M.S., Clemens, N.T., Donbar, J.M., and Carter, C.D. (2002) Planar imaging of CH, OH, and velocity in turbulent non-premixed jet flames. *Proceedings of Combustion Institute*, 29, 1921-1927.
- [75] Hult, J., Meier, U., Meier, W., Harvey, A., and Kaminski, C.F. (2005) Experimental analysis of local flame extinction in a turbulent jet diffusion flame by high repetition 2-D laser techniques and multi-scalar measurements. *Proceedings of Combustion Institute*, 30, 701-709.
- [76] Kim, M., and Yoon, Y. (2007) Flame residence time and strain rate in turbulent hydrogen non-premixed jet flames with coaxial air. *Proceedings of Combustion Institute*, 31, 1609-1616.

- [77] Kelman, J.B., and Masri, A.R. (1997) Reaction Zone Structure and Scalar Dissipation Rates in Turbulent Diffusion Flames. *Combustion Science and Technology*, 129, 17-55.
- [78] Sutton, J.A., and Driscoll, J.F. (2007) Imaging of local flame extinction due to the interaction of scalar dissipation layers and the stoichiometric contour in turbulent non-premixed flames. *Proceedings of Combustion Institute*, 31, 1487-1495.
- [79] Sutton, J.A., and Driscoll, J.F. (2013) Measurements and statistics of mixture fraction and scalar dissipation rates in turbulent non-premixed jet flames. *Combustion and Flame*, 160, 1767-1778.
- [80] Peters, N. (1983) Local quenching due to flame stretch and non-premixed turbulent combustion. *Combustion Science and Technology*, 30, 1-17.
- [81] Linan, A. The asymptotic structure of counterflow diffusion flames for large activation energies. *Acta Astronautica*, 1, 1007-1039.
- [82] Buch, K.A., and Dahm, W.J.A. (1998) Experimental study of the fine-scale structure of conserved scalar mixing in turbulent shear flows. Part 2. $Sc \approx 1$. *Journal of Fluid Mechanics*, 364, 1-29.

초 록

수소와 일산화탄소의 혼합기체로 이루어진 합성가스의 난류 비예혼합 제트화염에 대한 질소산화물(NOx) 생성 및 화염안정성 특성 연구를 수행하였다. 비예혼합 제트는 가운데 연료 노즐과 주위의 동축공기 노즐로 구성된, 상용 연소기에 흔히 사용되는 노즐의 조합으로부터 생성되었다. 단순 제트화염에서 화염의 체류시간, 제트의 전체 변형률 및 질소산화물의 상관관계를 살펴보고 동축공기 화염에서 화염의 안정적인계 및 국부유동의 특성의 분석을 진행하였다. 이를 위해 질소산화물 농도측정, OH 자발광, PIV, OH PLIF 등을 이용하였으며 극한 near field 영역에서 가시화를 진행하였다.

측정된 단일 제트화염의 길이는 연료제트의 레이놀즈 수가 증가할수록 증가하였고 또한 프라우드 수가 증가할수록 증가하였다. 즉, 본 연구에서의 화염은 부력-모멘텀 천이구간에서 존재함을 확인하였다. 레이놀즈 수가 증가할수록 질소산화물의 생성은 감소하였는데 이는 화염길이 증가에 따른 증가효과보다 연료속도 증가에 따른 감소효과가 더 크게 나타났기 때문이다. 합성가스에서 일산화탄소 함유량이 증가할수록 이론공연비 혼합분율(Z_s)은 커지고 그에 따라 화염길이는 줄어들며 질소산화물 생성도 줄어들게 된다. 단순화된 화염 체류시간 파라미터(L/U_f)를 적용한 개선된 스케일링($EINO_x/(L/U_f) \sim (U_f/d_f^*)^{-n}$)은 부력-모멘텀 천이구간의 모든 연료조건의 합성가스의 결과에서도 모멘텀 제트의 수소화염에서와 같이 $n = -1/2$ 의 값을 가짐을 확인하였다. 단위 공기당 질소산화물 생성을 고려한 더욱 개선된 합성가스에 대한 스케일링($EINO_x/f_{s,i}/(L/U_f) \sim (U_f/d_f^*)^{1/2}$)은 모든 연료조건의 합성가스 결과를 한 라인에 일치시킬 수 있었다.

연료속도 및 동축공기속도 변화에 대한 화염 거동 관찰을 통해 합성가스

제트화염의 부착 안정성 특성 연구를 수행하였다. 단일제트 화염의 화염날림 연료속도는 일산화탄소 함유량이 증가하면서 감소함을 보였는데, 이러한 경향은 높은 일산화탄소 함유 영역에서는 최대 층류화염속도의 경향과 잘 일치하였고 높은 수소 함유 영역에서는 이론공연비 질량비의 경향과 잘 일치하였다. 수소화염에서 동축공기 노즐의 직경은 연료/공기 도메인에서의 안정성에 영향을 미치지 않았고 부상화염의 날림은 제트의 난류 특성에 크게 영향을 받음을 확인하였다. 연료/공기 도메인에서의 안정성 곡선은 노즐 림의 두께가 증가할수록 위로 이동하였다. 비단조(증가/감소; regime I/regime II)의 경향은 모든 합성가스의 경우에서 관찰되었다. OH 자발광 측정을 통해 regime I에서는 노즐 바로 위의 국부소염, regime II에서는 노즐 위의 전단층이 시작되는 곳에서의 국부소염이 관찰되었다. Regime I에서의 안정성 커브는 연료와 공기의 질량 플럭스 변수로 스케일링될 수 있었다. 단일노즐 화염날림 제트속도로 평균화된 연료속도를 x축으로 표현한 안정성 커브의 최대점은 동일한 노즐두께를 가지는 경우에 동일함을 보였다.

감소구간(regime II)의 부착화염의 날림에 대한 이해를 위하여 PIV와 OH PLIF 동시측정을 통한 변형율 및 OH의 특성을 살펴보았다. OH에서의 주변형율의 평균값은 축방향에 따라 감소하였고 노즐 출구 근처에서 최대값을 나타내었다. 어떤 경우에는 주변형율 평균의 최대값이 안정적인 근처의 화염보다 안정적인 화염의 경우에 더 크게 나타났다. 다른 제트 속도의 경우라도 안정적인 근처의 화염들은 거의 같은 최소 OH 두께를 노즐 근처에서 가짐을 보였다. 주변형율과 OH 두께는 역의 관계를 가지지만 OH 두께는 낮은 주변형율 구간에서 넓은 분포를 나타내었다. OH 두께의 확률밀도함수는 높은 주변형율의 조건에서 낮은 값에서 분포하고 안정화염에서 한계영역으로 갈수록 피크 값이 낮은 쪽으로 이동하였다.

중심어: 비예혼합화염, 확산화염, 난류화염, 제트화염, NO_x 스케일링, 질소산화물, EINO_x, 화염안정성, 화염길이, 신장율, OH, 스칼라 소산, PIV, OH PLIF, IGCC, 합성가스 연소

학 번: 2009-30906